Ionoacoustics for Three-Dimensional Particle Bunch Monitoring

Sonja Gerlach

München 2023

Dreidimensionale Charakterisierung von Teilchenpaketen mittels Ionoakustik

DISSERTATION

an der Fakultät für Physik der

Ludwig-Maximilians-Universität München

vorgelegt von

Sonja Gerlach

geboren in Langen

München, den 24. August 2023

Erstgutachter: Prof. Dr. Jörg Schreiber
Zweitgutachter: Prof. Dr. Katia Parodi
Tag der mündlichen Prüfung: 13.11.2023

Zusammenfassung

Ionoakustik meint die Messung akustischer Wellen, die entstehen, wenn Ionen in Materie abbremsen. Eine besonders interessante Anwendung ist die Charakterisierung von einzelnen laserbeschleunigten Ionenpaketen, die für viele etablierte Online-Detektionssysteme eine Herausforderung darstellt. Der ionoakustische Ansatz bietet in diesem Zusammenhang verschiedene Vorteile. Die Methode ist resistent gegenüber den starken elektromagnetischen Pulsen, die bei der Laser-Plasma-Wechselwirkung auftreten, und zeigt auch bei sehr hohen Teilchenströmen keine Sättigung. Die prinzipielle Möglichkeit, die Energieverteilung von Teilchenpaketen aus einem akustischen Signal zu gewinnen (I-BEAT), wurde bereits konzeptionell gezeigt. In dieser Arbeit werden zwei neue Detektordesigns vorgestellt: der I-BEAT 3D und der TI-BEAT Detektor. Zur Auswertung der Daten wird eine schnelle Analysemethode aus einem analytische Model entwickelt. Das Ergebnis ist ein innovativer und vielseitiger Detektor für kurze und intensive Teilchenpakete, der direktes Feedback liefert.

Die Beschreibung der Dosisdeposition von Protonen in Materie, insbesondere im Eintrittsfenster und Wasserreservoir des Detektors, verbindet die wichtigsten Parameter der Protonenpakete mit den resultierenden ionoakustischen Signalen und bildet somit die Grundlage für die Entwicklung einer einfachen und schnellen Datenanalysemethode für Teilchenpakete mit gaußförmigen Energiespektren und lateralen Verteilungen. Dies ermöglicht die Analyse und Interpretation der akustischen Signale, die mit den Detektoren gemessen werden.

Der I-BEAT 3D Detektor verwendet vier Ultraschallköpfe und wurde in Experimenten an zwei lasergetriebenen Protonen-Strahlführungen am CALA und HZDR getestet. Durch das neue analytische Modell ermittelt der Detektor die mittlere Energie, die Energiebreite und die laterale Position der einzelnen Protonenpakete in unter einer Sekunde. Darüber hinaus ermöglicht der Detektor die Messung relativer Änderungen in der lateralen Größe der Protonenpakete. Die durchgeführten Experimente mit Protonenpaketen bei kinetischen Energien zwischen 10 MeV und 30 MeV zeigen eine Auflösung im sub-MeV- und sub-mm-Bereich. Durch die Kalibrierung des Detektors mit radiochromen Filmen kann die absolute Anzahl der Protonen in einem Paket mit einer Unsicherheit von lediglich 10% bestimmt werden.

Der TI-BEAT Detektor besteht aus einem schmalem Wasserreservoir, welches von Ionen mit ausreichend Energie passiert werden kann. Er soll zeigen, dass Ionoakustik auch als Transmissionsmonitor für Teilchenpakete genutzt werden kann. Das Detektorkonzept wurde am SIS-18-Synchrotron der GSI mit Xenon-Ionen bei kinetischen Energien von 385 MeV/u getestet. Die Bestimmung der absoluten lateralen Position des Ionenpakets wird mit einer Präzision von 0,15 mm demonstriert. Relative Änderungen der lateralen Größe des Ionenpakets können mit einer Präzision von unter 0,1 mm detektiert werden. Die Messung der Teilchenzahl des Ionenpakets wird mit einer Präzision zwischen 4% und 8% gezeigt.

Die neuen Detektordesigns und die analytische Methode zur Datenanalyse stellen ein schnelles, kompaktes, kostengünstiges und gegen elektromagnetische Pulse resistentes Online-Tool zur Charakterisierung wichtiger Parameter von Ionenpaketen an Anwendungsplattformen dar. Dies bildet die Grundlage für Bestrahlungsstudien und kann als Rückkopplung für die automatische Optimierung von lasergetriebenen Protonenquellen genutzt werden.

Abstract

Ionoacoustics refers to the measurement of acoustic waves excited by ions as they slow down in matter. One particularly interesting application is the monitoring of individual laser-accelerated ion bunches, which challenges many established online detection systems. The ionoacoustic approach offers advantages in this context. It is resistant to the strong electromagnetic pulse emitted during the laser-plasma interaction, and it does not exhibit saturation even at very high particle fluxes. Recovering the Ion-Bunch Energy distribution from a recorded Acoustic Trace (I-BEAT) has conceptually been proven. This work introduces two new detector designs, the I-BEAT 3D and the TI-BEAT detector, and develops a fast analysis routine based on an analytical model. The result is a novel and versatile online detector for short and intense ion bunches that enables immediate feedback.

Describing the dose deposition of protons in matter, particularly in the entrance window and the water reservoir of the detector, connects the most important proton bunch parameters to the resulting ionoacoustic signals and hence serves for the development of a simple and fast data analysis method for particle bunches with Gaussian energy spectra and lateral distributions. This is key to the analysis and interpretation of the acoustic traces obtained with the detector designs.

The I-BEAT 3D detector uses four transducers and is studied in experiments at two laser-driven proton beamlines located at CALA and the HZDR. Via the new analytical model, it provides the mean bunch energy, energy spread and lateral bunch position of individual bunches in less than one second. Additionally, the detector allows the monitoring of relative changes in lateral bunch size. Experiments with proton bunches at kinetic energies between 10 MeV and 30 MeV reveal sub-MeV and sub-mm resolution. Cross-calibration using radiochromic films proves that the new methodology can determine the absolute number of particles contained in a single bunch with uncertainties of only 10%.

The TI-BEAT detector uses a short water reservoir to allow ions with sufficient energy to pass through. It is developed to prove that ionoacoustics can also function as transmission monitor for particle bunches. The detector concept is evaluated at the GSI's SIS-18 synchrotron with xenon ions at kinetic energies of 385 MeV/u. The precision of determining the absolute lateral position and relative changes in the lateral size of ion

bunches is 0.15 mm and less than 0.1 mm, respectively. The particle number is extracted with a precision between 4% and 8%.

The new detector designs and the data evaluation method provide a fast, compact, cost-effective and electromagnetic pulse-resistant online tool for monitoring important ion bunch parameters at application sites. This provides the foundation for irradiation studies and can serve as feedback for automated optimization of laser-driven proton sources.

Contents

List of Figures

List of Tables

Abbreviations

ALBUS-2S Advanced Laser-driven Beamlines for User-specific Studies - 2 Solenoids

BP Bragg Peak

CALA Centre for Advanced Laser Applications

CMUT Capacitive Micromachined Ultrasonic Transducers

CPA Chirped Pulse Amplification

EIR Electric Impulse Response

EMP Electromagnetic Pulse

EW Equal Width

FODO Focusing Optic Defocusing Optic

FWHM Full-Width at Half-Maximum

GSI Helmholtzzentrum für Schwerionenforschung

HZDR Helmholtz-Zentrum Dresden-Rossendorf

I-BEAT Ion-Bunch Energy Acoustic Tracing

IC Ionisation Chamber

LION Laser-driven ION

PMQ Permanent Magnet Quadrupole

pps particles per spill

PtP Peak-to-Peak

RCF Radiochromic Film

RF Radio Frequency

ROI Region Of Onterest

SNR Signal-to-Noise Ratio

SEETRAM SEcondary-Electron TrAnsmission Monitor

SIR Spatial Impulse Response

SIS18 SchwerIonenSynchrotron 18

TI-BEAT Transmissive Ion-Bunch Energy Acoustic Tracing

TIR Total Impulse Response

TNSA Target Normal Sheath Acceleration

TOD Third-Order Dispersion

TOF Time-Of-Flight

TP Thomson Parabola

WET Water Equivalent Thickness

1 Introduction

The detection of particles is a common challenge to many modern physics disciplines, including astrophysics, particle physics, and medical physics. In order to extract particle properties such as charge or energy, particles must interact with the detector material. As a result, the fundamental physics of particle detection can be condensed into describing the interaction between particles and matter. For individual particles and short time scales, interactions can be attributed to one of the three fundamental forces described by the standard model, except gravitation, which is considered the fourth fundamental force [1]. In the case of swift charged particles, the dominant interaction is typically governed by the electromagnetic force [2]. While single-particle interactions adhere to the probabilistic nature of quantum mechanics, the typically large number of interactions involving many particles allows for a statistical and reproducible description of particle behaviour in matter. Energy transfer from particles to the detector material happens via a cascade of processes contingent on the composition of the detector. Nowadays, many detection systems employ the fast conversion of the particle's energy into light or charge, such as scintillators or ionisation chambers, which typically generate signals on pico- or nanosecond timescales. The other end of the spectrum of detectors is based on slow processes, such as calorimetry or ionoacoustics. Ionoacoustics has recently regained attention as a novel and intriguing option for detecting and characterising short particle bunches.

Ionoacoustics describes the emission and measurement of acoustic waves when ions deposit energy in matter. It is closely related to photoacoustics or optoacoustics, where the absorption of short laser pulses generates the acoustic waves [3]. The concept of pressure waves induced by ions was first theorised by Askaryan in 1957 [4]. In 1979, first experimental studies performed at the Brookhaven National Laboratory were published by Sulak [5] and compared to the previously developed analytical model [6]. In addition to its potential application in detecting neutrinos in the ocean, these publications further propose the use of ionoacoustics for beam monitoring, particularly mentioning the beam intensity and lateral beam parameters.
In the present day, ionoacoustics has garnered significant research interest in treatment

verification for ion beam therapy of tumours. [7]. Compared to traditional radiation therapy with photons, the depth dose curve of protons or heavier ions in human tissue allows for more precise dose deposition. The surrounding healthy tissue is speared by matching the particle's Bragg Peak (BP) in the planned target volume [8]. However, range uncertainties caused by factors such as patient misalignment, organ motion, or limited knowledge of ion stopping power still limit the full potential of ion beam therapy [9, 10]. To address this challenge, in vivo verification during or shortly after treatment has been discussed [11]. The most well-established methods for treatment verification are positron emission tomography (PET) and prompt gamma (PG) imaging [9, 12]. While PET systems for treatment verification are already available clinically [13–15], PG prototypes are currently being investigated in clinical trials [9, 16].

Compared to these established approaches, ionoacoustics has evolved only slowly in the context of treatment verification. The measurement of an acoustic pulse generated in a patient during treatment was first demonstrated in 1991 by Tada et al [17] and in 1995 by Hayakawa et al [18]. These early studies were followed by promising experimental campaigns that systematically investigated the properties of ionoacoustics. An important milestone was achieved in localising the BP with sub-millimetre accuracy in water phantoms [19–21]. To facilitate meaningful results in a clinical context, advanced dose reconstruction algorithms have been developed through numerous simulation [22–25] and experimental studies [26, 27]. These studies have been conducted using various ion sources, including linear accelerators [19, 26, 27], clinical isochronous cyclotrons (in combination with a pulsing system) [22], synchrocyclotrons [20] and synchrotrons using fast beam extraction [17, 18, 28]. However, typical clinical dose rates in combination with the high beam energies result in relatively weak acoustic signals with low frequencies that are difficult to detect [29]. To address this challenge, innovative ultrasonic detector designs such as Capacitive Micromachined Ultrasonic Transducers (CMUT) are under investigation due to their potential for extended bandwidths in the lower frequency range [29] and smaller footprints compared to conventional piezoelectric ceramic transducers. Furthermore, the possibility of signal enhancement by using gold markers [30] or contrast agents such as Indian ink and microbubbles [31] is investigated as well.

While clinical applications fight for the lower detection limit of ionoacoustics, the challenge of particle bunch detection at laser-ion sources is the opposite, as instantaneous dose rates are typically significantly increased by a factor of 10^9 compared to clinical accelerators. Therefore, ionoacoustics is ideally suited as detection method.

Laser-ion sources In recent decades, high-power laser systems have garnered increasing scientific interest due to their potential for various applications, including the acceleration of protons and heavier ions [32, 33]. The development of the Chirped Pulse Amplification (CPA) technique has enabled the increase of laser peak powers to the petawatt level, representing the current state-of-the-art technology for high-power laser systems. The concept behind this Nobel Prize-awarded technique involves stretching the laser pulse in time during the amplification process, which enables amplification of the laser energy with moderate space consumption. After amplification and before application, the pulse is compressed in time and typically focused to a small spot, resulting in peak intensities of up to 10^{23} W/cm^2 [34]. The interaction between this high-intensity laser and a target material leads to the production of highly energetic ions, reaching up to 100 MeV [35] for protons. These ions exhibit properties that complement Radio Frequency (RF) acceleration, particularly due to ultra-high peak intensities [36, 37] and the ability to synchronously accelerate multiple ion species and ion charge states. Furthermore, the resulting ion bunch is highly divergent, characterised by a small source size and a broad energy spectrum, and accompanied by other radiation modalities and a strong Electromagnetic Pulse (EMP). Dedicated beamlines have been developed for the manipulation of particle bunches, aiming to transport and focus a selected portion of the energy spectrum emitted from the plasma to a small spot with a typical size of a few millimetres [38–40]. The unconventional properties of laser-accelerated ions open up promising application fields, including:

- Medical physics: Potential usage of laser-accelerated ions for radiation therapy is discussed as a long-term goal. However, research in radiobiology, e.g. studying the Flash effect [41], or imaging, e.g. employing the bi-modal imaging capabilities [42], is possible already.

- Radiation chemistry: The ultrashort ion bunches provide a unique opportunity to experimentally study ultrafast processes initiated by the energy deposition of protons in water [43].

- Nuclear physics: The high density of laser-accelerated ion bunches is an interesting complement to study fission-fusion processes [44].

Determining the bunch parameters of laser-accelerated ions is one vital prerequisite for all applications and has remained a challenge [32, 45], in particular due to the specific character that makes the bunches so interesting.

Measurements of laser-accelerated ions today largely rely on offline detectors, such as Radiochromic Films (RCFs), image plates and nuclear track detectors to record the dose deposited by protons [35, 46] and heavier ions [47, 48]. Although robust, evaluation is time-consuming. Therefore, online detection methods are developed, especially in combination with energy spectrometers based on magnetic fields [49]. In a Thomson Parabola (TP), the magnetic field is complemented by an electric field, further allowing to resolve the energy distribution based on the charge-to-mass ratio of the accelerated particles [50]. Employing multiple TPs at different angles relative to the target normal direction is one possible approach to investigate the angular distribution of the ions [51]. The detection of the dispersed ions typically relies on micro-channel plates [50] or on semiconductor detectors [52]. One alternative for determining the energy distribution is a Time-Of-Flight (TOF) spectrometer, for example positioned in the focus of an ion beamline. Diamond detectors currently provide the best energy resolution for TOF spectrometers [53], but scintillators offer a more cost-effective option and can be realised less invasive [54]. Scintillators are also commonly used for obtaining information on the lateral ion bunch profile [55–57]. For absolute dosimetry, Ionisation Chambers (ICs) are commonly employed, even though high dose rates can pose a challenge due to saturation [41]. More recently, integrating current transformers have been demonstrated for measuring the total charge contained in a particle bunch [58].
The ionoacoustic method has recently been employed for reconstructing the ion bunch energy distribution from the measured Acoustic Trace (I-BEAT) for laser-accelerated proton bunch. [59]. One benefit of I-BEAT is the analogue delay of amplification and digitisation due to the low speed of sound. This enables separation of the signal from prompt disturbances such as the EMP. In addition, the conversion of deposited energy density into pressure is linear over a large range of bunch intensities [28]. So far, I-BEAT yielded the energy spectrum of an individual proton bunch by an iterative reconstruction algorithm that also approximated the lateral bunch size by using only one ultrasonic transducer [59]. In practice, this reconstruction has remained quite time-consuming and required tedious calibration of the set-up. Therefore, although the signal is available online, the data evaluation is not.

Research goals of this work Despite the various detection systems, there is currently a lack of online detection systems specifically tailored to laser-accelerated ions. In particular, there is no available online detection system that can simultaneously provide information on the three-dimensional particle bunch properties of laser-accelerated protons, hence;

The scientific goal of this work is to develop a monitor for the three-dimensional properties of focused laser-accelerated protons based on the ionoacoustic principle.

To tackle this goal, the I-BEAT 3D detector was developed in the framework of this thesis. Compared to the already demonstrated I-BEAT detector [59], I-BEAT 3D not only has the capability to determine the axial bunch properties (i.e., the energy distribution of the bunch) but also provides information on the lateral proton bunch parameters. This information is obtained by a simplified and hence fast filtered raw data analysis that provides the proton bunch mean energy and energy width, lateral position and lateral size, as well as the bunch particle number directly from the four acoustic traces. In the framework of this development, the following research questions will be addressed:

- Q1: What further information is obtained by three additional lateral transducers?
- Q2: Is a fast data analysis based on an approximate model suitable for providing immediate information on the bunch parameters, and how precise can these parameters be determined?
- Q3: Is ionoacoustics a suitable method for absolute dosimetry of laser-accelerated protons?
- Q4: Can ionoacoustics be utilised as a non-destructive ion diagnostics technique?

To address these questions, three experimental campaigns were conducted at the Laser-driven ION (LION) set-up of the Centre for Advanced Laser Applications (CALA) in Garching, the Advanced Laser-driven Beamlines for User-specific Studies - 2 Solenoids (ALBUS-2S) beamline at the Helmholtz-Zentrum Dresden-Rossendorf (HZDR) and the SchwerIonenSynchrotron 18 (SIS18) Synchrotron at the Helmholtzzentrum für Schwerionenforschung (GSI) in Darmstadt. The results of the experiments conducted at the ALBUS-2S beamline are published in reference [60].

Outline of this thesis The main focus of this research is the development of ionoacoustic detectors specifically designed for analysing focused and energy-selected laser-accelerated proton bunches. Consequently, the theoretical background presented in chapter 2 begins by elucidating the characteristics of laser-accelerated ions at both the source and the

focal point of a dedicated beamline. Understanding the theoretical aspects of laser-plasma interaction is relevant as it unveils the unique properties exhibited by the particle bunches, thereby necessitating the development of novel detectors. The theory chapter also describes the analytical model of ionoacoustic signals generated in the I-BEAT detector and serves as the foundation for analysing the experimental data.
Chapter 3 describes the material and the methods used in this work. It presents the design of the two employed detector set-ups, namely the I-BEAT 3D detector mentioned earlier, as well as the Transmissive Ion-Bunch Energy Acoustic Tracing (TI-BEAT) detector. The chapter also provides information on the ultrasonic transducers and signal amplification as well as details about the set-ups used in the three experimental campaigns. Special attention is on the manipulation of the bunch parameters as crucial asset for testing the detector capabilities. The chapter also describes the data analysis of ionoacoustic signal traces and the readout routine of the complementary detectors employed in this work.
Chapter 4 presents the results of the experimental studies, organised according to the two detector designs. The outcomes of the two experimental campaigns conducted with the I-BEAT 3D detector at the laser-driven proton sources are presented together, structured based on the deduced bunch properties. The results obtained from measurements with the TI-BEAT detector at the SIS18 synchrotron beamline are presented separately.
In chapter 5, the results are discussed. It explores the limitations of the detector designs and data evaluation and suggests improvements.
Finally, this thesis concludes with a summary of the most significant results obtained in this work and an outlook in chapter 6. It proposes possible future research studies and applications of the developed detectors, specifically in but not limited to the field of laser-ion acceleration.

2 Theoretical background

2.1 Laser-driven ion acceleration

Laser-driven ion acceleration is typically realised by focusing a high-power laser onto a solid-density target. In this chapter, the interaction process is shortly introduced with an emphasis on the particularly interesting properties of laser-accelerated particle bunches, which necessitate the development of new detectors. The given information on laser and target systems is tailored to the experimental set-ups employed in the scope of this study. For a more comprehensive understanding of the subject, detailed information can be found in references [32] and [33].

The interaction of the laser with the target is highly complex and results in a wide variety of effects. First of all, the large electrical laser fields generate a plasma when the intensity of the laser pulse crosses the ionisation threshold of the target material. The specific physics and dominant processes of the following laser-plasma interaction depend on the laser and target parameters and are highly nonlinear.

Current laser-driven ion acceleration experiments utilise lasers powers of hundreds of TW up to a few PW focused to small spots with a size of a few μm enabling peak intensities up to $10^{23}\mathrm{W/cm}^2$ [34, 61]. Various types of lasers with different pulse lengths and repetition rates have been employed. As an example, Ti:Sa laser systems are meanwhile well established in laser-driven ion acceleration with pulse durations as low as 20 fs and repetition rates of up to 10 Hz [61]. Thin foils with thicknesses ranging from a few nanometres to several micrometres, the optimum is dictated by the laser temporal profile and contrast curve, are typical targets. Protons are the dominant ion species accelerated because they are present on the target surface as contaminants unless a hydrogen-free target is significantly heated [47].

In the past decades, different acceleration mechanisms have been observed depending on the laser and target parameters. In this work, the so-called Target Normal Sheath Acceleration (TNSA) model is introduced to describe laser-driven ion acceleration. While TNSA is the most established model, it should be noted that depending on the combinations of laser and target parameters, alternative acceleration regimes can be observed, such as radiation pressure acceleration [62] or collisionless shock acceleration [63]. In

many practical cases, a mixture of several acceleration processes is present.

2.1.1 Laser-plasma interaction

A short laser pulse starts ionising the target material when reaching intensities $I_\mathrm{l} > 10^{12}\mathrm{W/cm^2}$ [64]. This intensity is either reached in the coherent contrast region many picoseconds before the peak of the pulse or by preceding prepulses. For longer irradiation times, even smaller intensities in the pulse pedestal, typically due to amplified spontaneous emission (ASE), can lead to target heating and plasma generation. Thus, the interaction with the main pulse takes place when the target is already transformed into a plasma. For laser-driven ion acceleration, the plasma is typically required to be overdense, meaning that the electron density n_e remains larger than the critical density n_c. The critical density is defined as the density at which the plasma frequency ω_P equals the frequency of the laser light ω_L. While an overdense plasma appears opaque to the laser, the critical density defines the transition when the plasma becomes transparent. Ignoring collisions, the critical density is

$$n_\mathrm{c} = \frac{m_\mathrm{e}\omega_\mathrm{L}^2}{4\pi e^2} \tag{2.1}$$

with the constants m_e and e being the mass and charge of an electron, respectively. For a Ti:Sa laser system with a central wavelength of 800 nm, n_c is calculated to $1.7 \cdot 10^{21}\mathrm{cm^{-3}}$. When the electron motion becomes relativistic, the critical density increases to $\approx \gamma n_\mathrm{c}$ where γ is the average Lorentz factor of the electrons in the interaction volume. Plasmas with densities lower than the critical density are referred to as underdense.
During the laser-plasma interaction, the laser pulse primarily interacts with the electrons in the plasma due to their low mass. The electrons oscillate in the laser field and experience a net energy transfer known as electron heating. It is important to note that electron heating plays a significant role in the acceleration process as it governs the coupling of laser energy into the plasma. The detailed mechanisms depend on the laser parameters and are not focus of this work; further information can be found in reference [65]. At high electron energies, their motion must be analysed relativistically. A key parameter characterising this transition is the dimensionless laser amplitude a_0 calculated by

$$a_0 = \frac{eE_\mathrm{L}}{m_\mathrm{e}c\omega_\mathrm{L}} = \sqrt{\frac{I_\mathrm{L}}{m_\mathrm{e}c_\mathrm{L}^3 n_\mathrm{c}}} \tag{2.2}$$

where E_L and I_L are the laser electric field amplitude and intensity, respectively, and c_L is the speed of light In a non-relativistic calculation, the electrons would reach the speed of light at $a_0 = 1$. Therefore, when a_0 approaches 1, the electron dynamics need to be treated relativistically. As an example, for a Ti:Sa laser with a peak intensity of 10^{21} W/cm^2, a_0 is 21.5, indicating that the dynamic of the plasma electrons in the laser field is highly relativistic.

2.1.2 Target normal sheath acceleration

Assuming a sufficiently thick and opaque target, the laser-plasma interaction is located at the irradiated side. Electrons are energised and heated, with an overarching oscillation frequency dictated by the laser field or intensity. When the target is not excessively thick, the most energetic electrons penetrate through the target. At the rear side, the electrons generate a sheath field with a field strength on the order of TV/m [32,33]. The extent of this sheath field into the vacuum is related to the hot electron Debye length

$$\lambda_D = \sqrt{\frac{\epsilon_0 T_e}{4\pi e^2 n_{e,hot}}} \tag{2.3}$$

where ϵ_0 is the electric constant, T_e the average energy (temperature) and $n_{e,hot}$ the average density of the hot, penetrating electrons [33]. The Debye length is of similar order as the laser wavelength [32] or of order the laser focal spot diameter [66,67].
Positively charged ions are accelerated by the sheath field in the direction normal to the target rear surface. The acceleration is proportional to the charge-to-mass ratio, promoting protons. The electric field experienced by the ions depends on their initial position, resulting in an exponential ion energy spectrum [68].

Figure 2.1 shows examples of energy spectra measured at three laser-driven proton sources. All three systems show the expected exponential proton energy distribution, despite the remarkable differences in the drive lasers. The PHELIX laser relies on a Nd:Glass system featuring relatively long laser pulses ($\approx$ 0.5 ps) and high energies of 200 J focused by an f/1.7 parabola to a spot of 4 μm Full-Width at Half-Maximum (FWHM) [70]. The DRACO and the ATLAS 3000 are both Ti:Sa systems with short pulses ($\approx$ 30 fs). The pulses of the DRACO laser deliver 18 J focused by an f/2.3 parabola to a spot with 2.6 μm FWHM [71], while the ATLAS 3000 pulses have an energy of 8 J focused by an f/5 parabola to a spot with 4.9 μm FWHM [72,73]. The DRACO and ATLAS 3000 systems serve as the drive lasers for the ALBUS-2S and the LION beamlines, respectively, where experiments are conducted within the scope of this study. Therefore, the presented

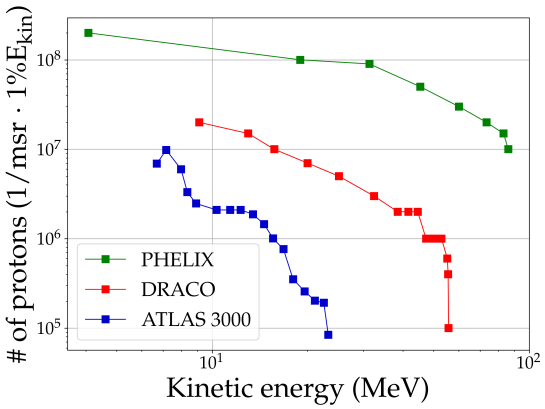

Figure 2.1: Energy spectra of laser-accelerated protons measured at three laser systems (colour code). The line connecting the measured data dots is a guide to the eye. Data taken from reference [69] and originally published in references [70] (PHELiX), [71] (DRACO) and [72] (ATLAS 3000).

spectra serve as a benchmark for the energy distribution of the laser-accelerated protons of the respective source before entering the beamline.

The acceleration time is in the order of the laser pulse duration [67]. Although this might underestimate the acceleration time for short pulse lasers such as provided by Ti:Sa systems [74], an important characteristic of laser-accelerated ion bunches is their very short initial duration, typically in the order of a picosecond and less, which is much shorter compared to conventional RF-accelerators. However, due to the broad energy distribution, the bunch spreads in time as it propagates away from the target. Along with the high particle numbers reaching more than 10^8 protons/(msr $\cdot$ 1%E_{kin}) [69], the short bunch duration leads to very high particle fluxes.

Because the sheath field is normal to the target only in the centre, typical proton bunch half-angle divergences are in the tens of degrees. Higher-energy particles are emitted at smaller divergence angles compared to the lower-energy part of the spectrum [61]. The transverse extent of the sheath field can spread over several hundreds of micrometres [67], but the transverse emittance is remarkably small and of order μm mrad [37].

The recent past has proven that reducing the target thickness is beneficial for gaining larger proton energies and numbers. This is partially related to new acceleration regimes in which the radiation pressure of the laser and/or the partial transparency of the target plays its role. The general properties of a typical proton bunch emitted from a laser-plasma interaction, in particular its energy spread, small transverse and longitudinal emittance, large particle numbers, etc., have remained similar so far [69].

2.2 Particle bunch transport

Laser-accelerated ion bunches are characterised by a large divergence and an exponential energy spectrum. While these properties are particularly favourable for some applications, others require a well-defined focal spot and/or a narrow energy distribution. To achieve this, dedicated ion beamlines can be implemented. The studies conducted in the scope of this work are performed with beamlines based on Permanent Magnet Quadrupoles (PMQs) and a pulsed high-field solenoid. Thus, the underlying functionality of these focusing elements is explained in the course of this chapter, with special attention on the particle bunch properties in the ion focus. It is worth mentioning that plasma lenses have regained attention for ion bunch focusing, in particular miniature versions, due to their larger field gradients compared to PMQs or solenoids [75].
The common principle among these beamline concepts is the use of strong magnetic fields to achieve focusing. The focusing is a consequence of the magnetic component of the Lorentz force, given by

$$\vec{F} = q\left(\vec{v} \times \vec{B}\right), \tag{2.4}$$

where q represents the particle's charge, $\vec{v}$ is its velocity, and $\vec{B}$ is the magnetic field. While the exact dependence of the focusing properties on the particle's energy varies for the different beamline designs, equation 2.4 already indicates a chromaticity. Thus, the focusing elements not only reduce the lateral extent of the ion bunch but can also serve as an energy selection system by dispersing certain spectral components. In combination, this results in a focal spot of small diameter with a narrow energy spread. By a proper beamline design, the lateral size and energy spread of the ion bunch in the focus position can be tailored to specific applications. During transport through the beamline, the bunch duration increases compared to its initial properties from the ion source due to the energy spread. However, even at the application location 1-2 meters downstream, the bunch duration remains small and of order few nanoseconds. This is still significantly shorter than bunch durations at conventional RF accelerators. For example, the bunch duration at the SIS 18 synchrotron during the experiments conducted in this work is approximately 300 ns. The exact bunch duration of the laser-accelerated and focused ion bunch is defined by the distance between the source and the ion focus, along with the transported energy spectrum. The combination of the short bunch duration, the large number of accelerated particles and the small focal spot lead to very high particle fluxes in the ion focus, which are particularly interesting for certain applications and hence

require adequate online detection systems.

2.2.1 Particle bunch dynamics

In this section, statistical bunch parameters are introduced according to reference [76] and [77] to evaluate the impact of beamline elements on the ion bunch. As most literature is focused on conventional accelerators, the term 'beam' is used, although the rest of this work specifically pertains to particle bunches that meet more the properties of laser-accelerated particles. The dynamics of a single particle are fully characterised by its position and momentum as a function of time, which can be represented as a point in the six-dimensional phase space. A particle ensemble can then be described by a density distribution ψ in this phase space. This section focuses on the bunch description in trace space, where the momentum is substituted by the particles direction $x' = p_\mathrm{x}/p_\mathrm{z}$ with p_x being the transverse momentum in x-direction and p_z the longitudinal momentum in the main propagation direction z. Under the assumption of no correlations between x and y dimensions, to simplify the analysis, only a two-dimensional subspace is considered. It is obtained by projecting the six-dimensional trace space onto a two-dimensional trace space that describes the bunch dynamics in only one space coordinate. Assuming the bunch travels in z-direction, the particle state for the lateral space coordinate $\vec{x}^{\mathbf{T}} = (x, x')$, with x being the position and x' the direction of the particle, are described by the so-called beam ellipse

$$\vec{x}^{\mathbf{T}} \boldsymbol{\sigma}_\mathrm{x}^{-1} \vec{x} = 1 \tag{2.5}$$

with the symmetric matrix

$$\boldsymbol{\sigma}_\mathrm{x} = \begin{pmatrix} \sigma_{11} & \sigma_{12} \\ \sigma_{12} & \sigma_{22} \end{pmatrix} . \tag{2.6}$$

The matrix entries represent the beam parameters describing the ion bunch and, thus, the form of the beam ellipse:

- The standard deviation of the spatial distribution is given as $\sigma_\mathrm{x} = \sqrt{\sigma_{11}}$ and defines the maximum elongation in x-direction. It is connected to the single particle dynamics by

$$\sigma_\mathrm{x}^2 = \int_{-\infty}^{\infty} \int_{-\infty}^{\infty} x^2 \cdot \psi(\vec{x}) \; dx dx' \quad , \tag{2.7}$$

which is the variance of the trace space projected on the space coordinate. $\psi(\vec{x})$ is the two-dimensional density distribution.

- The standard deviation of the angular distribution is given as $\sigma_{\mathrm{x'}} = \sqrt{\sigma_{22}}$ and defines the maximum elongation in x'-direction. It is connected to the single particle dynamics by

$$\sigma_{\mathrm{x'}}^2 = \int_{-\infty}^{\infty}\int_{-\infty}^{\infty} x'^2 \cdot \psi(\vec{x})\ dxdx' \quad , \tag{2.8}$$

  which is the variance of the trace space projected on the direction coordinate.

- The tilt of the ellipse is described by the correlation between the spatial and the angular distribution $\sigma_{\mathrm{xx'}} = \sigma_{12}$. $\sigma_{12} < 0$ corresponds to a focusing beam, $\sigma_{12} > 0$ corresponds to a diverging beam. $\sigma_{12} = 0$ describes a beam in the focus and a parallel beam as well. The correlation is connected to the single particle dynamics by

$$\sigma_{\mathrm{xx'}} = \int_{-\infty}^{\infty}\int_{-\infty}^{\infty} xx' \cdot \psi(\vec{x})\ dxdx' \quad , \tag{2.9}$$

  which describes the correlation between the space and the angular coordinate in trace space.

While the beam parameters change over time (along the path), the volume of the density distribution and thus the area of the beam ellipse remain constant following Liouville's theorem if no particles are lost and only conservative forces apply [77]. As a conserved quantity, the beam emittance ϵ is introduced. In x-direction, ϵ_{x} writes

$$\epsilon_{\mathrm{x}} = \sqrt{\mathrm{Det}(\boldsymbol{\sigma}_{\mathrm{x}})} = \sqrt{\sigma_{11}\sigma_{22} - \sigma_{12}^2} \tag{2.10}$$

and is related to the area of the beam ellipse A_{x} by

$$A_{\mathrm{x}} = \pi\epsilon_{\mathrm{x}}. \tag{2.11}$$

The SI units of the introduced beam parameters are given as

$$[\sigma_{11}] = \mathrm{m}^2, \quad [\sigma_{12}] = \mathrm{m}\cdot\mathrm{rad}, \quad [\sigma_{22}] = \mathrm{rad}^2, \quad [\epsilon] = \mathrm{m}\cdot\mathrm{rad}. \tag{2.12}$$

The specific form of the density distribution ψ can, in principle, be arbitrary. However, a Gaussian distribution often provides a good approximation for both the spatial and

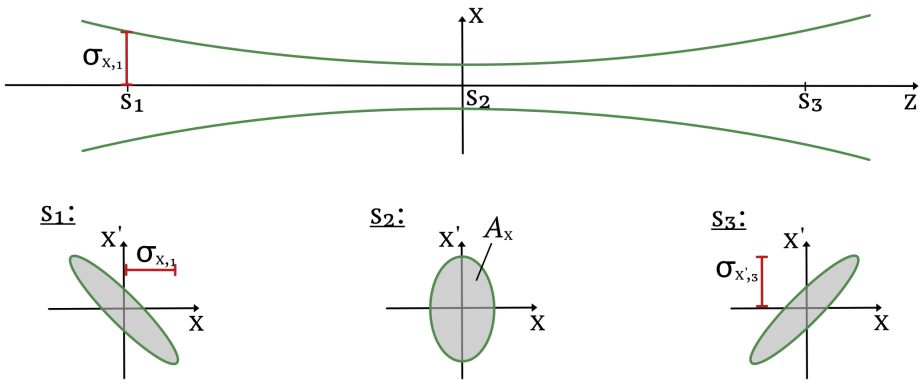

Figure 2.2: Schematic drawing of the beam waist and the beam ellipses in trace space at three positions s_1 before the beam waist, s_2 at the beam waist and s_3 after the beam waist. The beam travels in z-direction, and only one lateral dimension x is represented. The area of the ellipse A_x is marked in grey, and the beam parameters σ_x and $\sigma_{x'}$ are shown in red.

momentum distributions. Then, the density distribution can be expressed as

$$\psi(\vec{x}) = \frac{1}{2\pi\epsilon_x} \exp\left(-\frac{1}{2}\vec{x}^{\intercal}\boldsymbol{\sigma}_x{}^{-1}\vec{x}\right). \tag{2.13}$$

The beam ellipse then marks the contour line where the density is reduced to $\exp(-1/2)$, which follows directly from equation (2.5). To provide a visual representation of the described particle bunch dynamics, figure 2.2 illustrates the beam ellipse at three different positions around the beam waist of freely propagating and focusing particles. The beam waist refers to the location where the spatial extension is at its minimum.

With the description of the bunch parameters as a matrix, the transport of a charged particle beam through a beamline can be described mathematically by matrix multiplications. Each beamline element is represented by a matrix $\mathbf{M_i}$ derived from the equations of motions that reflect the forces acting on a single particle. The entire beamline can be modelled by a single matrix $\mathbf{M}$ obtained by multiplication of the single element matrices,

$$\mathbf{M} = \prod_i \mathbf{M}_i. \tag{2.14}$$

In x dimension, the transport of a single particle with initial coordinates $\vec{x}(0)$ to a position z is described by

$$\vec{x}(z) = \mathbf{M}_x \vec{x}(0). \tag{2.15}$$

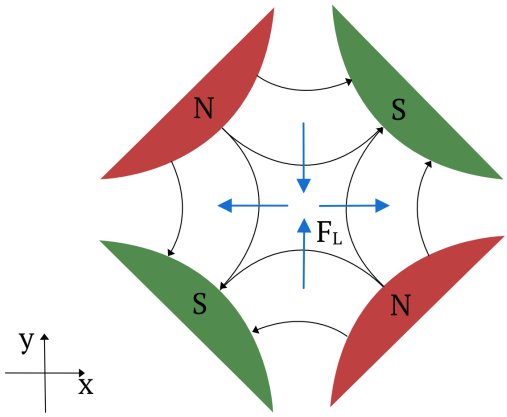

Figure 2.3: Schematic representation of a permanent magnet quadrupole. The magnetic field is indicated as black arrows, and the corresponding Lorentz force acting on positively charged particles travelling out of the paper plane is shown with blue arrows.

For particle bunches, the transport is described by a transformation of the beam ellipse. Analogously to equation 2.15, the transformation is calculated by

$$\boldsymbol{\sigma}_{\mathrm{x}}(z) = \boldsymbol{M}_{\mathrm{x}} \boldsymbol{\sigma}_{\mathrm{x}}(0) \boldsymbol{M}_{\mathrm{x}}^{\mathsf{T}}. \tag{2.16}$$

As an example, the transfer matrix describing a free drift writes

$$\mathbf{M}_{\mathrm{drift}} = \begin{pmatrix} 1 & z \\ 0 & 1 \end{pmatrix}. \tag{2.17}$$

This matrix is obtained by solving the equation of motion $\mathrm{d}^2x/\mathrm{d}z^2 = 0$, which reflects a particle that has no forces acting on it.

2.2.2 Quadrupole magnets

In this chapter, the focusing of charged particles by quadrupoles, for example by PMQs, is introduced following references [76] and [77]. The magnetic field of a quadrupole is characterised by its second magnetic moment, derived from the field multipole expansion. By definition, all other moments vanish. Figure 2.3 provides a visual representation of the quadrupole magnetic field, illustrating the effect of the Lorentz force on positively charged particles. In one dimension, particles are deflected towards the central axis, while in the other dimension, deflection occurs away from the axis. A bunch focusing effect is thus achieved in one dimension, while defocusing occurs in the other dimension.

The field strength is characterised by the quadrupole strength k, which writes for the x-dimension

$$k_{\mathrm{x}} = \frac{q}{p}\frac{dB_{\mathrm{y}}}{dx} \tag{2.18}$$

with q and p being the charge and momentum of the considered particle moving in the field. By convention, $k < 0$ describes a focusing and $k > 0$ a defocusing effect. To assess the focusing properties, a focal length f is calculated by

$$\frac{1}{f} = \pm\sqrt{|k|}\sin\left(\sqrt{|k|}L\right) \approx \pm|k|L \tag{2.19}$$

with L being the field lengths. The positive sign holds for the focusing plane, and the negative sign for the defocusing plane. For small values of $|k|L$, thus thin or weak magnets, the noted linear approximation holds, which depicts a practical formula assessing the influence of field strength and length on the focusing properties and is equal to a thin lens approximation.
While it is an intrinsic property of a quadrupole field to focus in one plane and defocus in the other, a beamline typically aims at bunch focusing in both dimensions. For that, a combination of quadrupoles can be employed. The simplest set-up is a doublet of quadrupoles with the field axes of the magnets being perpendicular to each other. This beamline design is typically referred to as Focusing Optic Defocusing Optic (FODO) structure. The PMQ-based LION beamline employed in this work is based on a doublet of equal strength, where the length of the first quadrupole L_1 is twice that of the second quadrupole $L_2 = 1/2 \cdot L_1$. For this configuration, reference [73] derives for the focal length

$$\frac{1}{f} = 2ak^2L_2^2 \pm kL_2 \tag{2.20}$$

with a being the distance between both quadrupoles. The positive sign describes the focusing-defocusing plane, while the negative sign the defocusing-focusing plane.

2.2.3 Solenoids

In this section, the focusing of charged particles by a solenoid is described based on reference [78]. The field inside the solenoid can be separated into its longitudinal and radial components. The longitudinal component is considered constant in the coil and

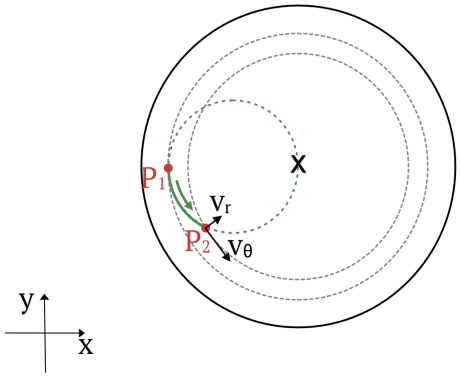

Figure 2.4: Schematic representation of a solenoid. The full black line represents the solenoid's bore size, and the black × the main axis. As an example, the lateral trajectory of a single exemplary particle transported through the solenoid out of the paper plane is shown: Before entering the solenoid, the particle's location is assumed to be P_1. While passing the solenoid, it moves on a helical trajectory indicated in dashed green. Depending on the length and the strength of the magnet, the particle arrives at a certain position on this helix when reaching the rear edge of the solenoid, here marked as P_2. The thereby conducted lateral movement is shown as full green line. Additionally, the particle velocity components in radial and azimuthal directions during the transport are indicated with black arrows. The focusing of a particle bunch is visualised as black dashed lines based on the initial and final position of the exemplarily chosen particle.

stepwise rising and falling at the edges. The radial field is assumed to be zero inside the coil, but it has a non-zero component at the edges of the solenoid. This radial component depends linearly on the distance from the main axis r. The lateral movement of a particle transported through a solenoid is visualised in figure 2.4. When a particle enters the solenoid with a trajectory parallel to the main axis, it experiences a force from the radial field in the azimuthal direction, resulting in a velocity component v_θ. Inside the coil, the particle is subjected to the longitudinal magnetic field due to its azimuthal momentum component, which induces a velocity component v_r. As a result, the particle follows a helical trajectory with a bending radius half of the initial radial offset, causing the particle trajectory to cross the main axis. In many set-ups the particle exits the solenoid before reaching the main axis. Upon leaving, the radial field once again acts on the particle's azimuthal momentum but in the opposite direction. This causes the particle's movement in the azimuthal direction to cease while the radial momentum is conserved. Outside the solenoid, the particle continues to move in a straight line towards

the extrapolated axis of the solenoid because of its remaining velocity component v_r. Analogously to the quadrupole description, the parameter k for solenoids is defined by

$$k = \frac{q}{2p} B_\mathrm{z} \tag{2.21}$$

in order to assess its focusing strength. Then, the focal length of a thin solenoid can be written as [79]

$$\frac{1}{f} = k^2 L. \tag{2.22}$$

It should be explicitly noted that a major difference to a quadrupole is the intrinsic focusing of a solenoid in both transversal planes. Thus, only one solenoid can be sufficient for an energy-selective and focusing beamline design. Comparison between the focus length of a quadrupole doublet and a solenoid given in equation 2.20 and 2.22, respectively, shows that both beamline designs depend quadratically on the particle charge and momentum. Further investigation and comparison between PMQ and solenoids can be found in reference [80]. It should be noted, however, that the specific focus properties ultimately depend on the individual set-up parameters.

2.3 Ionoacoustics

In this chapter, the theoretical background of ionoacoustic required for this work is described with a focus on analytical methods. This includes an accurate description of the expected acoustic waves to be measured as well as deducing analytical formulas for the calculation of bunch parameters. As a prerequisite, the dose deposition of protons in water is examined in section 2.3.1 using the analytical formulas developed in reference [81]. Section 2.3.2 contains the mathematical description of the generation and subsequent propagation of ionoacoustic waves based on literature [3, 82, 83]. In section 2.3.3, the influence of the detector entrance window is modelled analytically. In the next step, signal distortion due to the real detector and the amplification is considered in section 2.3.4. The last section 2.3.5 proposes a novel method for the fast deduction of the proton bunch energy spread.

2.3.1 Dose distribution of protons

The dose describes the energy loss per unit mass of particles in matter. The dose distribution in a medium can be calculated if the phase space of the particles is known and therefore is closely related to the particle bunch properties. As it is described in the subsequent section 2.3.2, the dose distribution defines, besides material dependent parameters and the detector geometry, the ionoacoustic wave. Thus, the dose distribution is the link between particle bunch properties and ionoacoustic wave.
Assuming the dose distribution $D(x, y, z)$ to be separable in axial and lateral dimensions, it can be modelled by

$$D(x, y, z) = D_{\text{lat}}(x, y) \cdot D_{\text{ax}}(z). \tag{2.23}$$

Thereby, axial refers to the axis of the mean proton momentum z and lateral to both perpendicular axes labelled x and y. For many cases, the lateral part of the dose distribution can be assumed Gaussian normalized to its integral over the transverse dimensions

$$D_{\text{lat}}(x, y) = \frac{1}{2\pi\sqrt{\sigma_x}\sqrt{\sigma_y}} \exp\left(-\left(\frac{x^2}{2\sigma_x} + \frac{y^2}{2\sigma_y}\right)\right). \tag{2.24}$$

with σ_x and σ_y being the standard deviation . The axial part of the dose distribution, also referred to as depth dose curve, is defined by the proton bunch energy distribution. For a Gaussian energy distribution, reference [81] derives

$$D_{\text{ax}}(z) = \Phi_0 \frac{e^{-\zeta^2/4}\sigma_{\text{R}}^{1/p}\Gamma(1/p)}{\sqrt{2\pi}\rho p\alpha^{1/p}(1+\beta R)} \cdot [\frac{1}{\sigma_R}\mathcal{D}_{-1/p}(-\zeta) + (\frac{\beta}{p} + \gamma\beta + \frac{\epsilon}{R})\mathcal{D}_{-1/p-1}(-\zeta)] \tag{2.25}$$

as an analytical formula holding for proton energies between 10 and 200 MeV in any homogeneous medium. The parameters are explained in the following. The derivation is based on the polynomial range-energy relationship

$$R = \alpha E^p \tag{2.26}$$

where the constants α and p are 0.0022 cmMeV^{-p} and 1.77 for water, respectively. While p is mostly projectile dependent, the parameter α can be obtained for other materials by fitting equation 2.26 to the range tables provided by the International Commission on Radiation Units and Measurements (ICRU) [84]. As an example, $\alpha_{\text{PA}} = 0.0018$,

$\alpha_{\mathrm{Alu}} = 0.0012$ and $\alpha_{\mathrm{Air}} = 2.2$ is calculated for the purposes of this work. The abbreviation PA is used to refer to polyamide. For better visibility, the depth z is substituted by

$$\zeta = \frac{R - z}{\sigma_R} \tag{2.27}$$

with the energy dependent proton range R and the width of the Gaussian range spectrum σ_{R}. The constant β describes the fluence reduction because of nuclear interactions, being 0.012 cm^{-1}, ρ the mass density, γ the locally absorbed energy in nonelastic nuclear interactions for which 0.6 is assumed and ϵ allows to consider a tail towards smaller energies in the energy spectrum. $\Gamma(x)$ is the gamma function and $\mathcal{D}_y(x)$ the parabolic cylinder function [85, 86]. Both functions are tabulated and also implemented in the SciPy Python library. For water,

$$D_{\mathrm{ax}}(z) = \frac{\Phi_0 e^{-\zeta^2/4} \sigma_{\mathrm{R}}^{0.565}}{1 + 0.012R} \cdot \left[\frac{11.26}{\sigma_R} \mathcal{D}_{-0.565}(-\zeta) + 0.157 \cdot \mathcal{D}_{-1.565}(-\zeta)\right] \tag{2.28}$$

depends on the range and the range spread of the particle bunch. Compared to equation 2.25, ϵ is set to zero because Gaussian energy spectra are considered in this work.
In the context of particle bunch monitoring, it is useful to connect the proton range and the width of the Gaussian range spectrum to the bunch parameters energy and energy spread. The proton range can be expressed in terms of energy with the polynomial range-energy relationship given in equation 2.26. The width of the Gaussian range distribution σ_{R} is connected to the initial energy spread σ_{E} by [81]

$$\sigma_{\mathrm{R}}^2 = \sigma_{\mathrm{mono}}^2 + \sigma_{\mathrm{E}}^2 \left(\frac{\mathrm{d}R}{\mathrm{d}E}\right)^2 = \sigma_{\mathrm{mono}}^2 + \sigma_{\mathrm{E}}^2 \alpha^2 p^2 E^{2p-2}. \tag{2.29}$$

The first addend describes the range straggling caused by the statistical interaction of the protons with water molecules. It can be thought of as the width of the Gaussian range distribution of a monoenergetic bunch with energy E and is thus labelled σ_{mono}. For water, it can be determined analytically by

$$\sigma_{\mathrm{mono}}^2 = \alpha' \frac{p^2 \alpha^{2/p}}{3 - 2/p} R^{3-2/p} = 0.012 R^{0.935}. \tag{2.30}$$

The parameter α' is given by $\frac{1}{4\pi\epsilon_0^2} e^4 NZ$, NZ being the electron number density, yielding $\alpha' = 0.0087$ $\mathrm{MeV}^2/\mathrm{cm}$ for water. More generally, the range straggling can be modelled as function of the penetration depth z by replacing the upper integration limit R_0 in

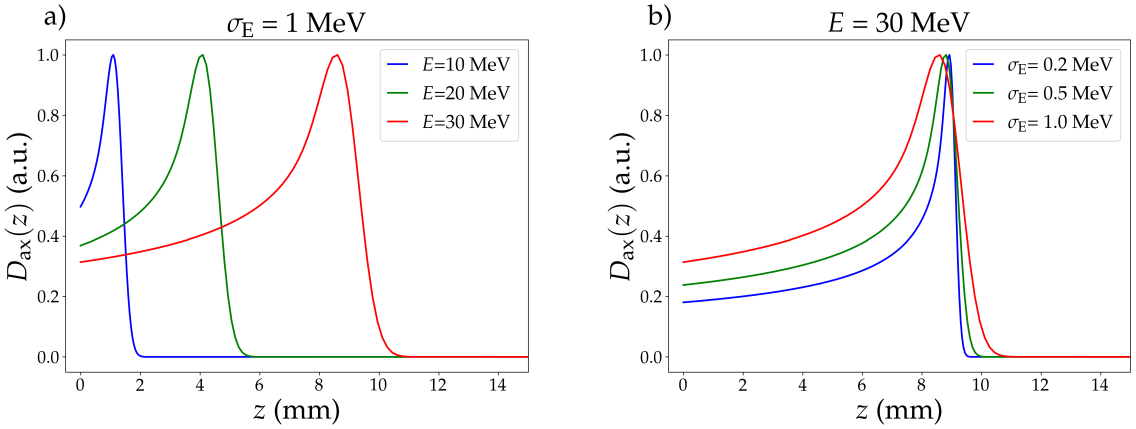

Figure 2.5: Analytical calculated depth dose curves in water according to equation 2.28. In a), the mean energy is varied while the energy spread is fixed to $\sigma_E = 1$ MeV. In b), the energy spread varies while the mean energy is fixed to $E = 30$ MeV.

formula B.4, reference [81], with z yielding

$$\sigma^2_{\text{mono}}(z) = \alpha' p^2 \alpha^{2/p} \int_0^z (R - z')^{2-2/p} dz'. \tag{2.31}$$

The second addend in equation 2.29 describes the effect of the initial energy spread $\sigma_{E,0}$ on the range distribution and is based on linearizing equation 2.26 around the mean energy E which is valid for a small energy spread $\sigma_E \ll E$.
Exemplary depth dose curves in water for proton bunches with mean energies between 10 and 30 MeV and energy spreads between 0.2 and 1 MeV are shown in figure 2.5.

2.3.2 Generation and propagation of ionacoustic waves

Transitioning to the basics of ionoacoustic waves, more information can be found in references [3, 82, 83]. The generation and propagation of an ionoacoustic wave are described by the general wave equation with a source term

$$\left(\nabla^2 - \frac{1}{c^2}\frac{\partial^2}{\partial t^2}\right) p(\vec{r}, t) = -\frac{\Gamma}{c^2}\frac{\partial}{\partial t} H(\vec{r}, t) \tag{2.32}$$

with the sound velocity in the corresponding medium c, the temperature and material dependent Grüneisen parameter Γ, the pressure $p(\vec{r}, t)$. $H(\vec{r}, t)$ is the heating function

and has the units J/(m$^3 \cdot$ s). The Grüneisen parameter can be calculated by

$$\Gamma = \frac{\beta}{\kappa \rho C_\mathrm{V}} \tag{2.33}$$

with the volume thermal expansion coefficient β, the isothermal compressibility coefficient κ and the volume specific heat capacity C_V. Commonly used is also the pressure specific heat capacity C_P being related to C_V by $C_\mathrm{P} = c^2 \kappa \rho C_\mathrm{V}$. Using a Green's function approach [87], the general solution of equation 2.32 is

$$p(\vec{r}, t) = \frac{\Gamma}{4\pi c^2} \frac{\partial}{\partial t} \int d^3\vec{r}' \frac{1}{|\vec{r} - \vec{r}'|} H(\vec{r}', t - \frac{|\vec{r} - \vec{r}'|}{c}). \tag{2.34}$$

describing the pressure amplitude at a position $\vec{r}$ of an ionoacoustic wave originated at $\vec{r}'$. Assuming that there are no spatio-temporal couplings, the heating function can be separated into its spatial and temporal dependent part

$$H\left(\vec{r}, t\right) = H_\mathrm{s}\left(\vec{r}\right) \cdot H_\mathrm{t}\left(t\right) \tag{2.35}$$

with the spatial part of the heating function being the energy density connected to the dose distribution by multiplication with the material's mass density, thus having the unit J/m^3. Under this assumption, equation 2.34 becomes

$$p(\vec{r}, t) = \frac{\Gamma}{4\pi c^2} \frac{\partial}{\partial t} \int d^3\vec{r}' \frac{H_\mathrm{s}(\vec{r}')}{|\vec{r} - \vec{r}'|} H_\mathrm{t}(t - \frac{|\vec{r} - \vec{r}'|}{c}). \tag{2.36}$$

Along with the formulas elaborated in the previous section 2.3.1, equation 2.36 allows a fully analytical calculation of the pressure amplitude in dependence on the proton bunch parameters, assuming that the temporal part of the heating function H_t is known and integrable.

A further simplification is possible under thermal and stress confinement. For thermal confinement, the initial heating and, thus, the energy deposition must occur in a timescale shorter than the heat diffusion in the volume of the energy deposition. The thermal relaxation time τ_thermal can be calculated by

$$\tau_\mathrm{thermal} = \frac{b^2}{\alpha_\mathrm{thermal}} \tag{2.37}$$

with the spatial extent of the energy deposition b and the thermal diffusivity α_thermal which is 0.14 mm^2/s for water at 20°C [88]. Similarly, stress confinement means the

initial heating must occur in a timescale shorter than the propagation of the ionoacoustic wave in the volume of the energy deposition. The stress confinement time τ_{stress} is thus defined by

$$\tau_{\text{stress}} = \frac{b}{c}. \tag{2.38}$$

Therefore, both thermal and stress relaxation time depend on the medium and the extent of the energy deposition. For a proton beam with a BP width of 500 μm width, 1.8 s and 0.33 μs can be calculated as exemplary values for the thermal and stress relaxation time, respectively. Under stress confinement, the temporal part of the heating function can be modelled by a delta function $H_{\text{t}}(t - \frac{|\vec{r}-\vec{r}'|}{c}) = \delta(t - \frac{|\vec{r}-\vec{r}'|}{c})$. This simplifies equation 2.36 further, yielding

$$p(\vec{r}, t) = \frac{\Gamma}{c}\frac{\partial}{\partial t}\int dS \frac{1}{ct} H_{\text{s}}(\vec{r}') \tag{2.39}$$

with S being the surface of a sphere with radius $R = |\vec{r} - \vec{r}'| = ct$ [19]. The integral expresses that at every time t, the pressure generated on a sphere with the distance $R = ct$ from the detection point is recorded, further accounting for the 1/R decrease of the pressure amplitude with the distance from the pressure source. While, in principle, this integral can be solved for any arbitrary dose distribution, two practical simplifications for particular lateral dose distributions are introduced in the following paragraphs.

One-dimensional model In thermal and stress confinement, an analytical solution to equation 2.36 can be found for a dose distribution of the form $H_{\text{s}}(\vec{r}') = \delta(x')\delta(y')h(z')$. In that case, the axial pressure amplitude is

$$\begin{aligned} p(z,t) &= \frac{\Gamma}{4\pi c}\frac{\partial}{\partial t}\int d^3\vec{r}' \frac{1}{|z-z'|}\delta(x')\delta(y')h(z')\delta(t - \frac{|z-z'|}{c}) \\ &= \frac{\Gamma}{4\pi c}\frac{\partial}{\partial t}\left(\frac{h(z')}{z-z'}\right)\Big|_{z'=z-ct} \\ &= \frac{\Gamma}{4\pi c^2}\frac{\partial}{\partial t}\frac{h(z-ct)}{t}. \end{aligned} \tag{2.40}$$

Thereby, $h(z')$ is proportional to the depth dose curve and has the unit J/m. Equation 2.40 visualises the important fact that a pressure wave is emitted through gradients in energy deposition.

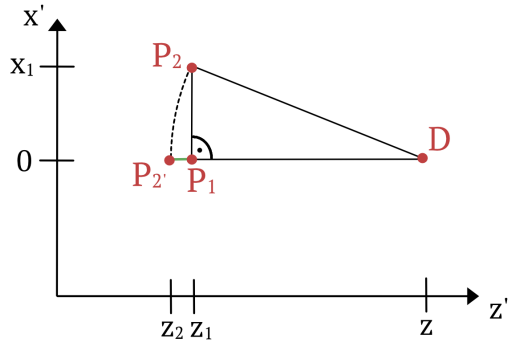

Figure 2.6: Influence of lateral extended bunches on the axial ionoacoustic signal. A pressure wave generated at P_2 will arrive later at the detection point D compared to a wave starting to propagate at P_1. P_2 can be projected on the $x = 0$ axis under the condition that the distance to the detection point D stays constant, resulting in the point $P_{2'}$.

Equal width model Instead of a transverse delta-function, a Gaussian lateral distribution with Equal Width (EW) is considered in both transverse dimensions (radial symmetry). Figure 2.6 visualised the effect of a laterally extended bunch on the ionoacoustic wave at a detection position D: The wave generated at P_1 and propagating towards D arrives at a time $t_1 = cz_1$. A wave generated at P_2, emitted at the same axial coordinate $z = z_1$ but with a lateral shift of x_1, will arrive later at D, i.e. at $t_2 = cz_2 = c\sqrt{z_1^2 + x_1^2}$. This is equivalent to considering the source of the wave being located at $P_{2'}$; thus, the lateral extension can be projected under an angle on the z-axis. It should be noted that this statement holds only for a single detection point and not for laterally extended detector geometries.

While this concept visualises the influence of a lateral bunch extension on the axial signal in general, a mathematically exact solution can be derived for Gaussian distributions of EW in both lateral dimensions x' and y' [59, 89]. For that case, the three-dimensional heating function is modelled by

$$H_\mathrm{s}(\vec{r}') = \frac{1}{2\pi\sigma^2} \exp\left(-\frac{x'^2 + y'^2}{2\sigma^2}\right) h_\mathrm{s}(z') \tag{2.41}$$

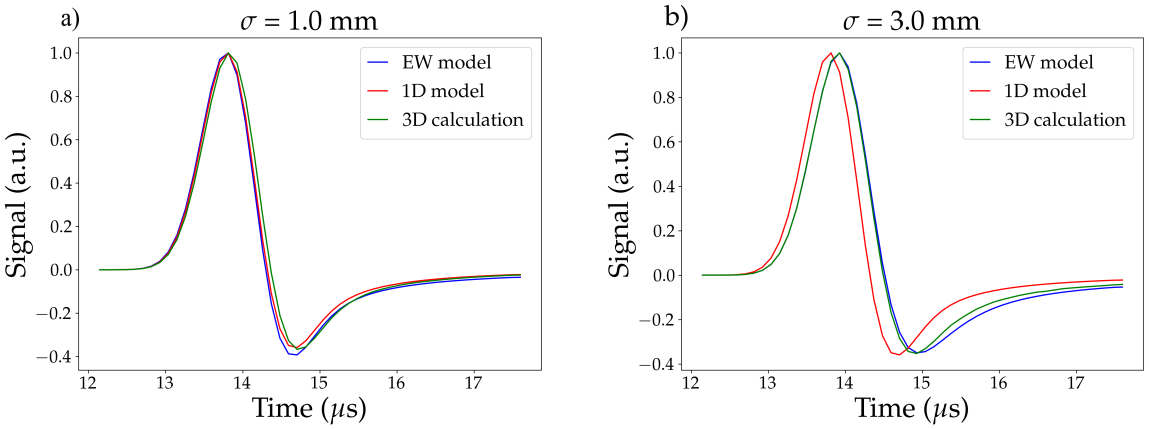

Figure 2.7: Ionoacoustic signals calculated based on the equal width (EW) model, the one-dimensional (1D) model and the full three-dimensional (3D) calculation for a mean energy of $E = 30$ MeV and an energy spread of $\sigma_{\mathrm{E}} = 1$ MeV. The lateral spread varies between a) $\sigma = 1$ mm and b) $\sigma = 3$ mm. The transducer position is chosen to be 30 mm behind the beginning of the water reservoir.

in which σ is the standard deviation of the lateral Gaussian distributions. Inserting equation 2.41 into equation 2.36 yields

$$p_{\mathrm{EW}}(z,t) = \frac{\Gamma}{4\pi c\sigma^2}\frac{\partial}{\partial t}\left(\exp\left(\frac{-c^2t^2}{2\sigma^2}\right)\int_{z+ct}^{z-ct} dz' \exp\left(\frac{(z-z')^2}{2\sigma^2}\right) h_{\mathrm{s}}(z')\right). \tag{2.42}$$

Figure 2.7 compares the pressure wave calculated with the full three-dimension integral given in equation 2.39 to the one-dimensional and the EW model. To fulfil the requirements of the EW model, only laterally Gaussian dose distributions with EWs are considered. Figure 2.7 shows example calculations for $\sigma = 1.0$ mm (a) and $\sigma = 3.0$ mm (b). While in 2.7a) all three models yield very similar results; the one-dimensional model deviates from the EW model and the full three-dimensional calculation in 2.7b). Theoretically, the EW model and the full three-dimensional calculation should yield the same curve, given that the EW model offers an exact solution of the three-dimensional calculation. The minor deviations observed are due to the numerical integral solving process utilised for the full three-dimensional calculation, while the EW model provides an accurate analytical solution. The deviation observed in the one-dimensional model illustrates the limited applicability of this model for larger lateral sizes. The validity of the one-dimensional model depends on the ratio between the lateral size of the bunch and its distance to the detector.

2.3.3 Influence of the detector entrance window

So far, only the wave emitted due to the dose distribution in water has been considered. In most experimental set-ups, a thin foil separates the water from the surrounding air or vacuum, which affects the signal detected by the axial ultrasonic transducer. The influence of this detector entrance window on the ionoacoustic signal shape can be divided into two components: First, a portion of the acoustic wave generated in water propagates towards the entrance window, reflects off it, and then travels towards the transducer location. Second, the energy deposition gradient at the entrance window generates an additional ionoacoustic pulse. This section presents the entrance window model, which incorporates these two additional influences, completing the mathematical model of the axial ionoacoustic signal. The model considers that the reflection and wave generation occur at two interfaces: air-foil and foil-water. To describe the multiple reflections caused by the etalon structure of the entrance window in a concise manner, the derivation is primarily carried out in the frequency domain. Initially, the model is formulated for particle bunches without lateral extension. Subsequently, it is extended to account for lateral Gaussian distributions with equal widths in both dimensions.

Ionoacoustic signal in frequency domain Starting from equation 2.36, the temporal part of the heating function is modelled by a delta function in frequency domain $H_\mathrm{t}(t) = \delta(t) = \int_{-\infty}^{\infty} d\omega \exp(i\omega t)$ yielding

$$p(\vec{r},t) = \frac{\Gamma}{4\pi c^2} \int d^3\vec{r}' \frac{H_\mathrm{s}(\vec{r}')}{|\vec{r}-\vec{r}'|} \int_0^\infty d\omega \; i\omega \exp\left(i\omega\left(t - \frac{|\vec{r}-\vec{r}'|}{c}\right)\right). \tag{2.43}$$

The pressure wave in time is

$$p(\vec{r},t) = \int_0^\infty d\omega \; \hat{p}(\vec{r},\omega) \exp(i\omega t). \tag{2.44}$$

By comparing equation 2.43 and 2.44, the pressure wave in frequency domain is identified as

$$\hat{p}(\vec{r},\omega) = \frac{i\omega\Gamma}{4\pi c^2} \int d^3\vec{r}' \frac{H_\mathrm{s}(\vec{r}')}{|\vec{r}-\vec{r}'|} \exp\left(-i\frac{\omega}{c}|\vec{r}-\vec{r}'|\right). \tag{2.45}$$

To analyse the axial signal shape in this chapter, the detection point is chosen to be at $\vec{r} = (x,y,z) = (0,0,z)$. Following the one-dimensional model for the axial signal described in the preceding section 2.3.2, which assumes a delta-spiked lateral particle

distribution in both dimensions, $H_\mathrm{s}(\vec{r}) = \delta(x)\delta(y)h(z)$ holds. Based on this assumption, the expression for the axial signal in the frequency domain can be written as

$$\hat{p}(z,\omega) = \frac{i\omega\Gamma}{4\pi c^2} \exp\left(-i\frac{\omega}{c}z\right) \int_0^z dz' \; \frac{h(z')}{z-z'} \exp\left(i\frac{\omega}{c}z'\right). \tag{2.46}$$

So far, the start of the dose distribution of the protons in water was assumed to be at $z' = 0$ for simplicity. Now, an entrance window geometry as visualised in figure 2.8a) is considered, which defines the beginning of the water phantom more generally at $z' = z_0 + d_\mathrm{f}$, with d_f being the thickness of the entrance window. Taking this into account, the ionoacoustic wave component of the non-reflected BP signal, denoted as $\hat{p}_\mathrm{BP}(z,\omega)$, can be expressed as

$$\hat{p}_\mathrm{BP}(z,\omega) = \frac{i\omega\Gamma}{4\pi c^2} \exp\left(-i\frac{\omega}{c}z\right) \int_{z_0+d_\mathrm{f}}^z dz' \; \frac{h(z')}{z-z'} \exp\left(i\frac{\omega}{c}z'\right). \tag{2.47}$$

Reflected Bragg peak signal The ionoacoustic wave generated in water and travelling in $-z'$ direction towards the entrance window is modulated in phase and amplitude at both material interfaces, which is evolved in the following. When the wave reaches the interface water-foil, part of the wave is reflected. Thereby, the amplitude is modulated by the reflection coefficient r_wf with the subscripts reflecting the material interface. Generally, the reflection coefficient r_{12} of a wave propagating through medium 1 and hitting the surface of medium 2 is calculated by

$$r_{12} = \frac{Z_2 - Z_1}{Z_1 + Z_2}, \tag{2.48}$$

where Z_i is the acoustic impedance of the medium i writing

$$Z_i = \rho_i c_i. \tag{2.49}$$

Part of the incoming wave is also transmitted into the foil medium; its amplitude is modified by the transmission coefficient t_wf. Generally, the transmission coefficient t_{12} of a wave propagating through medium 1 and transmitting into medium 2 is calculated by

$$t_{12} = \frac{2Z_2}{Z_1 + Z_2}. \tag{2.50}$$

This wave reaches the interface foil-air, where again reflection and transmission occur. Only the reflected part of the wave propagating in $+z'$ is considered here, as the

transmitted part will not reach the detection point. The amplitude of the reflected wave is modulated by r_{fa}. When reaching the foil-water interface, the transmitted part of the wave propagates towards the detection point. It is modulated in amplitude by $t_{\mathrm{wf}} r_{\mathrm{fa}} t_{\mathrm{fw}}$ and phase shifted by $\left(\frac{2d_{\mathrm{f}}}{c_{\mathrm{f}}}\right)$ compared to the wave, which was directly reflected at the water-foil interface and not travelling through the entrance foil. The part of the wave reflected in $-z'$ direction is bouncing again in the foil cavity, leading to a phase shift of $\frac{2d_{\mathrm{f}}}{c_{\mathrm{f}}}$ and an amplitude modulation of $r_{\mathrm{fa}} r_{\mathrm{fw}}$ per round trip. Thus, the BP signal reflected at the entrance foil $\hat{p}_{\mathrm{rBP}}(z,\omega)$ is described by

$$\begin{aligned}\hat{p}_{\mathrm{rBP}}(z,\omega) = \frac{i\omega\Gamma}{4\pi c^2} \exp\left(-i\frac{\omega}{c}z\right) \int_{z_0+d_{\mathrm{f}}}^{z} dz' \, \frac{h(z')}{z-z'} \exp\left(-i\frac{\omega}{c}z'\right) \\ \cdot \left[r_{\mathrm{wf}} + t_{\mathrm{wf}} r_{\mathrm{fa}} t_{\mathrm{fw}} \exp\left(-i\frac{\omega}{c_{\mathrm{f}}}2d_{\mathrm{f}}\right) \sum_{n=0}^{\infty} \left(r_{\mathrm{fa}} r_{\mathrm{fw}} \exp\left(-i\frac{\omega}{c_{\mathrm{f}}}2d_{\mathrm{f}}\right)\right)^n\right]\end{aligned} \tag{2.51}$$

This formula can be simplified using

$$t_{21} = 1 + r_{12}, \quad r_{12} = -r_{21} \tag{2.52}$$

and further, the geometric series yielding

$$\begin{aligned}\hat{p}_{\mathrm{rBP}}(z,\omega) = \frac{i\omega\Gamma}{4\pi c^2} \exp\left(-i\frac{\omega}{c}z\right) \int_{z_0+d_{\mathrm{f}}}^{z} dz' \, \frac{h(z')}{z-z'} \exp\left(-i\frac{\omega}{c}z'\right) \\ \cdot \frac{r_{\mathrm{wf}} + r_{\mathrm{fa}} \exp\left(-i\frac{\omega}{c_{\mathrm{f}}}2d_{\mathrm{f}}\right)}{1 + r_{\mathrm{wf}} r_{\mathrm{fa}} \exp\left(-i\frac{\omega}{c_{\mathrm{f}}}2d_{\mathrm{f}}\right)}.\end{aligned} \tag{2.53}$$

Discontinuity induced ionoacoustic waves At the entrance window, both mass density and hence deposited energy density as well as the Grüneisen parameter change suddenly. This gradient gives rise to the ionoacoustic signal. The pressure signal generated at the entrance window can be separated into two waves generated at each material interface and subsequent reflections. To describe the pressure generated at a single interface between two media, a generic model is set up. A material discontinuity is assumed at $z = z_0$ between a medium 1 ($z > z_0$) and a medium 2 ($z < z_0$), as illustrated in figure 2.8b). Each medium is characterised by its Grüneisen parameter Γ_1 and Γ_2 and speed of sound c_1 and c_2, respectively. Thus, c and Γ cannot be considered independent of z anymore. The heating function is assumed to be constant around the discontinuity and

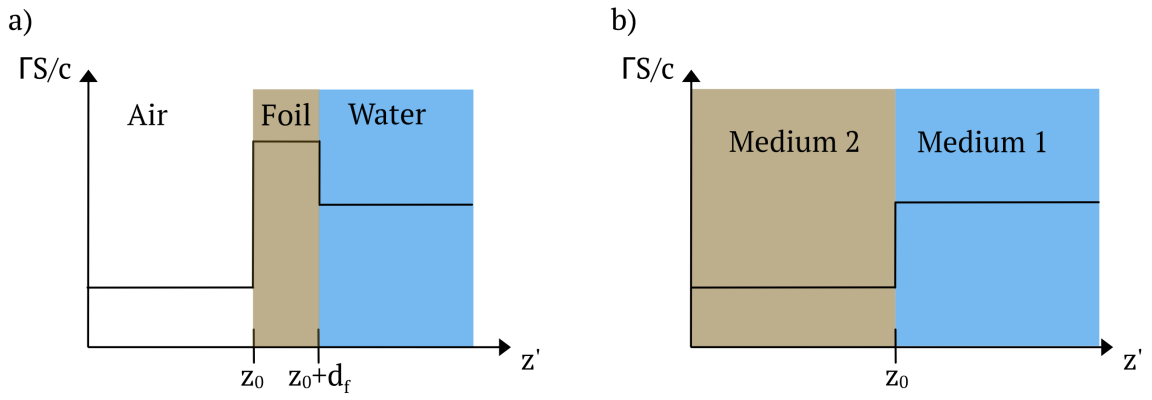

Figure 2.8: a) Typical detector set-up based on a thin foil with thickness d_f separating the water phantom from the surrounding air leading to two material transitions. The variables are explained in the main text. b) Graphical visualisation of a discontinuity between two media.

is therefore modelled by

$$h(z') = (S_2 - S_1)\Theta(z' - z_0) + S_1 = \begin{cases} S_1 & \text{for } z' > z_0 \\ S_2 & \text{for } z' < z_0 \end{cases} \tag{2.54}$$

with $\Theta(z')$ being the Heaviside step function. Inserting equation 2.54 into equation 2.46 results in the pressure wave, which is travelling towards a detection point in medium 1 writing

$$\hat{p}(z,\omega) = \frac{i\omega}{4\pi} \exp\left(-i\frac{\omega}{c_1}z\right) \int_{z_a}^{z_b} dz' \; \frac{1}{z - z'} \frac{\Gamma(z')}{c(z')^2} \left((S_2 - S_1)\Theta(z' - z_0) + S_1\right) \exp\left(i\frac{\omega}{c}z'\right) \tag{2.55}$$

with the integration limits enclosing the discontinuity, thus $z_a < z_0$ and $z_b > z_0$. Rearranging the integral and executing the integration yields

$$\begin{aligned} \hat{p}(z,\omega) &= \frac{i\omega}{4\pi} \exp\left(-i\frac{\omega}{c_1}z\right) \left[\int_{z_a}^{z_0} dz' \; \frac{1}{z - z'} \frac{\Gamma_2}{c_2^2} S_1 \exp\left(i\frac{\omega}{c_1}z'\right) + \int_{z_0}^{z_b} dz' \frac{\Gamma_1}{c_1^2} S_2 \exp\left(i\frac{\omega}{c_1}z'\right)\right] \\ &= \frac{1}{4\pi} \exp\left(-i\frac{\omega}{c_1}z\right) \left[\frac{1}{z - z'} \frac{\Gamma_2}{c_2} S_1 \exp\left(i\frac{\omega}{c_1}z'\right)\Big|_{z_a}^{z_0} + \frac{1}{z - z'} \frac{\Gamma_1}{c_1} S_2 \exp\left(i\frac{\omega}{c_1}z'\right)\Big|_{z_0}^{z_b}\right]. \end{aligned} \tag{2.56}$$

The left addend describes the pressure wave generated in medium 2 and propagating towards the detection point. This wave needs to transmit the interface from medium 2

into medium 1 and thus must be multiplied with the transmission coefficient t_{21}. The right term represents the pressure wave generated in medium 1. This wave consists of two parts: one part travels directly towards the detection point, while the other part first moves towards the interface, is immediately reflected, and then propagates towards the detection point. The amplitude of the reflected wave is modulated by the factor r_{12} compared to the initial wave, resulting in an overall amplitude modulation of $(1 - r_{12})$. The minus sign accounts for the phase shift of the wave initially emitted towards the interface. If the integration limits were evaluated at $z' = z_\mathrm{a}$ and $z' = z_\mathrm{b}$, it would describe a pressure wave generated at the locations z_a and z_b, respectively. In mathematical terms, these integration limits correspond to a discontinuity in the heating function, where $h(z') = 0$ for $z' < z_\mathrm{a}$ and $z' < z_\mathrm{b}$. However, in this specific case, only the pressure wave generated at a single interface $z = z_0$ should be modelled. Therefore, the integrals are only evaluated at this position, and the contributions from $z' = z_\mathrm{a}$ and $z' = z_\mathrm{b}$ are discarded, as they do not contribute to the pressure wave at the interface. Accounting for the amplitude modulation and the adjusted integration boundaries, the expression for the acoustic wave generated at a material interface

$$\begin{aligned}\hat{p}(z,\omega) &= \frac{1}{4\pi(z-z_0)} \exp\left(-i\frac{\omega}{c_1}z\right)\left[t_{21}\frac{\Gamma_2}{c_2}S_2 \exp\left(i\frac{\omega}{c_1}z_0\right) - (1-r_{12})\frac{\Gamma_1}{c_1}S_1 \exp\left(i\frac{\omega}{c_1}z_0\right)\right] \\ &= \frac{1}{4\pi(z-z_0)} \exp\left(-i\frac{\omega}{c_1}(z-z_0)\right) t_{21}\left(\frac{\Gamma_2}{c_2}S_2 - \frac{\Gamma_1}{c_1}S_1\right) \\ &= \frac{A_{12}}{4\pi(z-z_0)} t_{21} \exp\left(-i\frac{\omega}{c_1}(z-z_0)\right)\end{aligned} \tag{2.57}$$

is obtained with $A_{12} = \left(\frac{\Gamma_2}{c_2}S_2 - \frac{\Gamma_1}{c_1}S_1\right)$.

Entrance window signal The ionoacoustic entrance window signal is generated at the two interfaces of the entrance window, as visualised in figure 2.8a). This signal undergoes modifications through subsequent reflections at the window surfaces. Building upon the description of ionoacoustic wave generation at a single material transition developed in the preceding paragraph, the entrance window signal can be decomposed into three distinct parts, which are elaborated upon in the following.

- The discontinuity between foil and water causes a signal travelling in $+z'$ direction directly towards the detection point. This wave is not further modified by material transitions, and the mathematical description is directly described by equation

2.57,

$$\begin{aligned}\hat{p}_{\mathrm{wf,direct}}(z,\omega) &= \frac{A_{\mathrm{wf}}}{4\pi(z-z_0)} t_{\mathrm{fw}} \exp\left(-i\frac{\omega}{c_{\mathrm{w}}}\left(z-z_0-d_{\mathrm{f}}\right)\right) \\ A_{\mathrm{wf}} &= \left(\frac{\Gamma_{\mathrm{f}}}{c_{\mathrm{f}}}S_{\mathrm{f}} - \frac{\Gamma_{\mathrm{w}}}{c_{\mathrm{w}}}S_{\mathrm{w}}\right).\end{aligned} \tag{2.58}$$

- The discontinuity between foil and water also causes a signal emitted in $-z'$ direction towards the foil-air boundary. When reaching this boundary, a part of the wave is reflected and propagates in $+z'$ direction. At the foil-water boundary, the transmitted wave travels towards the detection point while the rest of the intensity is reflected and travels again towards the foil-air boundary. Thus, a cavity is formed, which generates acoustic pulses shifted by $2d_{\mathrm{f}}/c_{\mathrm{w}}$ and an amplitude change by a factor of $r_{\mathrm{fw}}r_{\mathrm{fa}}$. The contribution at the detection point z is given by

$$\begin{aligned}\hat{p}_{\mathrm{fw,indirect}}(z,\omega) = \frac{A_{\mathrm{fw}}}{4\pi(z-z_0)} &\exp\left(-i\frac{\omega}{c_{\mathrm{w}}}\left(z-z_0-d_{\mathrm{f}}\right)\right) t_{\mathrm{wf}} r_{\mathrm{fa}} t_{\mathrm{fw}} \exp\left(-i\frac{\omega}{c_{\mathrm{f}}}2d_{\mathrm{f}}\right) \\ &\cdot \sum_{n=0}^{\infty}\left(r_{\mathrm{fw}}r_{\mathrm{fa}}\exp\left(-i\frac{\omega}{c_{\mathrm{f}}}2d_{\mathrm{f}}\right)\right)^n \\ A_{\mathrm{fw}} = &\left(\frac{\Gamma_{\mathrm{w}}}{c_{\mathrm{w}}}S_{\mathrm{w}} - \frac{\Gamma_{\mathrm{f}}}{c_{\mathrm{f}}}S_{\mathrm{f}}\right)\end{aligned} \tag{2.59}$$

- The discontinuity between air and foil leads to the emission of an acoustic wave. At that interface, only the part of the wave emitted in $+z'$ direction, thus towards the detection point, must be considered. When reaching the foil-water interface, part of the wave is transmitted, and the other part is reflected. Similar as in the previous item, acoustic pulses with a phase shift of $2d_{\mathrm{f}}/c_{\mathrm{w}}$ and a factor of $r_{\mathrm{fw}}r_{\mathrm{fa}}$ modulated amplitude reach the detection point:

$$\begin{aligned}\hat{p}_{\mathrm{fa}}(z,\omega) = \frac{A_{\mathrm{fa}}}{4\pi(z-z_0)} &\exp\left(-i\frac{\omega}{c_{\mathrm{w}}}\left(z-z_0-d_{\mathrm{f}}\right)\right) t_{\mathrm{af}} t_{\mathrm{fw}} \exp\left(-i\frac{\omega}{c_{\mathrm{f}}}d_{\mathrm{f}}\right) \\ &\cdot \sum_{n=0}^{\infty}\left(r_{\mathrm{fw}}r_{\mathrm{fa}}\exp\left(-i\frac{\omega}{c_{\mathrm{f}}}2d_{\mathrm{f}}\right)\right)^n \\ A_{\mathrm{fa}} = &\left(\frac{\Gamma_{\mathrm{a}}}{c_{\mathrm{a}}}S_{\mathrm{a}} - \frac{\Gamma_{\mathrm{f}}}{c_{\mathrm{f}}}S_{\mathrm{f}}\right)\end{aligned} \tag{2.60}$$

Summing up these three contributions yields the complete window signal

$$\begin{aligned}\hat{p}_{\mathrm{WS}}(z,\omega) &= \hat{p}_{\mathrm{wf,direct}}(z,\omega) + \hat{p}_{\mathrm{fw,indirect}}(z,\omega) + \hat{p}_{\mathrm{fa}}(z,\omega) \\ &= \frac{1}{4\pi(z-z_0)} \exp\left(-i\frac{\omega}{c_{\mathrm{w}}}(z-z_0-d_{\mathrm{f}})\right) \frac{1-r_{\mathrm{wf}}}{1+r_{\mathrm{wf}}r_{\mathrm{fa}}\exp\left(-i\frac{\omega}{c_{\mathrm{f}}}2d_{\mathrm{f}}\right)} \\ &\cdot \left[A_{\mathrm{wf}}\left(1-r_{\mathrm{fa}}\exp\left(-i\frac{\omega}{c_{\mathrm{f}}}2d_{\mathrm{f}}\right)\right) + A_{\mathrm{fw}}(1-r_{\mathrm{fa}})\exp\left(-i\frac{\omega}{c_{\mathrm{f}}}d_{\mathrm{f}}\right)\right].\end{aligned} \tag{2.61}$$

One-dimensional entrance window model In order to describe the complete ionoacoustic signal $\hat{p}(z,\omega)$ at an axial detection position, the contributions of the direct BP signal $\hat{p}_{\mathrm{BP}}(z,\omega)$, the reflected BP signal $\hat{p}_{\mathrm{rBP}}(z,\omega)$ and the entrance window signal $\hat{p}_{\mathrm{WS}}(z,\omega)$ are added, yielding

$$\begin{aligned}\hat{p}(z,\omega) &= \hat{p}_{\mathrm{BP}}(z,\omega) + \hat{p}_{\mathrm{rBP}}(z,\omega) + \hat{p}_{\mathrm{WS}}(z,\omega) \\ &= \frac{1}{4\pi}\exp\left(-i\frac{\omega}{c}z\right)\Bigg[\frac{i\omega\Gamma_{\mathrm{w}}}{c_{\mathrm{w}}^2}\int_{z_0+d_{\mathrm{f}}}^{z} dz'\ \frac{h(z')}{z-z'}\exp\left(i\frac{\omega}{c_{\mathrm{w}}}z'\right) \\ &+ \frac{i\omega\Gamma_{\mathrm{w}}}{c_{\mathrm{w}}^2}\int_{z_0+d_{\mathrm{f}}}^{z} dz'\ \frac{h(z')}{z-z'}\exp\left(-i\frac{\omega}{c_{\mathrm{w}}}z'\right) \\ &+ \frac{1}{z-z_0}\exp\left(i\frac{\omega}{c_{\mathrm{w}}}(z_0+d_{\mathrm{f}})\right)\frac{1-r_{\mathrm{wf}}}{1+r_{\mathrm{wf}}r_{\mathrm{fa}}\exp\left(-i\frac{\omega}{c_{\mathrm{f}}}2d_{\mathrm{f}}\right)} \\ &\cdot \left[A_{\mathrm{wf}}\left(1-r_{\mathrm{fa}}\exp\left(-i\frac{\omega}{c_{\mathrm{f}}}2d_{\mathrm{f}}\right)\right) + A_{\mathrm{fw}}(1-r_{\mathrm{fa}})\exp\left(-i\frac{\omega}{c_{\mathrm{f}}}d_{\mathrm{f}}\right)\right]\Bigg].\end{aligned} \tag{2.62}$$

The temporal signal shape can be calculated by performing the inverse Fourier transform of the frequency-domain signal

$$p(z,t) = \mathrm{IFT}\left(\hat{p}(z,\omega)\right). \tag{2.63}$$

This can be achieved, for example, through the use of an inverse discrete Fourier transform algorithm.

Three-dimensional entrance window model Now, proton bunches with a Gaussian lateral distribution of equal width are considered. Mathematically, this concept is formulated as the EW model given in equation 2.42. The input for this model is the axial heating function $h(z'-(z_0+d_{\mathrm{f}}))$, further referred to as effective axial heating function. The argument of the heating function takes into account the shifted coordinate system $z' \to z'-(z_0+d_{\mathrm{f}})$, which allows the position of the entrance window's foil-water

interface to be at $z' = z_0 + d_\mathrm{f}$. Up to now, the entrance window model is derived based on the assumptions of the one-dimensional model as evolved in section 2.3.2. Therefore, equations 2.40 and 2.63 can be compared yielding

$$\mathrm{IFT}\left(\hat{p}(z,\omega)\right) = \frac{\Gamma}{4\pi c^2}\frac{\partial}{\partial t}\frac{h(z-ct)}{t}. \tag{2.64}$$

By integrating this equation from $t_1 = 0$ to $t_2 = (z - z' + z_0 + d_\mathrm{f})/c$, the required effective axial heating function is found as

$$h(z' - z_0 - d_\mathrm{f}) = \frac{4\pi c}{\Gamma}(z - z' + z_0 + d_\mathrm{f}) \int_0^{(z-z'+z_0+d_\mathrm{f})/c} dt\ \mathrm{IFT}\left(\hat{p}(z,\omega)\right), \tag{2.65}$$

assuming that $h(z) = 0$, which means the heating function at the detection point is zero. The pressure $\hat{p}(z,\omega)$ is thereby calculated according to equation 2.62. The heating function can be then inserted in the EW model given in equation 2.42, resulting in

$$p_\mathrm{EW}(z,t) = \frac{\Gamma}{4\pi c\sigma^2}\frac{\partial}{\partial t}\left(\exp\left(\frac{-c^2t^2}{2\sigma^2}\right)\int_0^{z-ct} dz' \exp\left(\frac{(z-z')^2}{2\sigma^2}\right) h(z' - z_0 - d_\mathrm{f})\right). \tag{2.66}$$

Along with the one-dimensional entrance window model given in equation 2.62 and the effective axial heating function 2.65, equation 2.66 allows to calculate the axial pressure considering a Gaussian lateral distribution of equal width and thus depicting the three-dimensional entrance window model. As long as all other parameters stay constant, equation 2.66 depends linearly on the absolute particle number, which is hidden in the axial heating function, as it is directly proportional to the depth dose curve. Further, the pressure scales with $1/\sigma^2$ on the lateral bunch size.

Figure 2.9 shows axial ionoacoustic signals calculated using the three-dimensional entrance window model according to equation 2.66. The entrance window is considered to be a polyamide foil of $d_\mathrm{f} = 50\mu$m thickness. When compared to the ionoacoustic signals calculated without considering the entrance window (figure 2.7), the entrance window model exhibits three peaks and not only one single-cycle pulse. In addition to the BP signal around $t = 14\mu$s, the entrance window signal and the reflected BP signal appear at $t = 20\mu$s and $t = 26\mu$s, respectively. To demonstrate the influence of the energy spread, figure 2.9a) presents signals for two different energy spreads: $\sigma_\mathrm{E} = 0.5$ MeV and $\sigma_\mathrm{E} = 1.0$ MeV. The energy spread affects the BP and reflected BP signals, as reflected in the first two terms of Equation 2.62. However, the entrance window signal, described by the third term, is independent of the energy spread. The effect of the lateral spread σ on

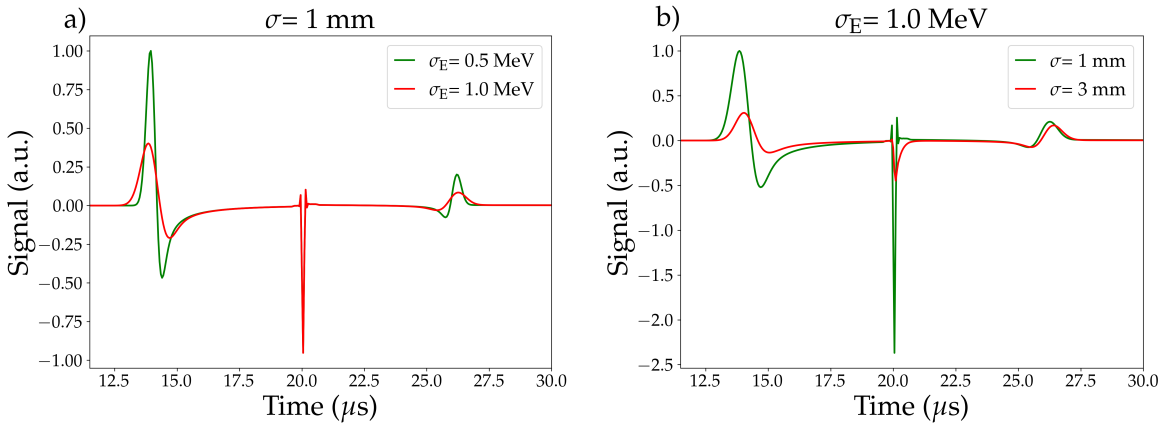

Figure 2.9: Ionoacoustic signals calculated based on the entrance window model for a 30 MeV beam. In a), the influence of the energy spread is exemplarily shown for $\sigma_E = 0.5$ MeV and $\sigma_E = 1.0$ MeV. In b), the lateral spread is varied between $\sigma = 1$ mm and $\sigma = 3$ mm.

the axial ionoacoustic signal is depicted in Figure 2.9b). All three peaks, including the entrance window signal, are influenced by the lateral bunch width. Mathematically, this is expressed in Equation 2.66, which describes the 'smearing out' of an acoustic pulse calculated based on the one-dimensional model due to a laterally extended bunch. A larger bunch width leads to broader peaks in all three signals, which is visible by the comparison between the traces for $\sigma = 1$ mm and $\sigma = 3$ mm. It is worth noting that the signal amplitude is also affected by the bunch width: a larger bunch width results in a decreased signal amplitude for the same number of particles contained in the bunch. To conclude, the ionoacoustic signal amplitude generated at the entrance window location is proportional to the number of protons per unit area, or proton fluence.

2.3.4 Detector response function

The ionoacoustic signal, as modelled in the previous sections, undergoes modifications upon detection. The influence of the detector system on the physical signal is a common challenge across various scientific disciplines and is typically described as the signal transfer function, which quantifies the signal output with respect to the signal input [90]. In this work, the transfer function is referred to as the Total Impulse Response (TIR) equivalent to previous studies in the field of ionoacoustics [26, 27, 91]. Mathematically,

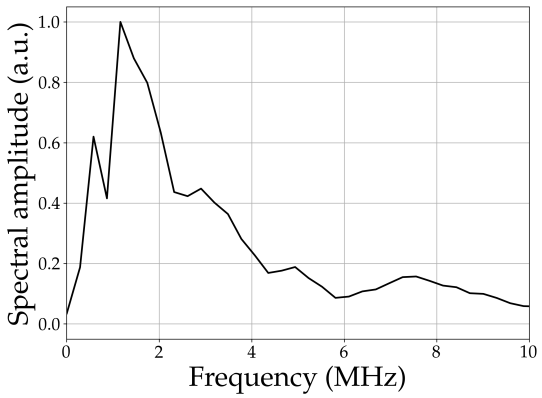

Figure 2.10: Total impulse response of the 10 MHz piezoelectric ceramic transducer with 25.4 mm focal length connected to a voltage amplifier.

the influence of the TIR on the signal input $p(\vec{r}, t)$ is described as a convolution

$$p(\vec{r}, t)_{\text{det}} = p(\vec{r}, t) \otimes \text{TIR}(\vec{r}, t) \tag{2.67}$$

with $p(\vec{r}, t)_{\text{det}}$ representing the detected signal. The TIR includes spatially dependent signal distortions, known as the Spatial Impulse Response (SIR), and the influence of the data acquisition chain, referred to as the Electric Impulse Response (EIR) [91]. Accurate modelling and consideration of the detector response into the bunch parameter reconstruction are challenging, particularly due to the requirement of a broadband and well-characterised input signal for measuring the TIR. More information on the TIR modelling and the signal reconstruction can be found in references [91] and [92].

In this work, a simplified but fast approach is adopted, not differentiating between EIR and SIR but considering the TIR evaluated at a single position. For comparison between the theoretical calculated and experimental signal traces, the TIR is estimated from the entrance window signal, as detailed in section 3.4.1. Further, the TIR is reflected in the commonly observed signal broadening resulting from limited detection bandwidth, which is considered when determining the proton bunch energy spread.

Figure 2.10 displays the absolute value of a TIR at a single position in frequency domain, obtained for a 10 MHz piezoelectric ceramic transducer (Videoscan series, Olympus Deutschland GmbH) with 2.54 cm focal length connected to a commercial low noise amplifier (HVA-10M-60-B, Femto Messtechnik GmbH). A plasma generated by a short laser pulse serves as the calibration source. The experimental set-up and the TIR retrieval algorithm are described in detail in reference [93]. As visible from the graph, the TIR

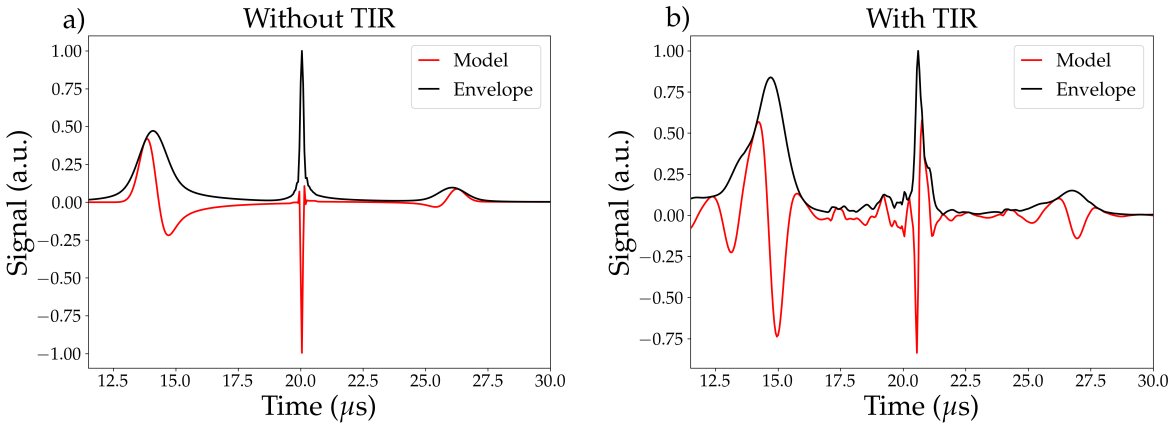

Figure 2.11: Influence of the detector response on an ionoacoustic signal calculated based on the entrance window model for an exemplary proton bunch with $E = 30$ MeV, $\sigma_E = 1.0$ MeV and $\sigma = 1$ mm. The ionoacoustic signal (red) and its envelope (black) is shown in a) without and b) with consideration of the total impulse response.

favours frequencies around the peak at approximately 2 MHz while attenuating very low and high frequencies. Although the specific form of the TIR may vary depending on the choice of transducer and amplifier, the overall shape of the response is typical for many detection systems, with the peak reflecting the stimulation of the resonance frequency of the complete system, which interestingly shows little relation to the transducer qualification '10 MHz'.

Figure 2.11 visualises the influence of the TIR on the incoming ionoacoustic signal. Figure 2.11a) shows an exemplary ionoacoustic signal calculated for a proton bunch with a mean energy of $E = 30$ MeV, an energy spread of $\sigma_E = 1.0$ MeV and a lateral spread of $\sigma = 1$ mm. Figure 2.11b) shows the convolution of this incoming signal with the TIR visualised in figure 2.10, revealing several important influences of the detection system. The signal is clearly distorted. The single-cycle pulse at $t = 14$ μs generated at the BP translates into a complex waveform with several zero crossings. Secondly, the signal experiences is delayed. This delay arises because detection systems are unable to accurately track the steep signal rises associated with high frequencies. By determining the positions of the signal envelope maxima, a time delay of 0.6 μs is found for this example. Thirdly, the acoustic pulses are lengthened. As a measure, the FWHM of the signal envelope is evaluated, revealing a broadening of from 1.4 μs to 1.6 μs and from 0.2 μs to 0.3 μs for the BP and the entrance window signal, respectively. While this theoretical model serves as an example to illustrate the influence of the TIR, it is

important to note that the behaviour will vary depending on the specific transducer and amplifier arrangement in the experiment.

2.3.5 Deduction of the proton bunch energy spread

In this section, the considerations are reconnected to the energy spread of a proton bunch with a Gaussian energy spectrum with the axial ionoacoustic signal. This approach offers a significant reduction in calculation time compared to the previously published iterative reconstruction method for the complete proton bunch energy distribution [59]. For many applications, quantifying the energy spread with a single value is sufficient.
Given that the mean energy of the bunch is known, the energy spread becomes the only free parameter of a Gaussian-distributed energy spectrum. Consequently, it is mathematically possible to deduce the energy spread from the axial ionoacoustic signal by extracting a properly chosen single parameter. In cases where the deposited energy distribution exhibits a single spike, such as the BP of focused protons described by a Gaussian energy distribution, a single-cycle pulse with a central wavelength and a pulse duration proportional to the size of the distribution in the respective direction of observation is expected. As a measure for the pulse width, the FWHM of the signal envelope multiplied by the speed of sound in water is chosen and further referred to as axial signal width w_{ax}. While it may be possible to derive a formula for the signal width based on the theoretical ionoacoustic model in an analytic way, however, such a formula would likely be long and impractical to use.
Here, a simplified model describing the relationship between signal width w_{ax} and the FWHM of the Gaussian energy spectrum $\mathrm{FWHM_E}$ is derived in three steps.
Firstly, the axial signal width is expressed by

$$w_{\mathrm{ax}} = \sqrt{a \cdot w_{\mathrm{BP}}^2 + w_{\mathrm{min}}^2}, \tag{2.68}$$

which results from the convolution of the axial BP width w_{BP} multiplied by a factor a and the shortest possible acoustic pulse w_{min}. The detector response is therein described in a single parameter w_{min} describing a broadening of the signal. The influence of the detection system on the signal phase is already excluded from the model as the model relies on the signal envelope. The factor a accounts for a proportional relationship between BP width and the width of the single-cycle pressure wave and depends on the shape of the exact distribution function.
Secondly, the BP width is related to the spread of the proton bunch range distribution

σ_R by

$$w_\mathrm{BP}^2 = b \cdot \sigma_\mathrm{R}^2 \tag{2.69}$$

with a proportionality factor b. Assuming a linear relationship is not trivial, however, motivation can be found in reference [94].
Thirdly, the relationship between the spread of the proton bunch range distribution and the energy spread is considered according to equation 2.29. Inserting equations 2.29 and 2.69 in equation 2.68 and using the exponential range-energy relationship given in equation 2.26 yields

$$w_\mathrm{ax} = \sqrt{k_\mathrm{ax}^2 \cdot (0.000144\alpha^{1.87}E^{1.87p} + \sigma_\mathrm{E}^2\alpha^2p^2E^{2p-2}) + w_\mathrm{min}^2}. \tag{2.70}$$

Inverting equation 2.70 results in

$$\sigma_\mathrm{E} = \frac{1}{\alpha p E^{p-1}} \sqrt{\frac{w_\mathrm{ax}'^2}{k_\mathrm{ax}^2} - 0.000144\alpha^{1.87}E^{1.87p}} \tag{2.71}$$

with the reduced signal width

$$w_\mathrm{ax}' = \sqrt{w_\mathrm{ax}^2 - w_\mathrm{min}^2}. \tag{2.72}$$

Equation 2.71 provides a formula for the energy spread depending on the unknown constant $k_\mathrm{ax}^2 = a \cdot b$. By calculating the reduced signal width w_ax' with the analytical model of the ionoacoustic signal derived in section 2.3.1 and 2.3.2 for various energy spreads, k_ax can derived as fit parameter. Here, the pressure trace is calculated based on the EW model assuming a Gaussian lateral bunch distribution with $\sigma = 0.5$ mm. It is worthwhile mentioning that the analytical model directly results in w_ax' when not considering a detector response. This comes with the benefit that the here deduced fit parameter is independent of the detection set-up. The detector response, however, can be easily considered by subtracting w_min quadratically from the measured signal width. Another option is to deconvolve the measured signal with the detector response function and subsequently determine w_ax' as the signal width of the deconvolved signal.
Figure 2.12 visualises equation 2.71 for mean energies E between 10 and 40 MeV and energy spreads σ_E ranging from 0.05 to 1.0 MeV. The dimensionless fit parameter k_ax is found to be 3.92 ± 0.01 for all energies. The match of the fit function with the calculated

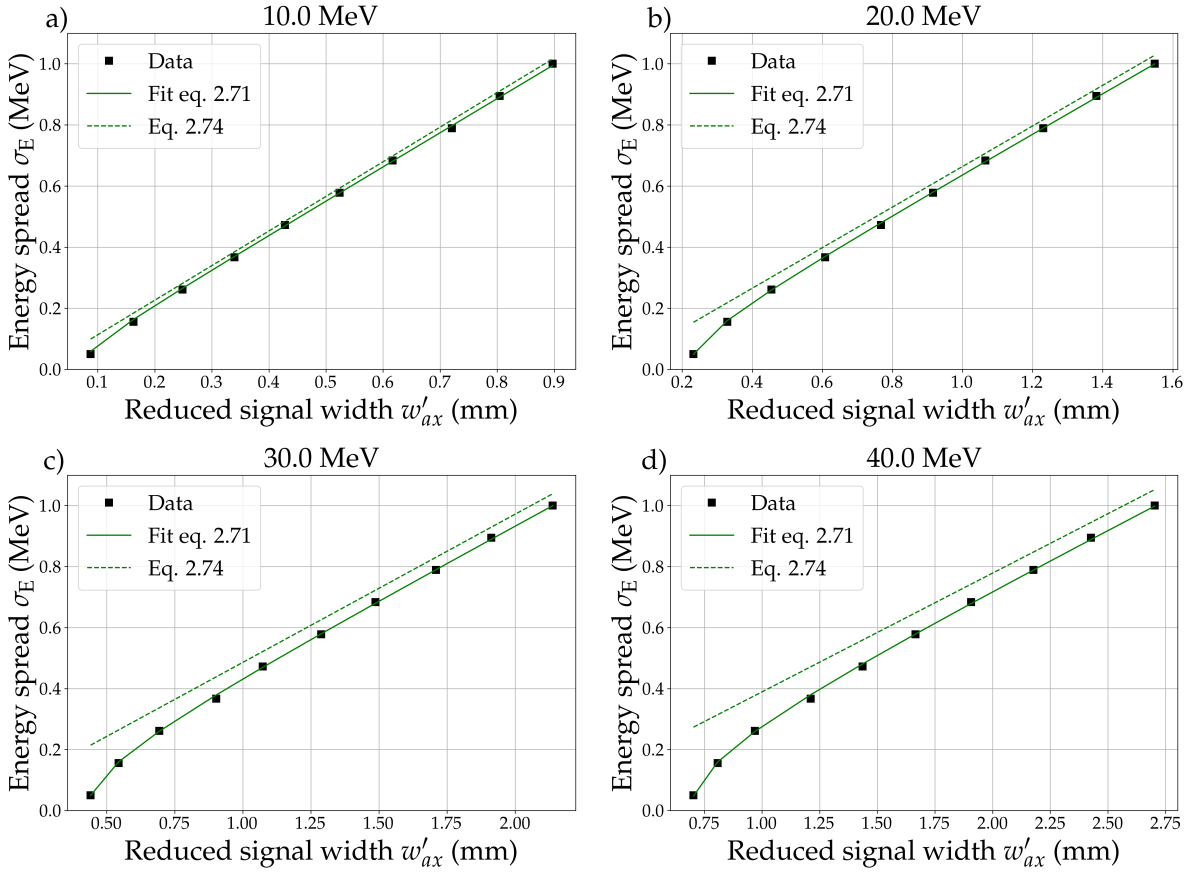

Figure 2.12: The black data dots display the energy spread as function of the determined reduced signal width w'_{ax} for varies mean energies, see title of each plot. The green full line shows a fit according to equation 2.71. Additionally, equation 2.74 is visualised in green dashed lines.

data points and the independence of the fit parameter k_{ax} on the mean energy validates the model derived in this section. More precisely, it proves the parameters a and b to be indeed constant in the considered parameter range. The initial energy spread of a proton bunch can thus be determined by

$$\sigma_{\mathrm{E}} = \frac{1}{0.039 \cdot E^{0.77}} \sqrt{\frac{w'^2_{\mathrm{ax}}}{15.37} - 1.54 \cdot 10^{-9} \cdot E^{3.31}} \tag{2.73}$$

with the mean energy E in MeV and the reduced axial signal width w'^2_{ax} in mm. For large initial energy spreads and small mean energies, range straggling can be neglected and equation 2.73 can be further simplified to

$$\sigma_{\mathrm{E}} = \frac{1}{0.15 \cdot E^{0.77}} w'_{\mathrm{ax}} \tag{2.74}$$

which is visualised in figure 2.12 as well. The deviation between the accurate modelling according to equation 2.71 and the approximation given in equation 2.74 increases towards larger mean energies. This agrees well with the theoretical expectation, as the influence of the range straggling increases towards larger particle ranges and thus energies. To give a numerical example, the Gaussian range spread of a 30 MeV beam with an initial energy spread of 0.5 MeV is 0.029 cm, comprising 0.027 cm attributed to the initial energy spread and 0.011 cm caused by straggling. Therefore, for most cases involving laser-accelerated protons, equation 2.74 serves as a practical and convenient formula for deducing the particle bunch energy spread from a measured acoustic trace.

3 Materials and Methods

3.1 Ionoacoustic detector designs

3.1.1 I-BEAT 3D

The I-BEAT 3D detector shown in figure 3.1 is designed to capture the three-dimensional properties of laser-accelerated protons. The detector consists of an aluminium box with dimensions 16 cm × 14 cm × 10 cm, filled with water. Protons enter the detector through a 50 μm thin polyamide entrance window with a diameter of 17 mm. Compared to the previous I-BEAT detector, which had only one ultrasonic transducer positioned along the proton axis [59], the I-BEAT 3D design incorporates four transducers. One transducer, referred to as the 'axial transducer', is mounted in extension of the proton bunch axis, while the other three 'lateral transducers' are positioned to the right, left, and top of the water volume. The set-up is designed to accommodate piezoelectric ceramic transducers from the Videoscan series by Olympus Deutschland GmbH. The series provides transducers with varying diameters and central frequencies. Each transducer is available with a flat or spherical surface. The spherical surface increases the signal amplitude for acoustic waves generated in the (variable) focal length and are further labelled as focused transducers. In the experiments presented here, the transducer diameter is 1.27 cm (0.5 inch). The transducer central frequency is chosen between 1, 3.5, 7.5 and 10 MHz depending on the experimental purpose and is explicitly stated for each campaign in section 3.3. All four transducers are directed towards the centre of the detector design, positioned at a distance of 2.54 cm, which corresponds to the focal length of the available focused transducers. A set of entrance windows is provided, labelled with energies ranging from 10 to 100 MeV in 10 MeV increments. The labelling indicates the proton energy for which the Bragg peak aligns with the detector centre. For example, the entrance window labelled '20 MeV' is positioned 4.2 mm in front of the detector centre, corresponding to the range of a 20 MeV proton bunch, which is approximately 4.2 mm. The I-BEAT 3D detector is utilised in two experimental campaigns using laser-accelerated protons, as detailed in Sections 3.3.1 and 3.3.2.

Figure 3.1: Photographs of the I-BEAT 3D detector. The left picture shows the detector in beam's eye view; the circular entrance window is visible in the centre. The shielded cables connect the four transducers via the amplifiers to the oscilloscope. In the right picture, the lid is removed, and the detector inside is revealed. The ochre entrance window is visible along with the axial, right and left transducers. The detector is not filled with water for better visibility.

3.1.2 TI-BEAT

The TI-BEAT detector shown in figure 3.2 is a transmissive ion bunch detector that operates on the ionoacoustic principle. TI-BEAT is based on the same aluminium box as the I-BEAT 3D detector introduced in the previous section 3.1.1. While the three lateral transducers are mounted as for the I-BEAT 3D detector, the axial transducer is replaced with a 50 μm thin polyamide exit window. The choice of transducer configuration for the TI-BEAT depends on the anticipated ion bunch parameters, which are specified in Section 3.3.3 for the experiments conducted in this work. In this work, the entrance- and exit windows are designed to support a water column of 1 cm thickness, symmetrically aligned with the detector design centre. Ions with ranges larger than the respective thickness will leave the detector through the exit window. Currently, laser-accelerated protons lack the necessary particle yield at kinetic energies sufficient to effectively penetrate the 1 cm water column. Consequently, the TI-BEAT detector is tested at a synchrotron facility where ion bunches with sufficient energy are available. The complete set-up of this campaign is depicted in Section 3.3.3.

3.2 Signal amplification

The experimental studies conducted in this work utilise two types of amplifiers: a voltage amplifier and a charge amplifier. Its task is the analogue amplification of the

Figure 3.2: Photographs of the TI-BEAT detector. The left picture shows the detector in beam's eye view; the circular entrance window is visible in the centre. The shielded cables connect the three transducers via the amplifiers to the oscilloscope. In the right picture, the lid is removed, and the detector inside is revealed. Opposite the ochre entrance window, the exit window is mounted from which only the aluminium tube serving as holder is visible. Further, the right and left transducers are visible, pointing towards the centre between entrance and exit window. The detector is not filled with water for better visibility.

typically weak piezoelectric signal, which is sensed by the ultrasonic transducer. The key requirements for these amplifiers are a bandwidth tailored to the relevant frequency range and low intrinsic noise. Further, the preservation of the signal shape during amplification is beneficial. In this work, the HVA-10M-60-B (voltage amplifier) and HQA-15M-10T (charge amplifier) models, supplied by FEMTO® Messtechnik GmbH, are employed. Table 3.1 provides an overview of the most important specifications for both amplifiers. The maximum output voltage mentioned in the table applies to the limited range of linear amplification. The upper limit of the voltage amplifier's bandwidth is 10 MHz and can result in a distortion of high-frequency signals, particularly when using a 10 MHz transducer. The specified intrinsic noise of the amplifiers is lower for the charge amplifier. However, for a meaningful assessment of the experimental sensitivity, it is necessary to consider the influence of impedance matching at the amplifier input and the different gains, which are investigated in this chapter.

The working principle of the two amplifier types is inherently different, as evident from the different units of the gain factor. The voltage amplifier directly translates input voltage to output voltage, whereas the charge amplifier is sensitive to input charge and converts it into voltage [96]. Therefore, a dimensionless amplification factor cannot be defined for a charge amplifier, and instead, a charge-to-voltage conversion factor is used

Table 3.1: Specifications of the employed voltage and charge amplifiers [95].

Amplifier	Max. output	Bandwidth (-3 dB)	Noise	Gain
Voltage amplifier HVA-10M-60-B	3.5 V	1 kHz - 10 MHz	0.9 nV/$\sqrt{\text{Hz}}$	60 dB ± 3%
Charge amplifier HQA-15M-10T	5 V	250 kHz - 15 MHz	0.7 nV/$\sqrt{\text{Hz}}$	10 V/pC ± 3%

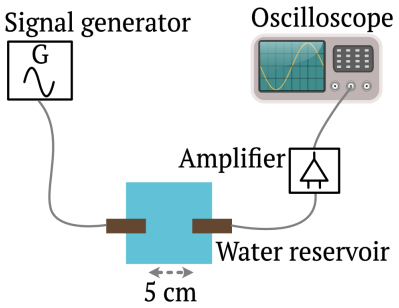

Figure 3.3: a) Experimental set-up to assess the amplifier properties. A test signal is emitted by a transducer connected to a signal generator. Another transducer is positioned to detect the signal, which is amplified by the amplifier under investigation and sent to an oscilloscope. The transducers are shown in brown.

as a gain measure. Further, the amplification properties of both amplifiers depend on the impedance matching at the amplifier entrance. The voltage amplifier has an input impedance of 50 ohms, while the charge amplifier is designed with a high-resistance input of 1 Gohm [95]. Hence, a performance comparison between the two amplifiers relies on the specific set-up, particularly the transducer being used. To assess their performance, an artificially created acoustic test signal is recorded using both the voltage and charge amplifier. Figure 3.3 illustrates the experimental set-up, where the acoustic test signal is emitted in a water tank from a transducer driven by an electric signal generator.

The test signal is subsequently detected by another transducer positioned facing the sending transducer. The detected electric signal is amplified using either the voltage or the charge amplifier and digitised with an oscilloscope (PicoScope™ 5000 Series, Pico Technology). As transducers, two flat 1 MHz transducers (V303-SU) with 50 Ω output impedance are utilised. The entrance resistance of the oscilloscope is set to 50 ohms for both amplifiers. It is worth noting that a higher input resistance may be advantageous for the charge amplifier [95]. The recorded signals for both amplifiers are presented in

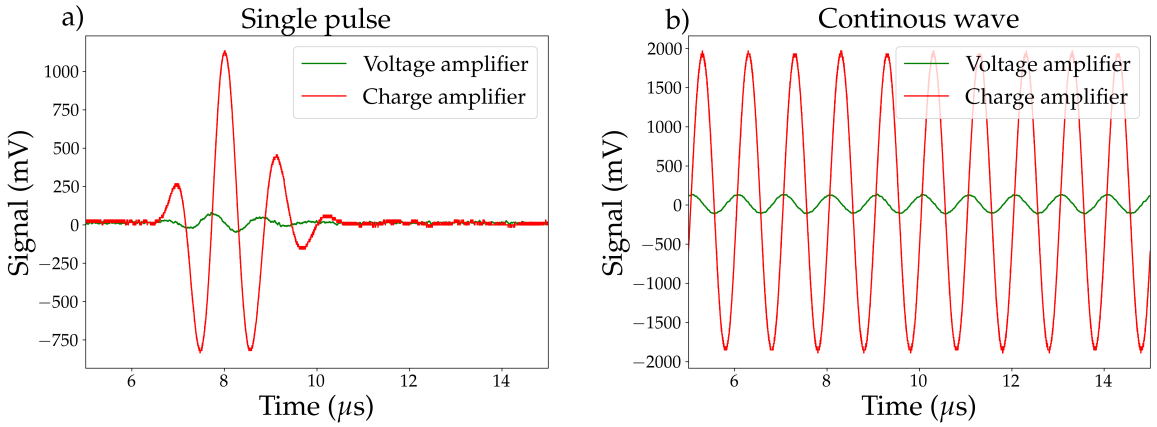

Figure 3.4: a) Single pulse and b) continuous wave signal amplified with both the voltage and the charge amplifier.

figure 3.4. Figure 3.4a) shows the detected signal when the sending transducer is excited by a single sine-shaped electrical spike with a frequency of 1 MHz and an amplitude of 100 mV Peak-to-Peak (PtP). Instead of a single bipolar spike, several oscillations can be observed in the detected signal, even though the sending frequency matches the nominal central frequency of the transducer. This can be attributed to the fact that the electrical spike contains higher-frequency components at the beginning and end, which the transducer cannot accurately track, resulting in an overshoot. It is evident that the charge amplifier provides a much higher signal output compared to the voltage amplifier. With respect to the amplifier noise level being 20 mV PtP for the voltage and 40 mV PtP for the charge amplifier, the Signal-to-Noise Ratio (SNR) is approximately 6 for the voltage and 50 for the charge amplifier, respectively. Hence, the charge amplifier improves the SNR and, thus, detection sensitivity by a factor of approximately 8. It is important to note that the noise level depends on the impedance matching between the transducer and the amplifier and may vary for different transducers. The integrated noise levels specified for the amplifiers could be reproduced without attached transducers.
Figure 3.4b) investigates the amplification of a continuous wave. A phase shift of $\pi/2$ between the two recorded signals can be observed. This phase shift is due to the intrinsic working difference of the amplifiers: the charge amplifier integrates the input current, assuming the current is proportional to the voltage, resulting in an output signal that is the integrated version of the voltage amplifier's signal. For a sine wave input, this translates to a cosine output, equivalent to a phase shift of $\pi/2$. The same phase shift can also be observed in Figure 3.4a) in the single pulse. Therefore, the signal alteration is different for the two amplifier types, which may have implications for the detection

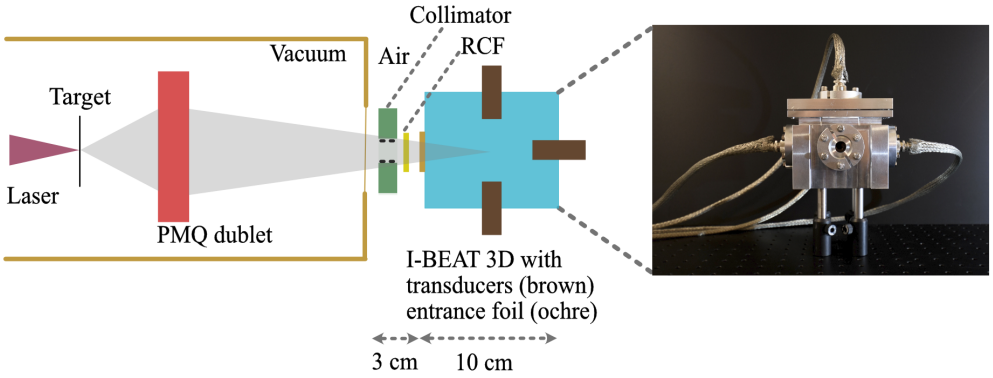

Figure 3.5: Schematic top view of the experimental set-up at the LION beamline (not to scale) with all components relevant for this study; additionally a picture of the I-BEAT 3D detector is shown with the circular entrance window being visible in the centre of the detector. The laser (magenta) is focused onto a thin foil target (black) from which protons are accelerated (grey). A chromatic permanent magnet quadrupole (PMQ) duplet focuses the protons to a spot in air. The protons pass through a collimator with a diameter of 3 mm and an RCF (yellow) before reaching the I-BEAT 3D detector. I-BEAT 3D consists of a water reservoir (turquoise) surrounded by four ultrasonic transducers (brown, three are visible). The ions enter the water through a thin polyamide entrance foil (ochre).

and comparison of ionoacoustic signals. However, it primarily affects the phase of the signal, which is moreover significantly altered by the entire detection set-up (see section 2.3.4), and will not play a role in the analysis method on the basis of signal envelopes in this work (see section 3.4.1).

3.3 Experimental campaigns

3.3.1 I-BEAT 3D at LION

Figure 3.5 shows the experimental set-up implemented at the LION Beamline at CALA. The ATLAS 3000 Laser System is operated to accelerate protons with cut-off energies up to 20 MeV from thin plastic foils [52]. The PMQ doublet focuses protons with design energies between 12 and 16 MeV to a small spot outside the vacuum chamber [73]. By adjusting drift 1 (distance between target and first PMQ) and drift 2 (distance between first and second PMQ), the design energy can be varied for a given target-to-focus distance. The vacuum exit window consists of a 50 μm polyamide foil to which a light-

tight aluminium foil with 12 μm thickness is attached. The proton bunch passes through a collimator with a 3 mm diameter to reduce the influence of particles with energies much lower or higher than the design energy. These spatial-spectral couplings are caused by the focusing properties of a chromatic lens as described in section 2.2. The bunch then passes through a single RCF layer before the particles come to a stop in the I-BEAT 3D detector. As lateral scattering in the polyamide window and the subsequent aluminium foil is not negligible for the considered range of particle energies [73], the detection system is positioned as close to the vacuum window as possible, resulting in a distance of approximately 3 cm between the exit window and the I-BEAT 3D entrance window. For selected shots, the single RCF layer and the I-BEAT 3D detector are removed, and an RCF stack is mounted (not shown in the figure). For the experiments performed at CALA, two I-BEAT 3D configurations are used. They mainly differ in the choice of the axial transducer, with configuration A using a 1 MHz flat transducer and configuration B using a 7.5 MHz focused transducer. The right, left and top position is equipped with 1 MHz flat transducers for both configurations. Additionally, the entrance windows of the two configurations also differ. Configuration A is equipped with a 20 MeV entrance window, while configuration B utilises a 60 MeV entrance window. Each transducer signal is amplified by 60 dB, with configuration A using the HVA-10M-60-B voltage amplifier and configuration B using the HQA-15M-10T charge amplifier. The amplified signal is recorded using a PicoScope™ (6000 Series).

3.3.2 I-BEAT 3D at ALBUS-2S

Figure 3.6 shows the experimental set-up that is implemented at the ALBUS-2S ion irradiation beamline of the DRACO laser at the HZDR [39]. Solenoid S1 is operated to select a narrow energy range around a design energy from the broad spectrum of laser-accelerated protons, which reached up to 54 MeV. The design energy value is varied between 13 and 31 MeV by adjusting the solenoid magnetic field representing the machine parameter defining the design energy. After exiting the vacuum chamber, the bunch travels through an air gap of 6.5 cm length. Then, depending on the experimental configuration, the proton bunch passes through either an aperture equipped with a TOF spectrometer (200 μm thickness) [41, 53, 54] and a parallel plate IC with $4 \cdot 50$ μm polyamide entrance foils (X-Ray Therapy Monitor Chamber 7862, PTW Freiburg) positioned behind the aperture and connected to a dosemeter (UNIDOS, PTW Freiburg) to measure the particle number of the proton bunch or a collimator of variable diameter between 1 and 5 mm. The proton bunch then enters the I-BEAT 3D detector, positioned

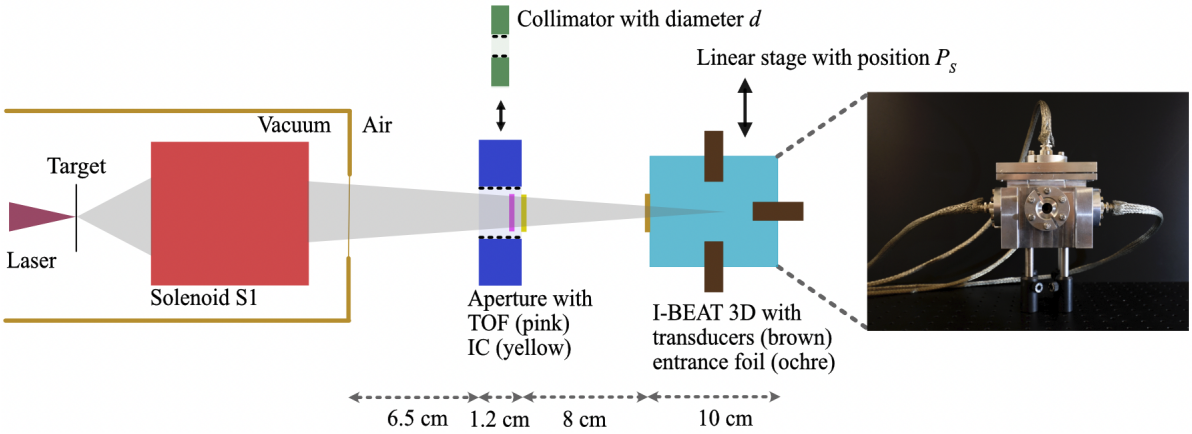

Figure 3.6: Schematic top view of the experimental set-up at the ALBUS-2S beamline (not to scale) with all components relevant for this study. The laser (magenta) is focused onto a thin foil target (black) from which protons are accelerated (grey). One energy-selective solenoid S1 focuses the protons to a spot in air. The protons pass either an aperture equipped with a time-of-flight spectrometer (TOF, pink) and an ionisation chamber (IC, yellow), or a collimator with a variable diameter (green). Finally, the protons reach the I-BEAT 3D detector, which is positioned on a linear stage.

8 cm downstream the aperture or the collimator, respectively. To allow accurate lateral shifts in the horizontal direction relative to the proton axis, the I-BEAT 3D detector is positioned on a motorised stage. For the axial position, a focused 10 MHz transducer is chosen, while flat 1 MHz transducers are installed, in beams eye view, on the right and the left of the water volume, and a focused 3.5 MHz transducer at the top position. Transducers with lower central frequency are installed at the lateral positions in order to account for the difference in the frequency spectrum at the lateral and axial transducer positions. It is expected that the central frequency of the transducer influences the deduction of the lateral bunch width. To investigate this, transducers with two different central frequencies are picked for the right/left and top positions. While the top and the axial transducer are chosen to be focused for optimal signal amplitude, the right and the left transducer are flat to support the scanning of the lateral bunch position. For the study presented here, I-BEAT 3D is aligned such that the BP of 30 MeV protons is in the centre of the four transducers (except when varying the lateral position of the detector relative to the bunch). The signal of each transducer is 60 dB amplified by the HVA-10M-60-B voltage amplifier and then digitised with a PicoScope™(5000 Series). For two shots, the proton bunches were stopped in an RCF stack detector mounted at the position of the I-BEAT 3D detector (not shown in the figure).

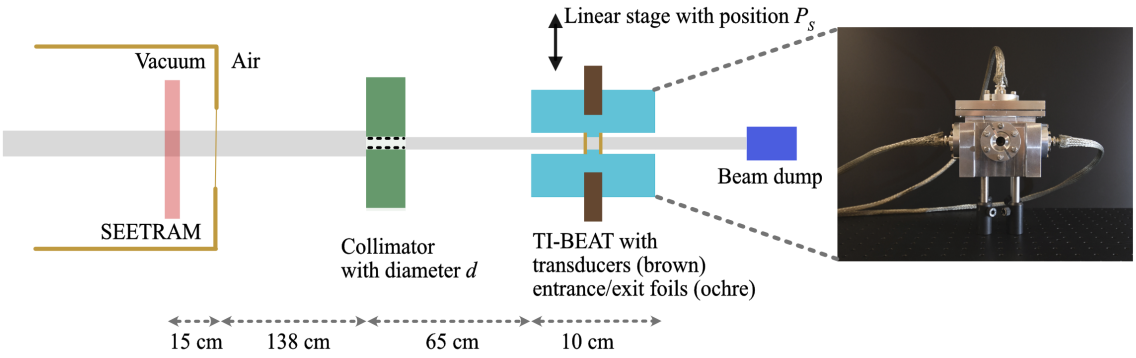

Figure 3.7: Schematic top view of the experimental set-up in cave A of the SIS18 synchrotron (not to scale) with all components relevant for this study. In front of the vacuum exit window, the SEETRAM (red) detects the beam particle number on single-shot basis. After passing a collimator with a variable diameter d (green), the ion beam enters the TI-BEAT detector (turquoise), which is equipped with three ultrasonic transducers (brown, two are visible). Thin polyamide foils (ochre) serve as entrance and exit windows for the ions. Finally, the beam is stopped in a beam dump (blue).

3.3.3 TI-BEAT at SIS18

Figure 3.7 shows the experimental set-up that is implemented in irradiation cave A of the SIS18 synchrotron operated by the GSI. For all experimental configurations, approximately 40 shots are recorded, each consisting of a single $^{124}Xe^{46+}$ ion bunch with kinetic energy of 385 MeV/u. Each ion bunch comprises four micro-bunches, which are merged into a single macro-bunch with a duration of approximately 0.4 μs using fast beam extraction. Located shortly after the synchrotron and approximately 100 m in front of the vacuum exit window, a fast current transformer is positioned (not shown in the figure) to measure the number of the particles in the bunch [97]. This measurement is primarily intended to the needs of the operating team and is not recorded on a single-shot basis but rather provided as a crude estimate to the experimenter. In this work, the measurement result from the fast current transformer is referred to as the nominal bunch particle number. In the experimental cave, a SEcondary-Electron TrAnsmission Monitor (SEETRAM) [98–100] is installed approximately 15 cm in front of the vacuum exit window. The SEETRAM consists of an isolated titanium foil, where

secondary electrons are generated by the passing ion beam. Two additional titanium foils are placed downstream and upstream of the central titanium foil. These foils are at 70 V potential and collect the generated secondary electrons. The created secondary current is guided to an oscilloscope, where it is recorded as a voltage over time. This voltage is related to the current via the input impedance of 50 Ohm. This measurement is saved on single-bunch basis and also serves as trigger for the TI-BEAT detector. At a distance of 138 cm downstream the vacuum exit window, a circular collimator is aligned with the centre of the beam. This serves two purposes: firstly, to restrict the lateral extent of the ion beam, as it is larger than the TI-BEAT entrance window. Without the collimator, dose would be deposited in the aluminium box, leading to signal distortions. Secondly, the ability of TI-BEAT to measure the lateral beam size is assessed by varying the collimator diameter between 1 and 5 mm. The thickness of the collimator in the direction of ion beam travel was varied due to availability reasons between 3 cm and 10 cm and is mentioned in section 4.2 for each data set. After an air gap of 65 cm measured from the collimator front side, the beam reaches the TI-BEAT detector. TI-BEAT is mounted on a linear stage to allow precise variation of the lateral position of the ion beam relative to the detector. All measurements are recorded with the same transducer composition. For the right and left positions, focused 10 MHz transducers are chosen to provide complementary information on the beam properties in this dimension. At the top position, a flat 1 MHz transducer is mounted. The beam is expected to be symmetrical in both lateral dimensions; however, different transducers at the right/left and top positions are used to assess the influence of the transducer response. Similar to the experimental campaign at the ALBUS-2S beamline, the signal from each transducer is amplified by 60 dB using the HVA-10M-60-B voltage amplifier and recorded with the PicoScope™(6000 Series).

3.4 Data analysis

3.4.1 I-BEAT 3D

Figure 3.8 shows an exemplary signal for both the axial and the right lateral transducer recorded with the I-BEAT 3D detector during the experimental campaign at the ALBUS-2S beamline described in section 3.3.2. The red curves show the single-cycle nature of the lowpass filtered pressure pulses, and the black curves show the amplitude envelopes. Since the phase and amplitude of the acoustic signal will be modified on detection as

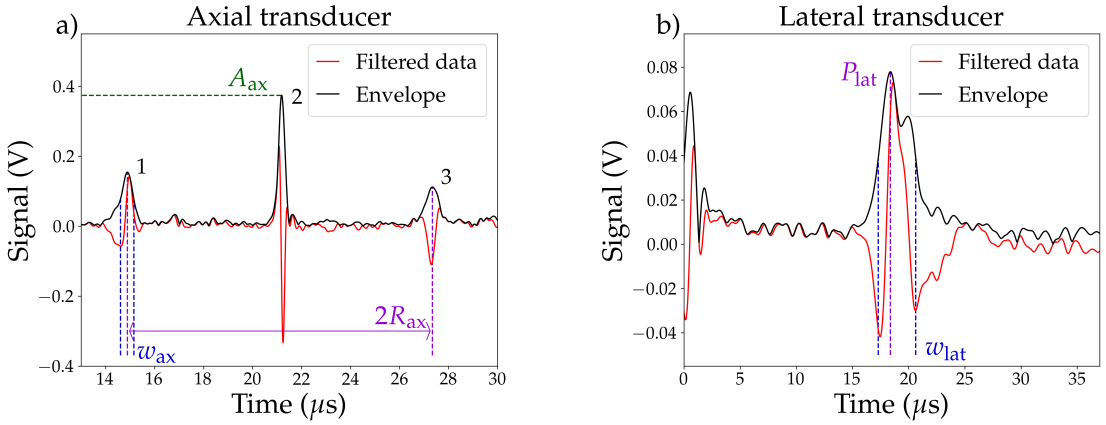

Figure 3.8: Exemplary ionoacoustic signal recorded with the a) axial transducer and b) the right lateral transducer during the campaign at the ALBUS-2S beamline. Curves represent the lowpass filtered data (red) and the signal envelope (black). The read-out positions for the deduction of the bunch properties, as described in the text, are marked by vertical and horizontal dashed lines.

elaborated in section 2.3.4, the analysis is restricted to the signal envelope calculated by taking the absolute value of the signals Hilbert transformation and deducing the amplitudes with their respective positions as well as their FWHM values. The envelopes recorded with the axial transducer are used to deduce the axial proton bunch properties and the bunch particle number; the envelopes from the lateral transducers are employed to measure the lateral bunch properties. All I-BEAT 3D data presented in this study are recorded using individual proton bunches; no averaging is performed. For all transducers, the measured data is filtered with a Butterworth lowpass filter (sixth-order) to reduce noise. The cut-off frequency is matched to the transducer properties aiming at reducing as much noise as possible while not manipulating the ionoacoustic signal. For the data recorded at the LION beamline, the cut off-frequencies of the axial transducers are for configuration A $f_{\mathrm{max,ax}} = 1.5$ MHz (1 MHz axial transducer) and for configuration B $f_{\mathrm{max,ax}} = 4$ MHz (7.5 MHz axial transducer). The cut off-frequencies for the filtering of the lateral transducers are $f_{\mathrm{max,top}} = 1$ MHz (1 MHz top transducer) and $f_{\mathrm{max,lr}} = 1$ MHz (1 MHz right and left transducer). As a low-frequency noise is recorded during the campaign, an additional highpass filter with $f_{\mathrm{min}} = 0.2$ MHz is applied to the data of all transducers. For the experimental data recorded at the ALBUS-2S beamtime $f_{\mathrm{max,ax}} = 4$ MHz (10 MHz axial transducer), $f_{\mathrm{max,top}} = 1.5$ MHz (3.5 MHz top transducer) and $f_{\mathrm{max,lr}} = 1$ MHz (1 MHz right and left transducer) is used.

Axial transducer signal

The axial signal in figure 3.8a) reveals three temporally separated pulses that are typical for proton bunches with narrow energy spread as theoretically modelled in section 2.3. In this work, the first and the third pulse is used to deduce the proton bunch mean energy and to monitor the proton bunch energy spread. The first pulse corresponds to the acoustic wave emitted from the BP directly towards the axial transducer. Likewise, an acoustic pulse is emitted from the BP location in the opposite direction towards the entrance foil, where it is reflected and propagates towards the axial transducer, leading to the third peak. The arrival time difference between both pulse envelope maxima, marked by the vertical magenta lines, corresponds to twice the proton bunch range R_{ax} divided by the speed of sound. Using the exponential range-energy relationship given in equation 2.26, the mean energy E of the particle bunch before entering the detector can be deduced [20].The axial signal width w_{ax} is modelled according to

$$w_{\mathrm{ax}} = \sqrt{\tilde{k}_{\mathrm{ax}} \cdot E^{2p} + w_{\mathrm{min}}^2}. \tag{3.1}$$

This formula is a simplification of equation 2.70, neglecting the straggling of the protons in water as the energy spreads considered in this work dominate the BP width. Further, the energy spread of the proton bunch focused by a chromatic lens σ_{E} is modelled first-order proportional to the mean energy, $\sigma_{\mathrm{E}} \propto E$. A fit of the measured values for w_{ax} according to equation 3.1 allows to determine the minimal axial signal width w_{min}. The proton bunch energy spread σ_{E} is calculated according to equation 2.74 from the signal width.
The third pulse that appears in the centre of the signal trace is generated at the location of the entrance foil. This signal, in particular the amplitude of its envelope A_{ax}, is expected to depend on the proton fluence and thus contains information on the particle number of the proton bunch as evolved in section 2.3.3. This is also true for the first pulse. However, the amplitude of the first pulse also depends on the energy spread, which makes reconstruction more difficult and less robust. If the detection geometry and the spatial distribution remain constant from bunch to bunch, A_{ax} is proposed as a measure for the number of protons contained in a single bunch.

Lateral transducer signal Figure 3.8b) shows a typical lateral signal recorded with the right transducer. At t=0 μs, the measurement shows the decaying EMP contribution generated during laser-plasma interaction; at around 20 μs and thus well separated

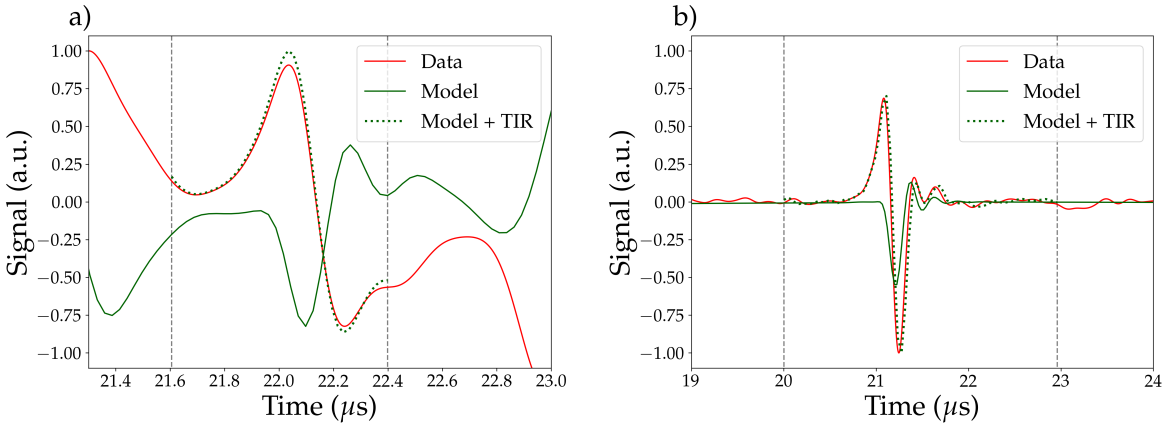

Figure 3.9: Modelling of the detector response using the axial entrance window signal for the experimental set-up used at the a) LION beamline and b) ALBUS-2S beamline. The experimental data is shown in red, and the theoretical model in green. The green dotted line shows the theoretical model convolved with the estimated TIR. The grey dashed line marks the interval in which the TIR is determined.

from the EMP contribution, the acoustic pulse due to the transverse energy density distribution is visible. The lateral bunch position and size can be deduced from this pulse envelope through the maximum position and the FWHM. The left transducer contributes complementary information, and in combination, right and left transducers allow a cross-check of the extracted parameters for horizontal bunch position and size. The top transducer signal is analysed in the same way and provides information in the vertical dimension. Finally, the lateral bunch position is defined by the time of the envelope maximum (magenta vertical line) multiplied by the speed of sound in water. The FWHM of the lateral ionoacoustic signal envelope w_{lat} (blue vertical lines) is related to the bunch diameter in the water, which is connected to the collimator size d. As a model for the lateral signal width,

$$w_{\text{lat}} = \sqrt{k_{\text{lat}} \cdot d^2 + w_0^2} \tag{3.2}$$

is proposed by virtue of a convolution of the collimator size d and the shortest possible acoustic pulse with length w_0 determined by the minimal measurable wavelength plus a potential contribution from lateral broadening during propagation from the collimator to the water and lateral straggling. Again, the constant k_{lat} accounts for the proportionality of the lateral width of the proton bunch to the width of the pressure pulse.

Modelling of the detector response For accurate comparison between the theoretical model and experimental data, the TIR must be taken into account. For that, the TIR is estimated by comparing the modelled and experimental entrance window signals. The entrance window signal is particularly well-suited for this purpose, as it is expected to exhibit broadband characteristics in the frequency domain due to its confined spatial origin. In the first step, the bunch parameters energy, energy spread and lateral spread are estimated from the axial signal measurements, as detailed in the preceding sections. Using these bunch parameters, the analytical model is applied in the second step to calculate a theoretical signal using equations 2.42 and 2.62. Moving on to the third step, the region corresponding to the entrance window signal is defined. Figure 3.9 shows the outcome of this procedure, displaying both the measured (red) and theoretically modelled (green) entrance window signals for a representative shot during the LION beamline (a) and ALBUS-2S beamline (b) campaigns. The design energies of the selected shots are 12 MeV in a) and 30 MeV in b). The interval encompassing the entrance window signal is indicated by the grey dashed line. Defining this interval is relatively straightforward when the entrance window signal is well-separated from the direct and reflected Bragg Peak (BP) signals, as observed in (b). However, in cases with smaller mean energies, an overlap between the entrance window signal and the direct/reflected BP signals may occur, as depicted in (a), posing a more challenging definition. In the forth step, the TIR is determined by a Laplace deconvolution of the measured and theoretically modelled entrance window signal. For validation purposes, the theoretical model is convolved with the TIR, resulting in the green dotted curve visible in figure 3.9. The convolution of the theoretical model with the TIR matches well with the experimental data; any minor deviations can be attributed to the limitations of the numerical sampling rate. The TIR estimated with this procedure is representative for a specific transducer and amplifier set-up and thus must only be determined once for the campaigns at the LION and ALBUS-2S beamline.

3.4.2 TI-BEAT

Figure 3.10 shows an exemplary signal recorded with the right lateral transducer of the TI-BEAT detector during the experimental campaign at the SIS18 synchrotron described in section 3.3.3. The red curves show the lowpass filtered pressure pulses and the black curves show the amplitude envelopes. As for the I-BEAT 3D signal, the analysis is restricted to the signal envelopes and the corresponding amplitudes with their respective positions as well as their FWHM values. Even though several shots are

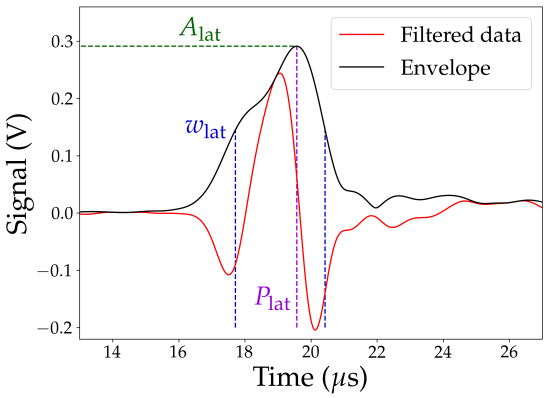

Figure 3.10: Exemplary ionoacoustic signal recorded with the top lateral transducer during the campaign at the SIS18 synchrotron. The red curve represents the lowpass filtered data, and the black curve the signal envelope. The read-out positions for the deduction of the bunch properties, as described in the text, are marked by vertical and horizontal dashed lines.

recorded for each experimental configuration, the data analysis is performed for each shot individually. Averaging is only performed on the extracted bunch parameters and is stated explicitly along with the results. For all transducers, the measured data is filtered with a Butterworth lowpass filter (sixth-order) with cut-off frequencies of $f_{\mathrm{max,lr}} = 4$ MHz (10 MHz transducers) and $f_{\mathrm{max,top}} = 1$ MHz (1 MHz transducer). The lateral bunch position and size are deduced from the pulse envelope through the maximum position, and the FWHM multiplied by the speed of sound labelled P_{lat} (magenta vertical lines) and w_{lat} (blue vertical lines), respectively. As for this detector design no entrance window signal is available, the bunch particle number is assessed using the lateral signal. This signal is proportional to the proton fluence and the deposited energy per particle. Thus, keeping the particle's energy spectrum and lateral distribution constant, it is a complementary measure for the bunch particle number.

3.4.3 Time-of-flight spectroscopy

The proton spectrum retrieved from the TOF measurement using the iterative reconstruction algorithm according to reference [54] is provided by the HZDR. The spectrum describes the proton bunch energy distribution at the position of the scintillator. It takes into account the effects of the vacuum exit window and the air gap between the vacuum exit window and the scintillator. An example of a single proton bunch energy spectrum is shown in Figure 3.11a). For the purpose of this work, the mean energy is deduced by

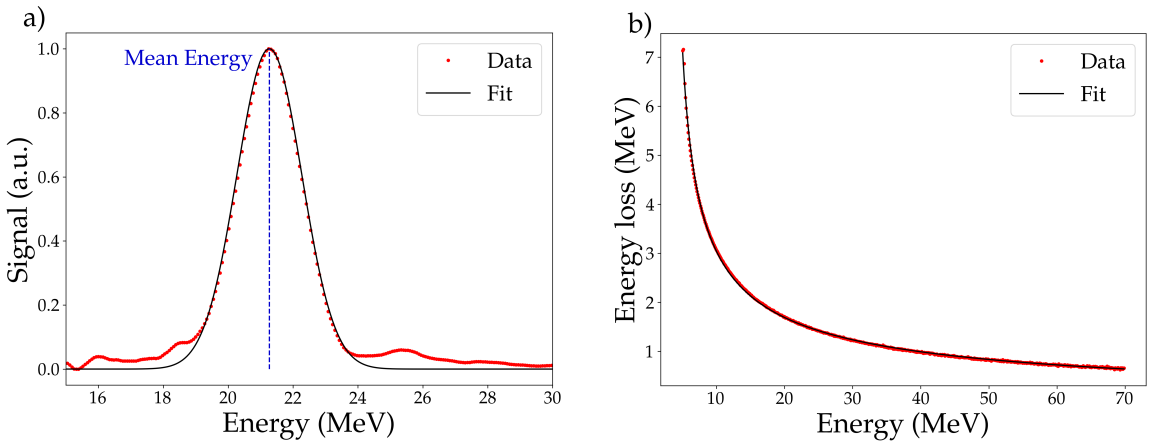

Figure 3.11: a) Proton bunch spectrum reconstructed from the time-of-flight (TOF) measurement. Additionally to the data dots in black, a Gaussian fit is shown in red along with the read-out position of the mean energy marked as blue dashed line. b) Energy loss between TOF and I-BEAT 3D detector. The red data dots are deduced from Monte Carlo simulations accounting for the TOF scintillator, the ionisation chamber, the air gap and the I-BEAT 3D entrance window. A fit of the data is shown in black.

fitting a single Gaussian function to the data and retrieving the mean value. For a proper comparison with the I-BEAT 3D result, the mean energy is then corrected for energy losses in the scintillator, the IC, the air gap between the scintillator and the I-BEAT 3D detector, and the I-BEAT 3D entrance window. The energy loss in each component is estimated from Monte Carlo simulations conducted at HZDR. The total energy loss is displayed in figure 3.11 b) along with a fit

$$E_{\text{loss}} = A \left(\frac{1}{E + c} \right)^{k}. \tag{3.3}$$

where A, c and k are fit parameters and E is the energy in MeV. This function approximates the Bethe formula and provides a continuous description of the energy loss. By subtracting the respective energy loss from the TOF mean energy, a corrected TOF result is obtained for comparison with the I-BEAT 3D mean energy.

3.4.4 Radiochromic films

The RCFs employed in this work are Gafchromic™ EBT3 films provided by the company Ashland Inc [100]. In order to obtain accurate results on the absolute dose distribution, the films need to be calibrated to convert optical density into dose. For the data recorded

at the ALBUS-2S beamline, the calibration is carried out by the HZDR, which provides the two-dimensional dose distribution for each film. On the other hand, for the films irradiated at the LION beamline, the calibration is conducted as part of this work and is described in more detail in reference [101]. In both cases, the films irradiated at the LION and ALBUS-2S beamline, the depth dose curve is deduced from the dose deposited in an RCF stack measurement. Reference [102] provides further information on the RCF evaluation at LION. Once the depth dose curve is obtained, it is used to derive the particle number, mean energy, and energy spread of the particle bunch.

Calibration The calibration is performed by delivering well-defined doses between $D = 0.5$ and $D = 10$ Gy to films with a dimension of 3×3 cm^2 using X-rays from a medical linear accelerator at LMU Klinikum, Munich. 24 hours after irradiation, the films are scanned by the EPSON Expression 11000 XL Pro, and the red pixel value R_i is obtained for each pixel. While in principle other colour channels can be used aswell, the red pixel value provides the most accurate result in the considered dose range [100, 103, 104]. As a single representative value for the film, the averaged red pixel value R calculates

$$R = \sum_i \frac{R_i}{\#pixels}. \tag{3.4}$$

It is related to the optical density OD by

$$\mathrm{OD} = -\log_{10}(R). \tag{3.5}$$

The determined optical density of the irradiated film (irr) must be corrected for a background value (bg). To account for background fluctuations of the scanner, the background value is determined individually for each film using a non-irradiated area of the film. The background corrected net optical density netOD is determined by

$$\mathrm{netOD} = \mathrm{OD}_{\mathrm{irr}} - \mathrm{OD}_{\mathrm{bg}} = \log_{10}\left(\frac{R_{\mathrm{bg}}}{R_{\mathrm{irr}}}\right). \tag{3.6}$$

where the subscripts irr and bg refer to the irradiated film and the background reference, respectively. By fitting the known dose D according to the polynomial relationship

$$D = a \cdot \mathrm{netOD} + b \cdot \mathrm{netOD}^c, \tag{3.7}$$

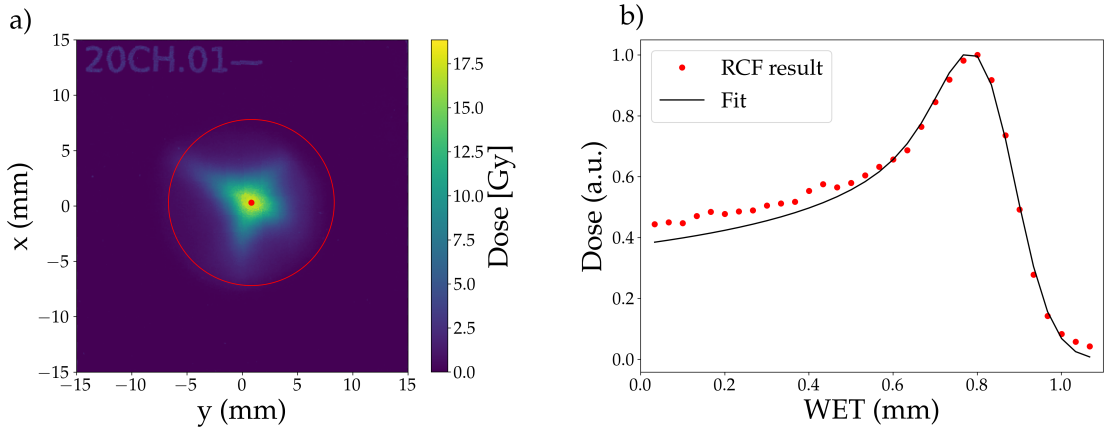

Figure 3.12: a) Single RCF layer with the deposited dose as colour code. The red dot marks the position of maximum dose deposition and the red circle the area of lateral integration with 15 mm diameter. b) Normalised depth dose curve deduced from an RCF-stack measurement. Each data dot in red represents one film layer and is calculated by laterally integrating the deposited dose in an area of 15 mm around the maximum position. In black, a fit according to equation 2.28 is shown.

the calibration factors $a = 5.27 \pm 0.16$, $b = 43.2 \pm 2.0$ and $c = 2.71 \pm 0.06$ are determined for the film batch employed in this work. The uncertainty of each fit parameter translates into the uncertainty of the dose value by Gaussian error propagation. With this calibration, the films irradiated during the experimental campaign at CALA provide the two-dimensional distribution of the dose deposited in each film. The irradiated films are treated in the same way as the calibration films, with the scanning performed 24-48 hours after irradiation using the same scanner and scan parameters.

Depth dose curve The two-dimensional dose distribution obtained from the RCF films is laterally integrated within a Region Of Onterest (ROI) to obtain a single value representing the deposited dose in the film. The ROI is circular and centred around the position of maximum dose deposition. The diameter is chosen as small as possible to reduce the influence of potential noise from non-irradiated regions of the film but large enough to ensure that the entire deposited dose is considered. For the films irradiated at the HZDR, a diameter of 15 mm is a good tradeoff between these constraints. In the experimental campaign conducted at the LION beamline, a collimator with a 3 mm diameter is used for all recorded data, so the diameter of the ROI is chosen to be 6 mm to provide a safety margin compared to the collimator size.
Figure 3.12a) shows an exemplary RCF shot from the HZDR campaign, where the image

value represents the locally deposited dose. The position of maximum dose deposition and the ROI are marked in red. In figure 3.12b), a depth dose curve obtained from an RCF stack measurement is shown in red. For this curve, the laterally integrated dose representing each RCF film is associated with the longitudinal position of the film layer, expressed in units of Water Equivalent Thickness (WET). The WET is the thickness of water that would cause the proton bunch to lose the same amount of energy as the bunch would lose in the RCF medium [105]. Neglecting the influence of different stopping powers in films and in water, the WET is approximated by

$$\mathrm{WET}_{\mathrm{RFC}} = P_{\mathrm{RFC}} \frac{\rho_{\mathrm{RFC}}}{\rho_{\mathrm{w}}}. \tag{3.8}$$

Thereby, P_{RFC} is the position of the film relative to the position of the first layer and ρ_{RFC} and ρ_{w} are the mass densities of the film and water, respectively.

Deduction of the particle bunch properties The deposited dose of particles stopping in an RCF stack is directly proportional to the bunch particle number calculating

$$N = \frac{\rho_{\mathrm{RCF}} \cdot D_{\mathrm{total}} \cdot V}{E_0} \tag{3.9}$$

with D_{total} being the axially and laterally integrated dose, V the integration volume and E_0 the energy of the particles. As only bunches with a narrow energy spectrum are employed in this work, E_0 is considered as the particle's mean energy neglecting the influence of the energy spread. The black curve in figure 3.12b) shows a fit of the depth dose curve according to equation 2.28. From this fit, the range R and the spread of the Gaussian range distribution σ_{R} is deduced as only free parameters. These parameters describe rather the BP than the entrance region of the Bragg curve, as only Gaussian energy distributions are assumed, neglecting the influence of a low-energy tail. Therefore, the fit function is optimised starting from $\mathrm{WET}_{\mathrm{RFC}} = 0.4 \approx R - 10\sigma_{\mathrm{R}}$. The mean energy E and the energy spread σ_{E} is then calculated using equations 2.26 and 2.29.

3.4.5 Secondary-electron transmission monitor

Figure 3.13 presents an exemplary signal recorded with the SEETRAM detector. The left ordinate axis shows the voltage measured with the oscilloscope, which is directly related to the current through Ohm's law. The time dependence of the signal reflects

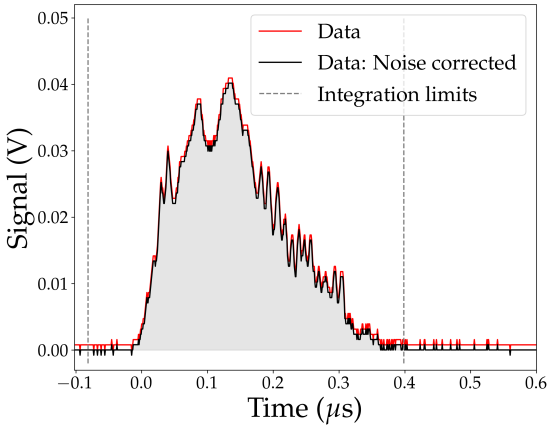

Figure 3.13: Exemplary signal recorded with the SEETRAM detector (red) along with the noise corrected data (black). The integration limits are shown as grey lines, and the resulting integral is marked as grey area.

the extraction profile, representing the bunch intensity over the extraction time. The raw data is shown in red, while the black line represents the background-corrected signal trace. To obtain the background-corrected trace, the average signal value is calculated in the time interval between 140 μs and 180 μs after the bunch, serving as a noise reference. The noise reference is then subtracted from the measured data to obtain the background-corrected trace. The SEETRAM detector triggers based on its own signal, which defines the t=0 μs position, serving as the reference time for the TI-BEAT detector as well. The integral of the background-corrected current represents a measure of the charge and is directly related to the number of secondary electrons collected at the outer titanium foils. Therefore, it is chosen as a measure for the bunch particle number, assuming that all other beam parameters, such as ion species and energy spectrum, remain constant. The integration limits for the background-corrected current are -0.08 μs and 0.4 μs, close to the extraction window, to minimise sensitivity to signal disturbances at earlier or later times. Each signal trace is recorded for a single ion bunch without averaging.

4 Results

4.1 I-BEAT 3D

4.1.1 Axial bunch properties

Figure 4.1 shows the proton bunch mean energy E and the range R_{ax} deduced from the axial I-BEAT 3D signal measured at the a) LION and b) ALBUS-2S beamline for different settings of the respective beamline instrumentation defining the design energy. The data recorded at the LION beamline is acquired with I-BEAT 3D configuration A. At some settings, several bunches were recorded. While this is visible in a) for design energies of 13 MeV and 15 MeV, also for 14 (17) MeV, two (five) shots were acquired at the LION beamline, yielding very similar results in terms of mean energy and are thus hardly distinguishable in the figure. Similarly, two (three) shots are conducted at 20 (30) MeV at the ALBUS-2S beamline. In figure 4.1b), the TOF result is additionally shown in blue. For direct comparison between TOF and I-BEAT 3D, one must account for energy loss in material between both detectors. For that, the IC, the air gap between TOF and I-BEAT 3D and the I-BEAT 3D entrance window is considered in the reconstruction of the TOF mean energy. TOF, IC and I-BEAT 3D results are available on same shot level since TOF and IC are both transmissive diagnostics. The design energy is rather a label to a certain beamline setting derived from a theoretical calculation and does not necessarily refer to a particle bunch property. Therefore, no uncertainty bar is shown in this dimension. The mean energy determined using the I-BEAT 3D detector has an uncertainty defined by the position of the envelope maxima given by half the minimal resolvable wavelength $\lambda_{\mathrm{min}}/2$ with $\lambda_{\mathrm{min}} = c_{\mathrm{s}}/f_{\mathrm{max,ax}}$. The energy uncertainty is then $\Delta E = \mathrm{d}E/\mathrm{d}R \cdot \lambda_{\mathrm{min}}/2$. The uncertainty of the TOF measurement is determined in the reconstruction process accounting for the complete detector response. The corrected TOF and I-BEAT 3D mean energy match within the uncertainties, and absolute deviations remain below 0.8 MeV. Figure 4.2a) shows the I-BEAT 3D signal width w_{ax} for the same shots as in 4.1b) and the fit according to equation 2.68. The data points are displayed as a function of the estimated mean bunch energy. The uncertainty for the axial signal width is calculated using Gaussian error propagation, again assuming that $\lambda_{\mathrm{min}}/2 = c_{\mathrm{s}}/(2 \cdot f_{\mathrm{max,ax}})$ is the

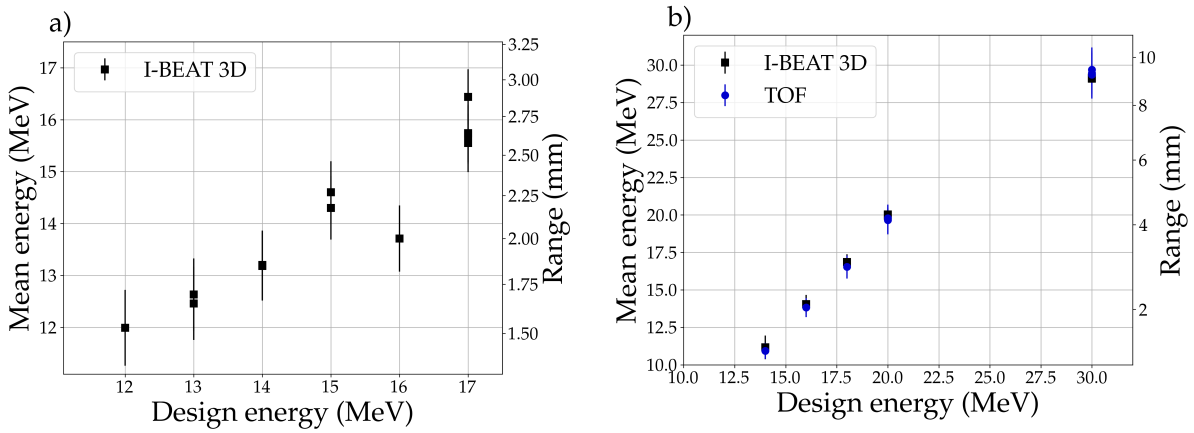

Figure 4.1: Estimated mean energy and range as a function of the design energy, which is a label for a certain beamline setting (see main text). The data shown in a) is recorded at the LION beamline and in b) at the ALBUS-2S beamline. Additional to the I-BEAT 3D result (black), the outcome of the TOF spectrometer (blue) is shown in b).

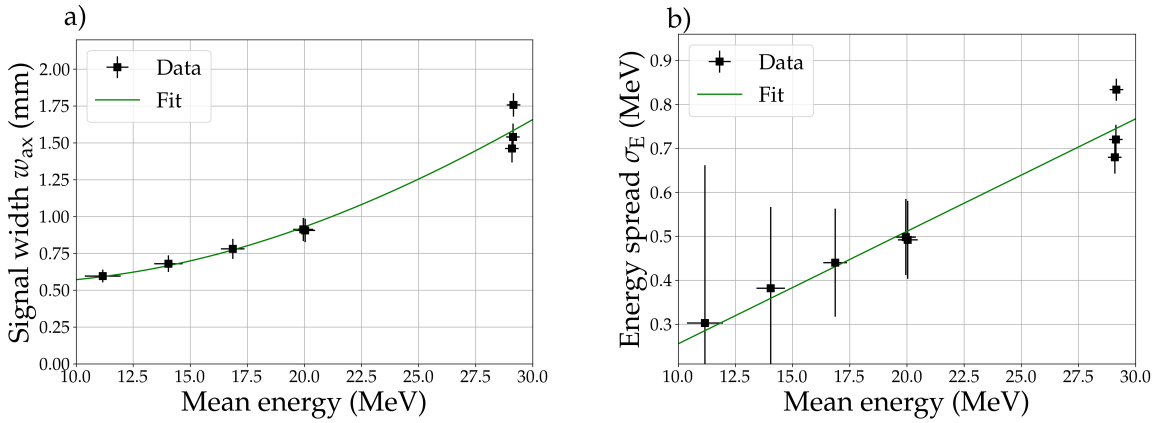

Figure 4.2: a) I-BEAT 3D signal width as a function of the determined I-BEAT 3D mean energy. A fit of the I-BEAT 3D data dots according to equation 2.68 is shown in green. b) Energy spread deduced from the signal width. A linear fit is shown in green.

dominating uncertainty. With increasing energy, the I-BEAT 3D signal width rises with the expected parabolic behaviour. The fit parameter $\tilde{k}_{\mathrm{ax}}$ is $(1.5 \pm 0.1) \cdot 10^{-5}\mathrm{mm}^2\mathrm{MeV}^{-2p}$. The minimal measurable signal width $w_{\mathrm{min}} = 0.53 \pm 0.07$ mm is slightly larger than the minimal resolvable wavelength $\lambda_{\mathrm{min}} = 0.38$ mm. The energy spread σ_{E} deduced from the axial signal widths according to equation 2.74 is shown in figure 4.2b) along with a linear fit. By Gaussian error propagation, the uncertainty of the energy spread is calculated based on the uncertainty of the axial signal width and the mean energy. The linear increase of the energy spread with the mean energy confirms the expected proportionality $\sigma_{\mathrm{E}} \propto E$ [73]. As a proportionality factor, 2.5% is found, which is a measure for the chromaticity of the solenoids. This result can be compared to the energy spectrum deduced from two separate RCF stack measurements for which $\sigma_{\mathrm{E}} = 1.5 \pm 0.1$ MeV and $\sigma_{\mathrm{E}} = 0.70 \pm 0.1$ MeV is determined for mean energies of $E = 29.0 \pm 0.1$ MeV and $E = 28.6 \pm 0.1$ MeV, respectively. The uncertainties are determined by the fit, underestimating the influence of limited axial resolution defined by the film thickness. The significant difference between both shots visualises the possible substantial fluctuations of laser-proton acceleration which question the comparison of measured energy spreads across individual shots. However, the RCF result and the I-BEAT 3D result on the mean energy are very similar, even though shot-to-shot variations are larger than the individual uncertainty, too.

4.1.2 Lateral bunch properties

Figure 4.3 shows the lateral bunch position estimated from the I-BEAT 3D signal. This data is recorded at the ALBUS-2S beamline. The spatial resolution limit calculated by $\pm\lambda_{\mathrm{min}}/2/\mathrm{SNR}$ is represented by the red lines around the expected curve for which the I-BEAT 3D bunch position P_{lat} is equal to the nominal bunch position defined by the stage position P_{S}. The theoretical resolution limit describes the ability to distinguish two signals accounting for the limited detector bandwidth. Deviations between I-BEAT 3D bunch position and nominal bunch position are below 0.4 mm. This data set is recorded with the 3 mm collimator in front of the I-BEAT 3D detector. The uncertainty of the I-BEAT 3D bunch position is given by $\lambda_{\mathrm{min}}/2$, which is much larger than the uncertainty of the proton bunch position in the detector and is chosen more conservatively than the theoretical resolution limit. To have a hint on the reproducibility of the measurement, for some positions several shots were collected. The two consecutive shots at 3 mm and three shots taken at -0.75 mm reveal that shot-to-shot fluctuations cause differences that are smaller than this uncertainty. Accounting for the error bars and the resolution limit,

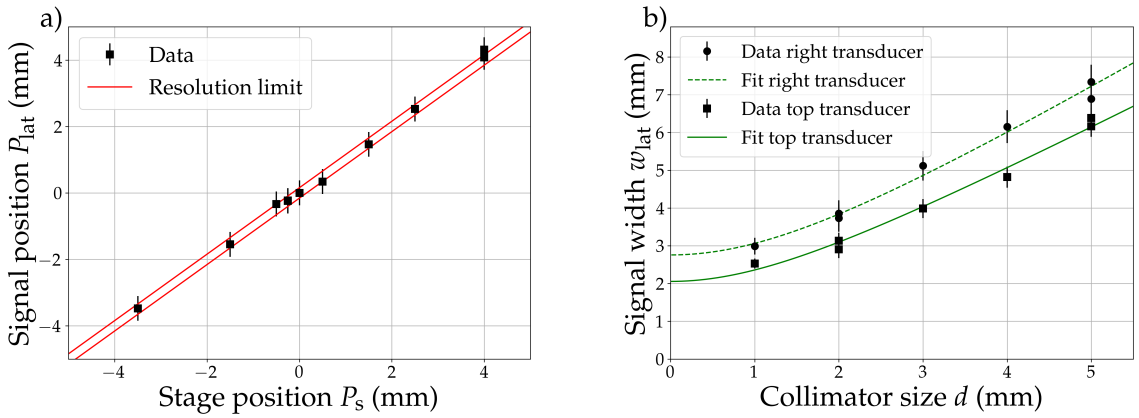

Figure 4.3: a) I-BEAT 3D result of the bunch position in dependence of the stage position. The resolution limit is shown in red. b) Measured lateral signal width in dependence of the collimator size along with a fit according to equation 3.2 for the top and the right transducer. The minimal measurable pulse width w_0 is found to be 2.8 ± 0.2 mm for the right and 2.1 ± 0.2 mm for the top transducer.

the estimated and the nominal bunch position coincide.

Figure 4.3b) shows the width of the ionoacoustic signal w_{lat} measured with the right and top transducer as a function of the collimator size d, also recorded at the ALBUS-2S beamline. A fit of the data according to equation 3.2 is shown in green with a dashed and full line, respectively. Shots were taken twice for the 2 and 5 mm collimator and yielded similar results with deviations below 0.5 mm. The uncertainties of w_{lat} are calculated based on equation 3.2 using Gaussian error propagation, again with $\lambda_{min}/2$ as dominating uncertainty. A clear trend towards a larger signal width with increasing collimator size is visible. According to equation 3.2, for very small collimator sizes the signal width is given by w_0 which is found to be 2.8 ± 0.2 mm for the right and 2.1 ± 0.2 mm for the top signal. Thus it is considerably larger than the minimal resolvable wavelength $\lambda_{min} = 1.5$ mm and 1 mm, respectively. For k_{lat}, $= 1.8 \pm 0.1$ and 1.4 ± 0.1 is deduced for the right and top signal, respectively.

4.1.3 Bunch particle number

Figure 4.4a) shows the amplitude of the window signal envelope A_{ax} as a function of the laterally integrated dose deposited in a single RCF. This data is recorded at the LION beamline with I-BEAT 3D configuration B. The RCF is transmissive to the protons as they are only slowed down but not stopped in the single film. Therefore, the RCF

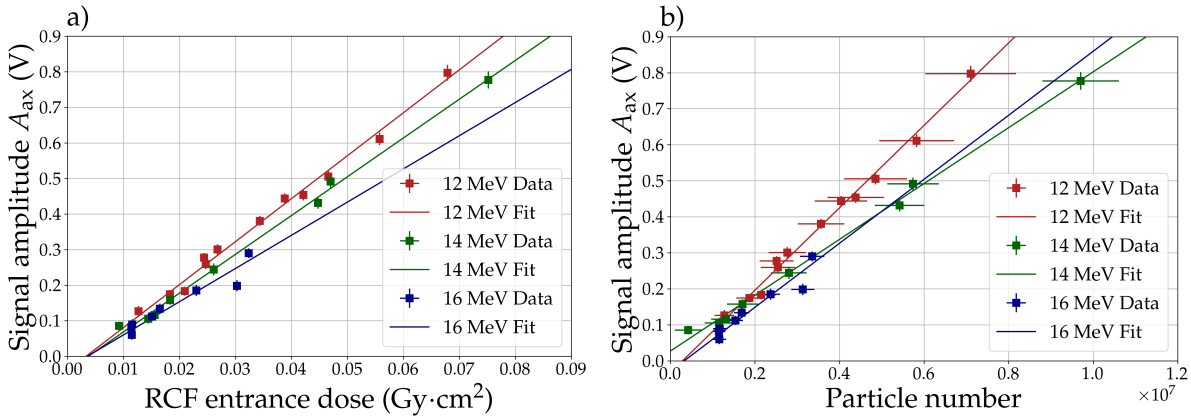

Figure 4.4: The amplitude of the ionoacoustic signal envelope generated in the I-BEAT 3D entrance window is displayed in dependence of a) the laterally integrated dose deposited in the RCF layer and b) the total bunch particle number for design energies 12, 14 and 16 MeV. Each data dot represents an individual particle bunch; additionally, a linear fit is shown for each design energy.

and I-BEAT 3D results are available on same shot level, and each data dot represents a single particle bunch. The uncertainty of the I-BEAT 3D signal is determined by the noise level in the recorded signal. For the RCF result, the uncertainty is calculated using Gaussian error propagation based on the uncertainty of the calibration parameters given in section 3.4.4. Multiple particle bunches are recorded for different design energies of 12, 14 and 16 MeV, and the variation is due to inherent shot-to-shot fluctuations of the laser-driven source. A linear fit is shown for each data set, as a linear relationship between the laterally integrated RCF entrance dose and I-BEAT 3D signal amplitude is expected for a constant slope in the entrance region of the Bragg curve. The linear fits do not intersect the origin of the graph, which reflects the constant noise levels of the signal traces: For RCF entrance doses below 0.0035 Gy·cm^2, the signal is lost in the electric noise. For the 12 and 14 MeV data sets, the Pearson coefficient R^2 exceeds 0.99, confirming the excellent correlation between the results of both detectors. In the case of the 16 MeV data set, a correlation coefficient of $R^2 > 0.91$ is determined. At higher bunch energies, fewer particles are expected from laser-proton sources, resulting in increased noise dominance and, thus, a reduced correlation coefficient. Interestingly, the slope of the linear fits increases monotonously with the design energy decreasing from the 16 MeV data set to the 12 MeV data set. This is a remarkable hint that the Bragg curve becomes steeper in the entrance region with decreasing particle energies, as shown in figure 2.5.

Table 4.1: Parameters of the energy-dependent calibration of the I-BEAT 3D entrance window signal to the bunch particle number according to equation 4.1.

Design energy (MeV)	Slope m (V^-1)	y-Intercept b
12	$(8.8 \pm 0.3) \cdot 10^6$	$(2.6 \pm 1.0) \cdot 10^5$
14	$(1.3 \pm 0.05) \cdot 10^7$	$(-3.8 \pm 1.3) \cdot 10^5$
16	$(1.15 \pm 0.13) \cdot 10^7$	$(2.7 \pm 1.9) \cdot 10^5$

In order to relate the dose deposited in a single RCF layer to the total particle number contained in the bunch, the result of six RCF stack measurements for each of the three energy settings is used. The total number of particles contained in the stack is deduced according to equation 3.9 and fitted linearly to the total dose deposited in the first layer of the stack. The data of the RCF stack measurements is shown in reference [102]. Employing this relation for the RCF entrance dose, figure 4.4b) shows the I-BEAT 3D signal amplitude versus the estimated bunch particle number N for the same shots as in figure 4.4a). Linear fits are applied to each design energy, and the relatively large error bars are due to the varying shape of the Bragg curve, with the uncertainty of the particle number dominated by the uncertainty of the fit between the total particle number and the entrance dose.
The energy-dependent calibration of the I-BEAT 3D detector is obtained based on the theoretical expectation of a linear correlation between the total particle number and the entrance window signal amplitude. The calibration is given by

$$N = m \cdot A_{\mathrm{ax}} + b \tag{4.1}$$

where N represents the total particle number. The calibration parameters m and b are determined from the linear fit of each data set and are provided in table 4.1. For a constant signal amplitude, which corresponds to a constant energy deposition in the entrance window, a larger particle number is required for larger bunch energies (compare figure 2.5). Figure 4.5 shows the amplitude of the window signal A_{ax} as a function of the IC signal recorded on same shot level. This data is recorded at the ALBUS-2S beamline. For these measurements, the laser energy was varied between 12 and 30 J in order to cover a wide range of proton numbers at the detector position. The given IC signal is the charge collected on the detector electrodes (without further data processing). However, the relation between deposited energy in the detector volume and read-out charge at

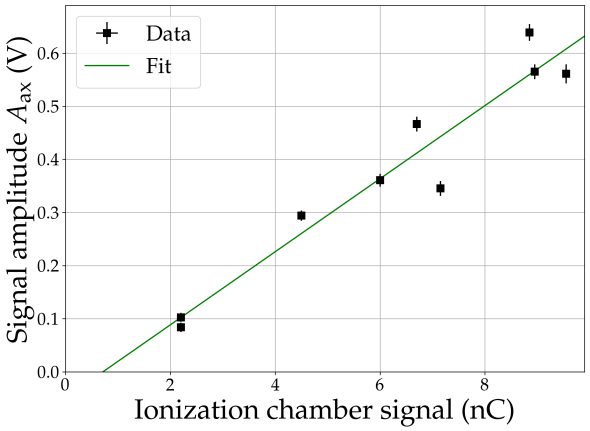

Figure 4.5: The amplitude of the ionoacoustic signal envelope generated in the I-BEAT 3D entrance window is displayed in dependence of charge measured with the ionisation chamber for various bunch particle numbers. Additionally to the black data dots, the linear correlation curve is shown in green.

the electrodes could be nonlinear for high particle fluxes [106]. The uncertainty of the I-BEAT 3D signal is given by the noise level in the recorded signal. The correlation between the window signal amplitude in I-BEAT 3D (a measure for the proton fluence) and the IC-reading (a measure for the proton number) is $R^2 = 0.93$. If both IC and I-BEAT 3D would be ideal detectors and the lateral bunch size is constant, a linear relationship is expected as for the dependence of the I-BEAT 3D result on the RCF dose presented in the previous paragraph. For interpreting the above observations, it is important to note that the IC signal and the laterally integrated dose in the RCF reference layer are sensitive to the energy deposited in the entrance region of the Bragg curve. The amplitude of the I-BEAT entrance window signal is related to fluence.

4.1.4 Signal reconstruction

In this chapter, the parameters of individual proton bunches recorded at both the LION and ALBUS-2S beamlines are determined. Figure 4.6a) shows a filtered and normalised axial signal trace measured at LION (I-BEAT 3D configuration B) in red. A mean energy of $E = 12.3 \pm 0.7$ MeV is deduced from the data. This energy is smaller than the design energy 14 MeV. This is due to the material positioned upstream I-BEAT 3D. The RCF reference layer is particularly significant and causes an energy reduction of approximately 1.2 MeV for a bunch with a 14 MeV entrance energy. The energy spread is calculated to $\sigma_E = 0.62 \pm 0.08$ MeV. In order to determine the energy spread, a shortest possible acoustic pulse $w_{min} = 0.53$ mm is assumed from the results recorded

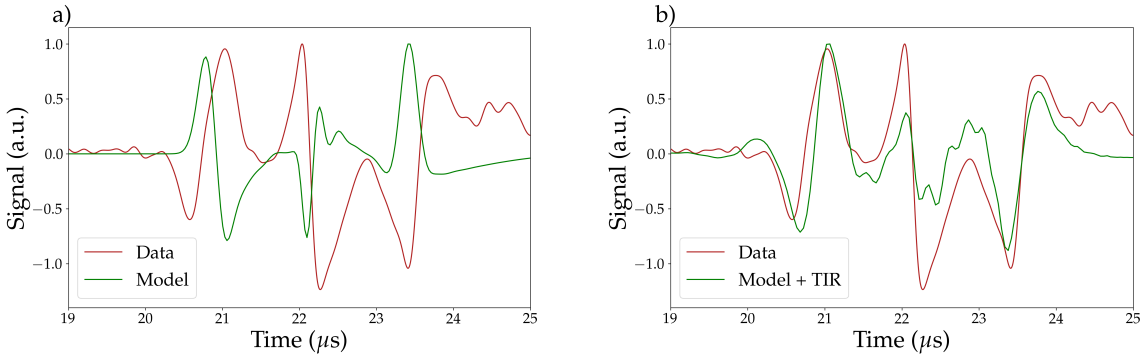

Figure 4.6: a) Comparison of experimental data recorded at the LION beamline to the theoretical model. The bunch parameters used as input for the model are $E = 12.3$ MeV, $\sigma_E = 0.62$ MeV and $\sigma = 1.5$ mm. In b), the theoretical model is convolved with the TIR determined from the entrance window signal.

at the ALBUS-2S beamline. However, it should be noted that the set-up varies slightly between both experimental campaigns, and thus w_{min} can vary as well. The energy spread is approximately 5% of the mean energy, which is about twice the result which was obtained by simulations of the LION beamline presented in reference [73]. By analytical calculations according to formula 2.31, broadening of the energy distribution caused by straggling in the additional RCF layer not considered in the simulations is found to be below 0.01 MeV and, therefore, negligible. Imprecise positioning of the PMQ magnets may have a more significant influence on the energy resolution [73]. The lateral signal width in this particular shot is determined to be $w_{\text{lat}} = 4.6 \pm 0.4$ mm. This result agrees remarkably well with the measurements presented in figure 4.3b) for the $d = 3$ mm collimator, despite the fact that those measurements were conducted at the ALBUS-2S beamline. The absolute bunch particle number is calculated to be $N = (5.7 \pm 0.6) \cdot 10^6$ protons based on the entrance window signal amplitude and the correlation established in figure 4.4.

To validate the bunch parameters determined from the experimental signal trace, a signal trace is computed using the analytical model developed in section 2.3. As input parameters, the mean energy and energy spread determined from the analysis of the experimental signal trace are used. The choice of lateral bunch width is not obvious, as the theoretical model is based on Gaussian lateral distributions, while realistic proton foci are typically characterised by more complex shapes. Pragmatically, a lateral bunch width of $\sigma = d/2 = 1.5$ mm is assumed based on the collimator size. The theoretical signal, calculated using equations 2.42 and 2.62, is shown as the green trace in figure 4.6a) along with the experimental data. For a fair comparison, the theoretical signal is

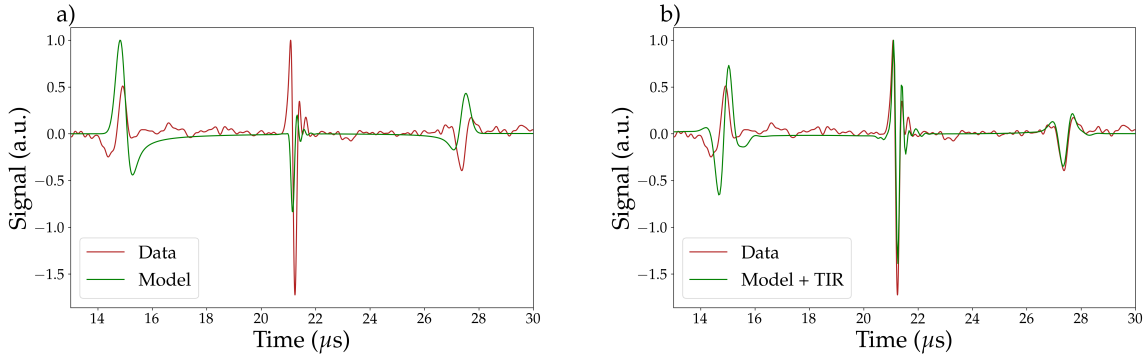

Figure 4.7: a) Comparison of an experimental data recorded at the ALBUS-2S beamline to the theoretical model. The bunch parameters used as input for the model are $E = 30.6$ MeV, $\sigma_{\mathrm{E}} = 0.46$ MeV and $\sigma = 1.5$ mm. In b), the theoretical model is convolved with the TIR determined from the entrance window.

filtered in the same way as the experimental signal. While the frequency components of the experimental signal are well reproduced, a dominant phase shift is visible, likely due to the detector response. In figure 4.6b), the green trace shows the theoretical signal model convolved with the TIR. The experimental signal trace is plotted again in red for comparison. The TIR is determined by comparing the experimental and theoretical entrance window signal of a different shot with 12 MeV design energy, as described in section 3.4.1. The model now resembles the shape of the experimental trace. The main deviation between the model and the experimental data is that the model underestimates the amplitude of the entrance window signal compared to the BP signals. One reason might be limited precision in determining the lateral bunch distribution which influences the amplitude of the acoustic signals as visible in figure 2.9. Figure 4.7a) shows in red a filtered and normalised experimental signal recorded at the ALBUS-2S beamline for a design energy of 30 MeV and with the $d = 3$ mm collimator. From the signal trace, a mean energy of $E = 30.6 \pm 0.3$ MeV and an energy spread of $\sigma_{\mathrm{E}} = 0.46 \pm 0.08$ MeV are deduced. The energy spread is thus approximately 1.5% and is expected to be influenced by the collimator. The focusing properties of the solenoid induce spatio-spectral couplings, resulting in protons with energies different from the design energy being guided with larger lateral bunch diameters compared to protons with energies close to the design energy. As a result, the collimator truncates the proton spectrum and reduces the energy spread. The energy spread of several proton bunches without collimator is shown in figure 4.2. As an example, a shot with equal design energy but without collimator yields an energy spread of $\sigma_{\mathrm{E}} = 0.82 \pm 0.03$ MeV, corresponding to a relative spread of 3%. The lateral signal width is determined from the right transducer

signal and yields $w_{\mathrm{lat}} = 4.5 \pm 0.4$ mm, corresponding to the 3 mm collimator. This result agrees with the measurements presented in figure 4.3b). Consequently, a lateral bunch width of $\sigma = 1.5$ mm is assumed, as was done for the LION trace reconstruction. The absolute calibration determined at LION is not applicable for the data collected at the ALBUS-2S beamline because of the different set-ups, particularly in the charge and voltage amplifiers, as discussed in section 3.2.
The green trace in figure 4.7a) presents the theoretically modelled and filtered signal based on the determined bunch parameters. Similarly to the LION signal reconstruction, this model is convolved with the TIR determined through comparison of the experimental and theoretical entrance window signals from a different shot (see section 3.4.1). The result is shown as the green trace in figure 4.6b) along with the experimental signal trace in red. The shape of the experimental trace is reproduced well by the model, confirming the determined bunch parameters. Similar to the LION result, the amplitude of the three peaks relative to each other differs between the experimental and theoretical signal traces.

4.2 TI-BEAT

4.2.1 Lateral bunch properties

Figure 4.8 presents the TI-BEAT results on the lateral bunch position measurements at SIS18. For this data set, a collimator of $d = 3$ mm diameter and 10 cm thickness is positioned upstream the TI-BEAT detector. In panels a) and b), the mean TI-BEAT signal position P_{lat} deduced from the right and the left transducer signal, respectively, is plotted versus stage position, which is considered as ground truth. The uncertainty bars represent the standard deviation of each sample consisting of approximately 40 bunches. Since the stage offers a precision <15 μm, the uncertainty of the stage position is neglected. For further assessment of the TI-BEAT result, panels c) and d) display the deviation between the TI-BEAT mean value and the nominal position for the right and left transducer, respectively. Again, the standard deviation of the sample is depicted as uncertainty bar, which is approximately ± 0.15 mm. This statistically determined value agrees well with the theoretical estimated measurement uncertainty of $\lambda_{\mathrm{min}}/2 = 0.18$. For all stage positions, the TI-BEAT mean value deviates less than 0.15 mm from the nominal value. Within the uncertainties, the TI-BEAT mean value coincides with the nominal position for all but two stage positions. This measurement is susceptible to the trigger signal, as any delay directly translates into an offset of the recorded signal trace and, consequently, affects the signal position. For example, a jitter of 0.01 μs in the trigger signal would lead to an error of 0.015 mm in the determined bunch position. However, this contribution is relatively small compared to the overall uncertainty of the measurement and is therefore not further considered. When comparing the results of the left and right transducers in panels c) and d), it can be observed that the independently measured and deduced TI-BEAT signal positions show the expected anti-correlation between the two transducers. In figure 4.9, the width of the ionoacoustic signal w_{lat} is shown as a function of the collimator size d for all three transducers. The thickness of the collimators used in this scan is 3 cm. Each data point represents the mean of each sample (approximately 40 bunches), and the error bar represents the standard deviation. There is one data point with an outstandingly large standard deviation of 0.37 mm, which corresponds to the sample recorded with the $d = 5$ mm collimator and the left transducer. This large standard deviation is due to one single signal trace in which the FWHM algorithm did not correctly determine the half-maximum position of the principal signal peak but of a nearby peak. For all other points, the standard deviation lies between 0.01 and 0.07 mm, which is too small to be visible. The 10 MHz right and

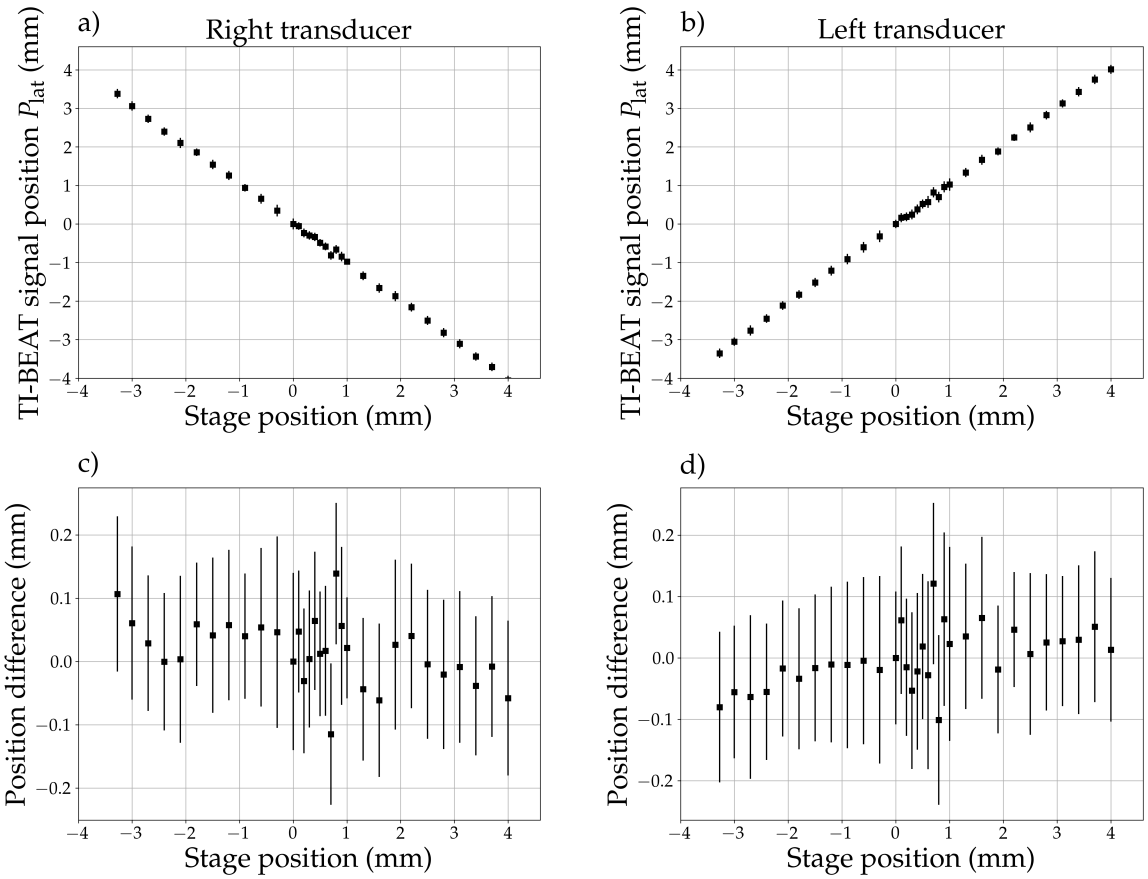

Figure 4.8: TI-BEAT result of the lateral bunch position deduced from the a) right and b) left transducer in dependence of the stage position. In c) and d), the difference between the TI-BEAT result and the stage position is also shown in dependence of the stage position for the right and left transducer, respectively. Each data dot represents the mean value of the sample; the standard deviation is shown as error bar.

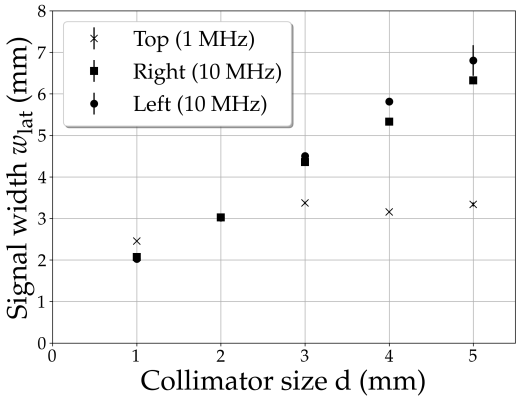

Figure 4.9: TI-BEAT lateral signal width in dependence of the collimator size for all three transducers. Each data dot represents the mean value of the sample; the standard deviation is shown as error bar.

left transducers show similar results, with a clear trend towards larger signal widths for increasing collimator sizes. By extrapolation, a signal width $w_{\text{lat}} \approx 1$ mm is expected for a theoretical collimator size of $d = 0$ mm. This is in line with the results presented in section 4.1.2, considering the response of the detection system. For collimator sizes of 3 mm and larger, the signal width recorded with the top transducer stays rather constant, unlike the right and left transducer results.

To further assess the influence of the nominal transducer bandwidth, figure 4.10 shows the filtered signal traces in frequency domain of individual shots recorded with the top and the right transducer for collimator diameters ranging from 1 to 5 mm. The right transducer signal is representative for a 10 MHz transducer and is thus very similar to the left transducer result. The power spectrum allows to determine the mean frequency of the signal $\hat{f}$ by

$$\hat{f} = \frac{\sum f_i A(f_i)}{\sum f_i} \tag{4.2}$$

with f_i being the contributing frequencies and $A(f_i)$ the Fourier amplitude of each frequency. $\hat{f}$ decreases monotonously from 0.96 to 0.45 MHz with increasing collimator size for the top transducer and from 1.2 to 0.5 MHz for the right transducer. To ensure a proper comparison of $\hat{f}$, the cut-off frequency of the lowpass filter is here adapted to be $f_{\text{max}} = 4$ MHz for both transducers. The difference between the top and right transducer traces is representative of the differing transducer response functions, which match the central design frequency trend. The central design frequency is lower for the top transducer (1 MHz) and higher for the right transducer (10 MHz).

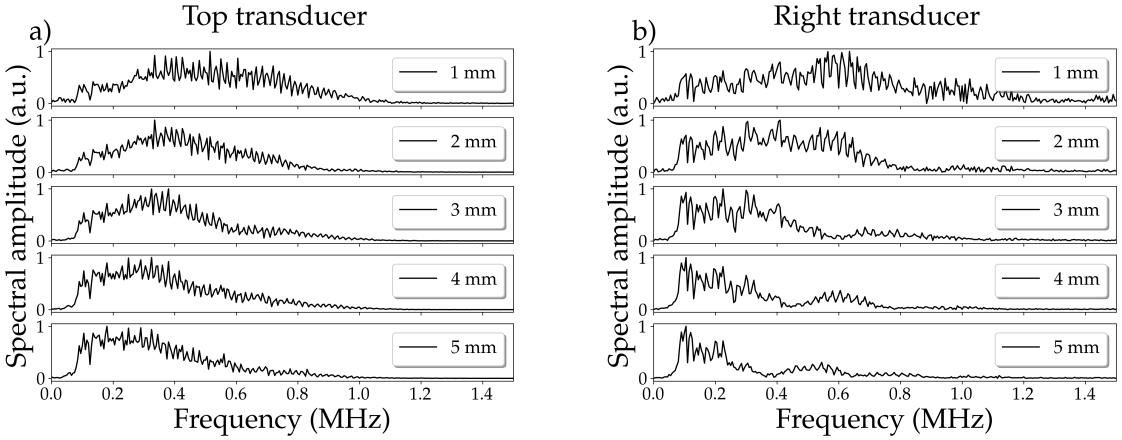

Figure 4.10: Normalised spectral amplitude of the a) top and b) right transducer TI-BEAT signal for collimator diameters from 1 to 5 mm.

4.2.2 Bunch particle number

To assess the sensitivity of the TI-BEAT detector to the bunch particle number, the signal amplitude is compared to the SEETRAM result. Figure 4.11 shows both detector results. The data presented in this paragraph was collected using a collimator with a diameter of $d = 3$ mm and a thickness of 10 cm. Only the right transducer result is shown as an example; the corresponding figures for the left and top transducers would look similar. The data set is recorded for seven different settings of the bunch particle number, with nominal values ranging from 5.2×10^7 to 2.3×10^9 particles per second, as deduced from the current transformer measurement and indicated by the colour code. However, it should be noted that the collimator placed upstream of the TI-BEAT detector only transmits a small portion of the beam, resulting in the detected bunch particle numbers being much lower than the nominal values. The TI-BEAT and SEETRAM detector measurements show a very strong correlation, with Pearson coefficients ranging from 0.9985 to 0.9987, depending on the transducer being evaluated. The noise level of the signal trace, which is maximally 0.05 V, serves as a measure of the precision of the TI-BEAT result. As the noise level does not depend on the bunch particle number, the relative uncertainty of the measurement decreases with increasing particle number, leading to improved precision for higher bunch intensities. For the SEETRAM result, reference [99] reports a total accuracy of 2% composed of a statistical uncertainty of 1% and possible systematic uncertainties in a calibration study. These values were obtained from measurements with xenon ions, similar to the ones used in this study, albeit at a different isotope with an atomic mass of 136 u and an energy of 600 MeV/u. While the

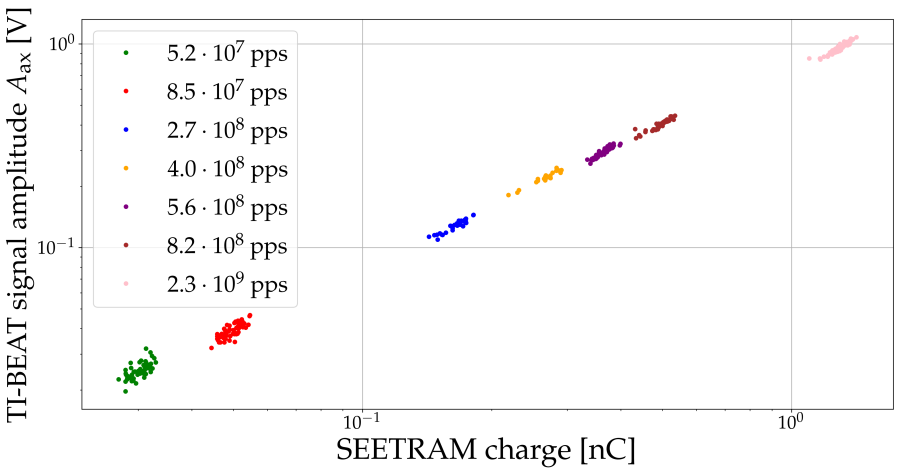

Figure 4.11: The amplitude of the ionoacoustic signal envelope measured with the right transducer along with the corresponding SEETRAM result. The nominal bunch particle number in units of particles per spill (pps) indicated by colour is given in the legend.

accuracy might be affected by the ion species and energy, the provided uncertainties serve as a valuable benchmark. To improve visibility, uncertainty bars are not shown in the figure.

To further evaluate the precision of the TI-BEAT detector, the signal amplitudes of the three TI-BEAT transducer traces are compared to each other. As an example, figure 4.12 shows the TI-BEAT result of the right and the left transducer. The figure clearly shows the increased fluctuation in the signal amplitudes at lower bunch particle numbers, which is caused by the constant absolute uncertainty of the measurement. The Pearson coefficients calculated between the right and left transducer, right and top transducer, and top and left transducer results are between 0.99976 and 0.99983. This quantifies the high correlation between the signal amplitudes measured by different TI-BEAT transducers. Interestingly, the correlation between the TI-BEAT transducers is even higher than the correlation of each transducer result with the SEETRAM detector. The standard deviations of the samples recorded with the TI-BEAT transducers and the SEETRAM detector are displayed in figure 4.13 for the various nominal particle numbers. The SEETRAM variation is consistently smaller than the variation observed in all three transducer results. The variation in the TI-BEAT transducer results decreases with higher particle numbers, which is consistent with considering noise as the main source of uncertainty. More precisely, the absolute noise level of 0.05 V translates into a relative noise level of 5% for the highest available beam current of $2.3 \cdot 10^9$ pps. Therefore, noise is the main cause for the determined standard deviation of 6%. Interestingly, the difference

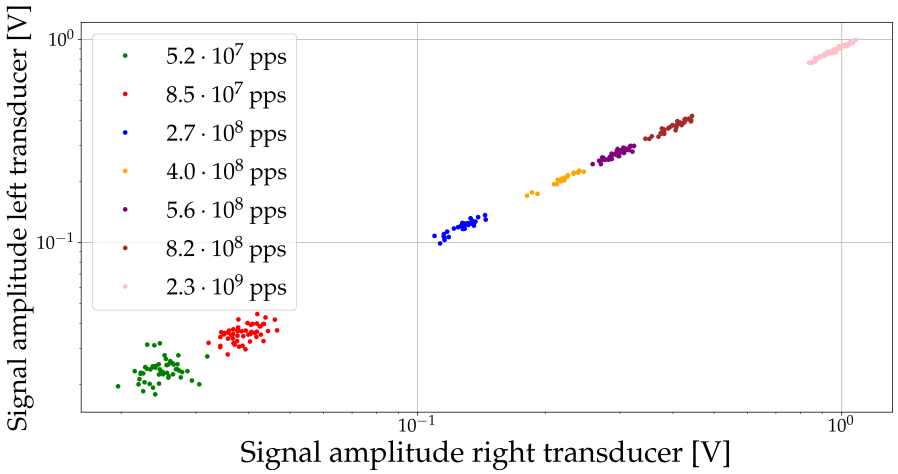

Figure 4.12: Correlation of the envelope amplitude deduced from the right and left transducer signal. The nominal bunch particle number indicated by colour is given in the legend.

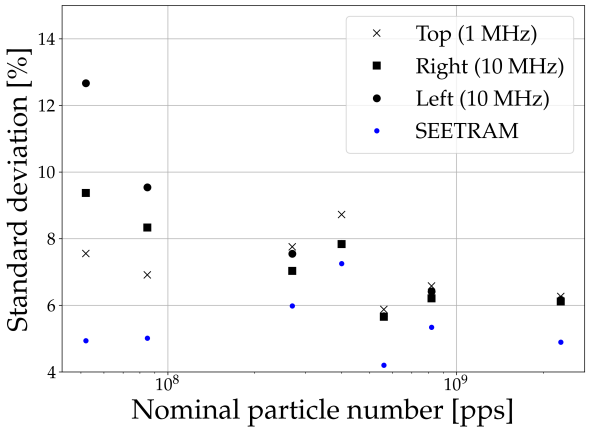

Figure 4.13: Standard deviation of the TI-BEAT signal amplitude recorded with the top, right and left transducers and the SEETRAM result for various nominal bunch particle numbers.

between the three transducer results decreases with higher particle numbers, and it is hardly visible for the highest available beam current. The displayed uncertainties represent an upper bound for the measurement precision of both the SEETRAM and the TI-BEAT detectors with the given set-up and bunch properties. This assumes that there is no variation in the bunch particle number between individual bunches. However, the clear correlation observed between both detector results for each nominal beam current visible in figure 4.11 indicates that there is indeed a variation in the bunch particle number. A lower bound for the TI-BEAT precision is given by the SEETRAM variation, which assumes that the SEETRAM does not induce statistical measurement uncertainty.

5 Discussion

I-BEAT 3D The I-BEAT 3D detector is equipped with four transducers, providing acoustic traces in four spatial directions. As expected, the analysis of the envelope of the filtered raw signal amplitudes reveals the position and the width of the BP volume. The accuracy of this position is currently limited to the resolution limit defined by the maximal detectable frequency and the SNR. For the 10 MHz piezoelectric transducer combined with the voltage amplifier used in this study, the position accuracy is 0.04 mm. The SNR is dominated by the employed amplifier. Improvements in SNR can be achieved by using the novel charge amplifiers, resulting in an eight-fold enhancement compared to the voltage amplifier.

In axial direction, this analysis yields an absolute measure of the proton range [19,20] and hence kinetic energy before entering the water reservoir immediately, with a maximum deviation to the TOF spectrometer of 0.8 MeV. Analysis of the width of the signal envelope allows in addition fast monitoring of the width of the BP, which serves as a measure of the energy spread dE/E. Equation 2.68 describes the relationship between the measured signal width and the bunch energy accurately. Based on the comprehensive analytical model for the ionoacoustic signal, equation 2.74 enables the determination of the absolute energy spread from the axial signal width. The detector response is thereby considered through a single parameter $w_{\min}$ that describes the signal broadening. This approach depicts a simplified and rapid method to support high repetition rate bunch monitoring without the need for a calibration source as $w_{\min}$ can be determined from the fit of the axial bunch width scan. While the minimal resolvable wavelength $\lambda_{\min}/2 = 0.18$ mm for the 10 MHz transducer combined with the voltage amplifier is similar to the signal broadening of 0.23 mm by the EIR estimated in section 2.3.4, the experimentally determined value of $w_{\min} = 0.53 \pm 0.07$ mm is considerably larger. This discrepancy is partly due to straggling in all beamline components. For the ALBUS-2S beamline setup, the energy spread induced by straggling of a bunch with $E = 30$ MeV is estimated by equation 2.31 to be 0.22 MeV, with the detector water volume being the main source of straggling. The analytical model describing the relationship between energy spread and axial signal width depends on the lateral signal size. For instance, in section 4.1.4, the energy spread is overestimated by 7% because the lateral bunch width is assumed

to be $\sigma = 0.5$ mm in the analytical model, whereas the true value in the experiment is $\sigma = 1.5$ mm. Although this deviation is acceptable for certain applications, the analytical method allows for determining specific parameters for the lateral bunch width in less than one second if necessary.

The relation between lateral signal width and aperture diameter is well described by eq. 3.2. The minimum signal width w_0 is smaller for the top transducer than for the right transducer, which is expected due to its larger frequency bandwidth. The difference in w_0 between the two transducers thus confirms our signal modelling. However, the width of both lateral signals remains considerably larger than the minimal resolvable wavelength, and straggling within the remaining 8 cm of air after passing the collimator as well as the water cannot account for this. This hints at additional contributions, for example, by the vacuum exit window and the collimator itself [107], and deserves further investigation.

Particularly interesting is the scaling of the ionoacoustic signal generated in the entrance window of the I-BEAT 3D detector with the number of particles in the bunch. Through the cross-calibration with RCFs, an online measure of proton performance in the focus of the proton bunch at LION is now at hand. Calibration parameters for energies of 12, 14, and 16 MeV are determined to account for the energy-dependent dose deposition in the entrance window. However, the calibration parameters do not strictly follow the analytically expected behaviour on the bunch mean energy. This deviation arises from a limited correlation between the dose deposited in the entrance region of the Bragg curve and the dose deposited in the BP region. This limitation indicates that relying solely on the entrance window signal may have constraints. While the entrance window signal has the advantage of being insensitive to minor changes in energy spread, it can provide misleading results when major deviations from a Gaussian energy spectrum occur. This is because the signal is sensitive to the dose deposited in the entrance region of the Bragg curve, disregarding significant variations in the Bragg peak's dose deposition. However, for laser-accelerated ions, the shape of the Bragg curve can vary substantially [102]. To address this limitation, a more sophisticated reconstruction algorithm could consider the amplitude of the BP signal in addition to the entrance window signal. Further, the entrance window signal is sensitive to proton bunch fluence, and not just particle number, which can be seen in equation 2.42. As an example, when increasing the lateral signal width of a 30 MeV proton bunch from 3 mm to 3.1 mm, the pressure amplitude is decreased by approx. 5%. If the change in lateral signal width is known, such as through information provided by the lateral transducer, the calibration factors can be adjusted

accordingly. While the given calibration parameters are specific to the employed detector setup, it is possible to adapt the calibration for different detector designs, such as a larger distance between the entrance window and axial transducer, using the analytical model. However, this adjustment is limited to the detector geometry, as changes in hardware components primarily affect the conversion of pressure into voltage, i.e. the EIR, and require measurement rather than easy derivation. The calibrated I-BEAT 3D signal enables the determination of the absolute particle number in the focus of the LION beamline. Employing charge amplifiers instead of voltage amplifiers significantly improves the detection threshold, with a minimum of $1 \cdot 10^6$ particles detected in this study. It should be noted that the detection threshold also depends on other bunch parameters, such as the energy spread.
The entrance window signal exhibits a correlation with the ionisation chamber signal, albeit with deviations larger than the individual uncertainties. This discrepancy may be attributed to variations in the lateral bunch size, which can influence the results obtained by the I-BEAT 3D detector. However, the lateral signal width does not show corresponding changes, possibly due to limited resolution. It should be noted though, that the scaling of the IC signal with the total particle number becomes nonlinear for high fluxes [106]. It is also worthwhile mentioning that similar to the single RCF, the IC signal is proportional to the dose in the entrance region of the Bragg curve, and thus, it also depends on the energy spectrum.
The systematic studies on the relationship between particle properties and ionoacoustic signal are applied to deduce the bunch parameters for one shot each recorded at the LION and ALBUS-2S beamlines, demonstrating the feasibility of online monitoring of three-dimensional particle bunch properties at a frequency of 1 Hz, and potentially even higher repetition rates. The signal shape is particularly well replicated when the EIR is taken into account. It is a particularly valuable asset that the TIR can be obtained by comparing the calculated and measured entrance window signals. This innovative method of assessing the detector response complements the more established methods, which mainly rely on a dedicated broadband calibration source [93].

TI-BEAT The TI-BEAT detector offers a non-destructive means of monitoring high-energy ion bunches. Unlike the I-BEAT 3D detector, which captures the ionoacoustic signal generated within the Bragg peak (BP), the TI-BEAT detector utilizes three transducers to receive the waves emitted laterally from the entrance region of the Bragg curve. Consequently, the signal amplitude is expected to be reduced in proportion to the

ratio between the dose in the entrance region and the dose in the BP. By analyzing the envelope of these signals, the TI-BEAT detector enables the monitoring of lateral bunch parameters in two dimensions, along with determining the number of particles contained within a bunch. Similar to the I-BEAT 3D detector, the resolution of the TI-BEAT detector is constrained by the maximum detectable frequency and the signal-to-noise ratio (SNR). The high repetition rate of the SIS18 synchrotron facilitates the acquisition of a substantial data set consisting of approximately 40 bunches recorded for each experimental configuration. While the bunch parameters are deduced for each individual bunch, the large data set allows for statistical analysis of the derived parameters, thus enabling an assessment of the precision of the ionoacoustic method. Furthermore, the experiment demonstrates the capability of data acquisition at repetition rates exceeding 1 Hz, showcasing the readiness of ionoacoustic detectors for high repetition rate laser-driven particle sources.

The analysis of the lateral signal position enables the determination of the lateral bunch position. The standard deviation of the samples provides valuable information regarding the precision of the measurement, which is consistently found to be below 0.15 mm. The fluctuation in signal position can partly be attributed to electronic noise, predominantly caused by the amplifier. Another contributing factor could be variations in the lateral dose distribution. Addressing this issue would require a more sophisticated data analysis approach, as the current simple readout routine based on a single parameter may not adequately account for these variations. The mean signal position exhibits a deviation of less than 0.15 mm from the known position of the bunch defined by the collimator relative to the detector. This provides an indication of the system's accuracy in determining the lateral bunch position. Notably, this deviation does not appear to be random, but rather a correlated systematic trend is observed over the 8 mm scan range for both lateral transducers. Additionally, the deviation becomes more pronounced around the centre of the detector, which coincides with the focus of the left and right transducers. Consequently, it is likely that the deviation of the mean signal position is influenced by the SIR, which is known to vary in the focal region of the transducers [93].

The correlation between the lateral signal width and the bunch diameter depends on the frequency of the transducer. For small collimator diameters, such as 1 mm and 2 mm, a single-cycle acoustic pulse is expected to originate with frequencies of 1.5 and 0.75 MHz, respectively. Both the 1 MHz and 10 MHz transducers are capable of resolving these frequencies. However, for larger collimator sizes, the lateral dose distribution is more likely a flat-top profile. The presence of two lateral gradients along the transducer axis

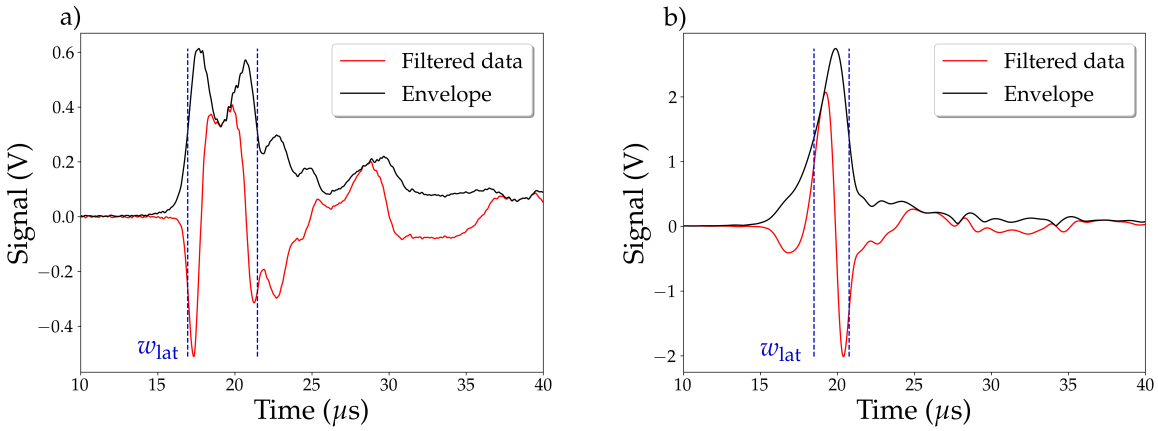

Figure 5.1: Lateral ionoacoustic signals recorded with the a) 10 MHz left transducer and b) 1 MHz top transducer of the TI-BEAT detector. Curves represent the lowpass filtered data (red) and the signal envelope (black). The readout positions of the lateral signal width w_{lat} are shown in blue.

generates acoustic waves with higher frequency components, dependent on the steepness of the gradient and the scattering in the collimator and the TI-BEAT detector. Figure 5.1 shows the recorded signal for the 5 mm collimator, presenting the filtered signal and its envelope, along with the half-maxima positions for the 10 MHz left transducer in (a) and the 1 MHz top transducer in (b). The 10 MHz transducer is able to resolve two separate peaks corresponding to the gradients in the flat-top beam profile, whereas the slower response of the 1 MHz transducer results in a single electric pulse. This highlights the significance of the EIR. Furthermore, it becomes evident that for larger beam diameters, relying solely on the FWHM position may not provide an accurate assessment of the beam width. This represents a general limitation of the simple data analysis method, as monitoring the envelope FWHM is only suitable for single-cycle pulses within the transducer's bandwidth. Comparing the results of the lateral signal width between the I-BEAT 3D and TI-BEAT detectors, it may seem surprising that the 1 MHz transducer provides a reasonable measure for the signal width at larger collimator sizes only for the I-BEAT 3D detector. However, this discrepancy is not attributed to the different detector designs but rather to the distinct characteristics of the accelerator types used in the experiments. In particular, the particle bunch in the focus of the ALBUS-2S beamline is smaller in size compared to the SIS-18 beam. As a result, the influence of the collimator on the lateral dose distribution is diminished in the experiments conducted at the ALBUS-2S beamline. This leads to shallower gradients and, consequently, a lower frequency component in the lateral dose distribution, in contrast

to the high-frequency component present through the sharp flat-top profile expected at the SIS-18 beamline. This observation highlights that the lateral dose distribution is not solely determined by the collimator but rather influenced by other factors such as the beam profile. Furthermore, it should be noted that the fast readout routine utilized in this study is not specifically designed to reconstruct the full two-dimensional dose distribution but rather to provide a simple measure for the lateral beam width. Although the accuracy of the signal width as a monitor for the bunch width depends on the minimal resolvable frequency and, consequently, the EIR, the small standard deviations of the mean signal widths demonstrate the nevertheless high precision of the measurement. In principle, the lateral signal width of the TI-BEAT detector should also follow equation 3.2. However, since the acquired data only falls within the linear range of the model, it does not provide information on the beam waist that determines w_0. Therefore, fitting methods cannot accurately describe the beam waist. Compared to the lateral transducers of the I-BEAT 3D detector, the 10 MHz lateral transducers used in this study are expected to have a faster impulse response and thus a smaller w_0, which could be further assessed by employing collimators with even smaller diameters. An additional challenge in evaluating the lateral signal width arises from the relatively elongated bunch length, which is on the order of 0.3 μs, comparable to the stress confinement time of 0.67 μs estimated for a 1 mm diameter bunch. Consequently, the ionoacoustic wave triggered by the rising edge of the ion bunch has already travelled through a significant portion of the energy deposition volume when the last ions arrive, leading to the smearing out of the ionoacoustic signal. The amplitude of the lateral signal traces exhibits a strong correlation with the SEETRAM result regarding the bunch particle number, covering a large dynamic range of nearly two orders of magnitude. At lower particle numbers, the measurement is limited by the noise level of the TI-BEAT detector, which is predominantly influenced by the amplifiers. However, employing charge amplifiers instead of voltage amplifiers is expected to improve the SNR by a factor of eight. It should be noted that the lowest resolved bunch particle number in this study may not be representative of the detector setup in general, as its sensitivity also depends on factors such as the lateral beam shape and the type of particle under investigation. The highest beam current in this study is defined by the limit of the accelerator machine. It is anticipated that the TI-BEAT detector can provide information on beams with much higher bunch particle numbers with adequate adaption of the amplifier, with the ultimate limitation potentially being the boiling of the water, which can affect the linearity of the measurement result. No upper limit has been observed in ionoacoustic studies thus far. In addition, the accuracy of the measurement

improves as the particle numbers increase; so far it is between 4% and 6% for the highest investigated beam current. An interesting finding is that the results from the three TI-BEAT transducers exhibit a stronger correlation compared to the correlation between TI-BEAT and SEETRAM results. This suggests a potential change in the lateral beam profile, as the collimator positioned between SEETRAM and TI-BEAT only transmits a small subset of the particles, thereby indicating that the TI-BEAT result is specifically related to this subset of particles and this cannot be monitored by the SEETRAM.

6 Conclusion and Outlook

The primary scientific goal of this work is successfully achieved through the demonstrated monitoring of the three-dimensional properties of focused laser-accelerated protons using the ionoacoustic approach. The study introduces the I-BEAT 3D and TI-BEAT detectors as novel tools for particle bunch monitoring. These detectors, along with their fast and straightforward data analysis based on a comprehensive analytical model, now offer a compact, simple, and cost-effective online solution that complements the existing suite of particle detectors.

The developed theoretical model serves to describe the complete ionoacoustic signal of I-BEAT 3D, in particular the axial signal, using analytical methods. Its purpose to establish a connection between particle bunch parameters, such as mean energy and energy spread, and the characteristics of the ionoacoustic waves is fulfilled. One notable improvement of this model compared to previous work is its more precise description of the detector entrance window. It takes into account the two boundaries of the window representing an acoustic etalon, resulting in a deeper understanding of the axial ionoacoustic signal. Additionally, the theoretical model forms the foundation for the absolute calibration of the I-BEAT 3D detector and provides insights into the effects of variations in the proton bunch parameters on the calibration.
The I-BEAT 3D detector is demonstrated to monitor important bunch parameters of focused and energy-selected proton bunches at two laser-driven particle sources. The information provided by the additional transducers adds lateral bunch information to previous I-BEAT set-ups. Operating four transducers enables estimates of the position and size of the BP in three dimensions, and this relates to the main parameters of the six-dimensional phase space distribution of the bunch. This is a clear advantage over previous I-BEAT versions. In addition, the bunch particle number is accessible. The fast and simple data analysis is an integral part of the I-BEAT 3D detector and reveals the position and size of the BP in I-BEAT 3D with sub-mm resolution. This is a very satisfying result for a simple monitor with immediate feedback. Compared to the previously used simulated annealing approach [59] demonstrated for dose reconstruction in the axial dimension (i.e. the depth dose curve), the here presented fast data analysis

has the advantage that the extraction of information becomes compatible with 1 Hz operation and probably much higher repetition rates. Having in mind that a complete reconstruction of the depth dose curve is possible, for many use cases rapid feedback on the properties of a focused proton bunch is sufficient.
Ionoacoustic bunch monitoring is not solely reliant on the acoustic waves emitted in the BP region. The measurements with the TI-BEAT detector prove that the lateral transducers can monitor the lateral bunch properties and the absolute particle number in transmission mode.

An intriguing alternative for reconstructing complex three-dimensional dose distributions could involve training a neural network to establish relationships between transducer signals and dose distribution, as well as beam parameters. A significant prerequisite for this approach is a substantial collection of high-quality training data, which can now be supplied by the analytical model. Additionally, incorporating the detector response function into the training process enhances the accuracy of the neural network. Consequently, the neural network could reconstruct complex dose distributions while also being fast.
Regarding the hardware, improvements in the accuracy of the demonstrated three-dimensional bunch reconstruction are anticipated through the utilization of transducers with larger bandwidth and an increased number of transducers [108]. Further, the influence of the SIR could be diminished by employing transducers which are smaller in diameter. However, it should be noted that this might also decrease the sensitivity. In order to accommodate non-destructive monitoring of lower energetic ions, the thickness of the TI-BEAT water column can be reduced. This modification could enable non-destructive monitoring of laser-accelerated ions.
The studies presented in this work primarily focus on the use of water as the detector medium. Preliminary investigations have been undertaken to explore the effects of alternative detector media. Specifically, the benefits of employing materials which exhibit an increased Grüneisen parameter have been examined. As an example, aluminium holds the potential to generate pressure amplitudes up to three orders of magnitude higher than water while absorption of the acoustic wave is similarly low [109]. Considering potential activation issues of the detector should be taken into account to ensure the safety and radiation hardness of the overall set-up and other practical issues should be investigated thoroughly though.

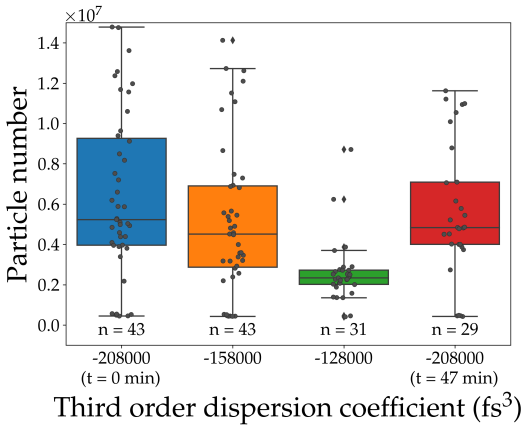

Figure 6.1: Bunch particle number deduced from the I-BEAT 3D signal for three different settings of the laser TOD coefficient. The initial setting -208000 fs^3 (blue) labels the shortest laser pulse and is set again after the scan (red). The particle numbers of the single proton bunches are shown as data dots. For better statistical assessment, the data is further visualized as a boxplot.

Despite of potential improvements, the presented ionoacoustic detector designs are ready for applications now. Through its rapid monitoring of proton bunches, the I-BEAT 3D detector holds potential for future applications in optimizing laser-driven particle sources. The particle number at the beamline focus can serve as a measure for assessing the efficiency of proton acceleration which can be inserted as feedback in the control system capable of manipulating the laser parameters. Machine learning algorithms, such as Bayesian optimization, can then effectively handle the complex interplay between laser and particle parameters. Impressive demonstrations of this approach have already been witnessed in the field of laser-electron acceleration [110, 111], and there is also one experimental study focusing on proton acceleration. However, it should be noted that this particular study was conducted using a smaller laser system and investigated lower energy protons with approx. 3 MeV, for which particle detection solutions already exist [112]. In contrast, the I-BEAT 3D detector presented here enables the monitoring of higher energetic ions, making it applicable to the current leading systems with lasers operating in the petawatt regime accelerating protons up to 100 MeV [35], provided that a beamline for focusing and energy selection is available.

In a first attempt, the acceleration performance is exemplarily varied by changing the laser pulse Third-Order Dispersion (TOD). Figure 6.1 presents the bunch particle number in the focus of the LION beamline for three different settings of the laser TOD coefficient with the PMQ magnets adjusted to a design energy of 12 MeV. Each data dot represents

a single particle bunch. To improve visibility, the error bars representing the signal noise level and the uncertainty of the absolute particle number calibration are omitted. For statistical analysis, a boxplot is used to visualize the median (central line), the first and third quartiles (upper and lower limit of the box), and the whiskers representing the 1.5 interquartile range. The initial setting of -208000 fs^3 corresponds to the shortest laser pulse and is repeated after the scan, which occurs 47 minutes later, to investigate possible systematic trends unrelated to our active manipulation. Online monitoring of the particle number allows for the acquisition of a large data set (n=146 shots) at a medium repetition rate (2.6 shots per minute), which is currently limited by the number of targets and the capacity of the IT infrastructure, respectively. Across all shots, particle bunch numbers ranging from 0 to 1.5×10^7 particles are observed, indicating pronounced variations. For meaningful comparison between the TOD settings, a statistical hypothesis testing is conducted [113]. Choosing a significance level of $\alpha = 0.05\%$, a significant deviation can only be found between the initial setting (TOD = -208000) and the TOD = -128000 setting with a p-value < 0.01. When comparing the two data sets corresponding to the shortest pulse collected at t = 0 min and t = 47 min, the p-value is 0.4, indicating no significant deviation. This first demonstration gives a glimpse of the possibilities that I-BEAT 3D can open up in the future.

A very interesting future application of ionoacoustic bunch monitoring is online dosimetry for radiobiological experiments conducted at laser-driven particle sources directly in the irradiated sample. This idea of miniature image guidance is motivated by the demonstrated sub-mm resolution in determining the location of the BP. Further, the capability of absolute dosimetry, as demonstrated in this work, can mediate the substantial shot-to-shot fluctuations typically observed [40, 41]. To achieve this, an ideal set-up would integrate ultrasonic detectors for bunch monitoring with the biological sample. For biological samples positioned in water, such as zebrafish embryos [40], the experimental set-up could involve the installation of ultrasonic transducers at the walls of a water phantom. In this regard, the use of smaller transducers, such as those based on foils made of piezoelectric polymer [114], could facilitate easier adaptation to fit a dedicated experimental set-up.

Last but not least, the I-BEAT 3D detection method, and more specifically TI-BEAT, is promising for beam monitoring beyond laser-ion acceleration wherever high dose rates apply, for example, in the context of FLASH radiotherapy [106].

Publications and Conference Contributions

Journal articles

- **S. Gerlach**, F. Balling, A. Schmidt, F. Brack, F. Kroll, J. Metzkes-Ng, M. Reimold, U. Schramm, M. Speicher, K. Zeil, K. Parodi und J. Schreiber, *High Power Laser Science and Engineering* **11** (2023), e38.
- N. Weiße, L. Doyle, J. Gebhard, F. Balling, F. Schweiger, F. Haberstroh, L.D. Geulig, J. Lin, F. Irshad, J. Esslinger, **S. Gerlach**, M. Gilljohann, V. Vaidyanathan, D. Siebert, A. Münzer, G. Schilling, J. Schreiber, P.G. Thirolf, S. Karsch und A. Döpp, *High Power Laser Science and Engineering* **11** (2023), e44.
- **S. Gerlach**, M. Pinto, N. Kurichiyanil, C. Grau, J. Hérault, M. Hillbrand, P.R. Poulsen, S. Safai, J.M. Schippers, M. Schwarz, C.S. Søndergaard, F. Tommasino, E. Verroi, M. Vidal, I. Yohannes, J. Schreiber und K. Parodi, *Physics in Medicine & Biology* **65** (2020), 245045.
- K. Parodi, W. Assmann, C. Belka, J. Bortfeldt, D.A. Clevert, G. Dedes, R. Kalunga, **S. Kundel**, N. Kurichiyanil, P. Lämmer, J. Lascaud, K. Lauber, G. Lovatti, S. Meyer, M. Nitta, M. Pinto, M.J. Safari, K. Schnürle, J. Schreiber, P.G. Thirolf, H.P. Wieser und M. Würl, *Acta Oncologica* **10** (2019), 1470.

Conference proceedings

- F. Balling, **S. Gerlach**, A.K. Schmidt, V. Bagnoud, J. Hornung, B. Zielbauer, K. Parodi und J. Schreiber: First tests of the I-BEAT detector as primary monitor for target normal sheath accelerated protons. In *Proc. SPIE, Laser Acceleration of Electrons, Protons, and Ions VI*, **11779** (2021), 27.
- J. Hartmann, T. F. Rösch, F. Balling, M. Berndl, L. Flaig, **S. Gerlach**, L. Tischendorf, and J. Schreiber. Commissioning of the laser-driven ion acceleration

beamline at the Centre for Advanced Laser Applications. In *Proc. SPIE, Laser Acceleration of Electrons, Protons, and Ions VI*, **11779** (2021), 44.

Conference contributions

- **Oral:** Particle bunch monitoring at high repetition rates using ionoacoustics. *43rd Workshop on High-Energy-Density Physics with Laser and Ion beams*, Hirschegg (Austria), 2023.
- **Oral:** Laser-Driven Ion Acceleration at the Centre for Advanced Laser Applications. *Conference on High Intensity Laser and Attosecond Science*, Tel Aviv (Israel), 2022.
- **Poster:** Detection of focused laser accelerated particle bunches using acoustic traces: the I-BEAT 3D detector. *9th International Conference on Ultrahigh Intensity Lasers*, Jeju Island (Republic of Korea), 2022.
- **Oral:** Detection of focused laser-accelerated particle bunches using acoustic traces: The I-BEAT 3D detector. *Beamline & Instrumentation for Laser-Driven Particle Acceleration*, Garching (Germany), 2022.
- **Oral:** Detection of Single Monoenergetic Ion Bunches using Ionoacoustics. *Spring meeting of the German Physical Society in Mainz*, virtual, 2022.
- **Oral:** Ionoacoustics for particle beam monitoring: The I-BEAT detector. *42rd Workshop on High-Energy-Density Physics with Laser and Ion beams*, virtual, 2022.
- **Poster:** Particle Dosimetry for Pulsed Ultra High Peak Dose Rates: The I-BEAT Detector. *Flash Radiotherapy And Particle Therapy conference*, virtual, 2021.
- **Poster:** Beam Monitoring for Pulsed Ultra High Dose Rates: The TI-BEAT Detector. *Flash Radiotherapy And Particle Therapy conference*, virtual, 2021.
- **Oral:** Detection of Laser-Accelerated Ions using the Ionoacoustic Approach: the I-BEAT Detector. *Spring meeting of the German Physical Society in Dortmund*, virtual, 2021.
- **Oral:** Three Dimensional Dose Reconstruction for Laser-Accelerated Ions: The I-BEAT Detector. *41rd Workshop on High-Energy-Density Physics with Laser and Ion beams*, virtual, 2021.

- **Invited talk:** I-BEAT: Acoustic Characterization of Laser-accelerated Ions for a User Beamline. *ELIMAIA Beamline User Workshop*, virtual, 2020.

Supervised theses

- **Master's thesis** *Ina Hofrichter* Investigation of the Axial I-BEAT Signal: The Entrance Window as an Acoustic Etalon (2023).
- **Bachelor's thesis** *Oleksii Fedorenko* Automated Field Measurements of Permanent Magnet Quadrupoles with Lengths of 20, 40 and 80 mm (2022).
- **Master's thesis** *Anna-Katharina Schmidt* Characterization of a Plasma-Acoustic Source for the Calibration of Ultrasonic Transducers (2021).
- **Bachelor's thesis** *David Jonathan Walcher* Absolute Calibration of Radiochromic Films (2021).

Third party funding & awards

- BMBF project (01IS17048, 100k€) Data-based optimization of a laser-ion source (2022-2023).
- Prize for the best poster at the 9^{th} International Conference on Ultrahigh Intensity Lasers (2022).

Bibliography

[1] Robinson, M. *Symmetry and the Standard Model: Mathematics and Particle Physics*. SpringerLink : Bücher (Springer New York, 2011).

[2] Lechner, A. Particle interactions with matter. *CERN Yellow Reports: School Proceedings* **Vol 5**, 47 Pages (2018). Artwork Size: 47 Pages Publisher: CERN.

[3] Wang, L. V. & Yao, J. A practical guide to photoacoustic tomography in the life sciences. *Nature Methods* **13**, 627–638 (2016).

[4] Askaryan, G. A. Hydrodynamic radiation from the tracks of ionizing particles in stable liquids. *The Soviet Journal of Atomic Energy* **3**, 921–923 (1957).

[5] Sulak, L. *et al.* Experimental studies of the acoustic signature of proton beams traversing fluid media. *Nuclear Instruments and Methods* **161**, 203–217 (1979).

[6] Askariyan, G., Dolgoshein, B., Kalinovsky, A. & Mokhov, N. Acoustic detection of high energy particle showers in water. *Nuclear Instruments and Methods* **164**, 267–278 (1979).

[7] Takata, T. *et al.* Reprint of Localized dose delivering by ion beam irradiation for experimental trial of establishing brain necrosis model. *Applied Radiation and Isotopes* **106**, 104–106 (2015).

[8] Linz, U. (ed.) *Ion Beam Therapy: Fundamentals, Technology, Clinical Applications*, vol. 320 of *Biological and Medical Physics, Biomedical Engineering* (Springer Berlin Heidelberg, Berlin, Heidelberg, 2012).

[9] Parodi, K. & Polf, J. C. *In vivo* range verification in particle therapy. *Medical Physics* **45** (2018).

[10] Paganetti, H. Range uncertainties in proton therapy and the role of Monte Carlo simulations. *Physics in Medicine and Biology* **57**, R99–R117 (2012).

[11] Knopf, A.-C. & Lomax, A. *In vivo* proton range verification: a review. *Physics in Medicine and Biology* **58**, R131–R160 (2013).

[12] Parodi, K. Vision 20/20: Positron emission tomography in radiation therapy planning, delivery, and monitoring: PET in RT planning, delivery, and monitoring. *Medical Physics* **42**, 7153–7168 (2015).

[13] Parodi, K. PET monitoring of hadrontherapy. *Nuclear Medicine Review* **15**, 37–42 (2012).

[14] Zhu, X. & Fakhri, G. E. Proton Therapy Verification with PET Imaging. *Theranostics* **3**, 731–740 (2013).

[15] Nishio, T. *et al.* The Development and Clinical Use of a Beam ON-LINE PET System Mounted on a Rotating Gantry Port in Proton Therapy. *International Journal of Radiation Oncology*Biology*Physics* **76**, 277–286 (2010).

[16] Richter, C. *et al.* First clinical application of a prompt gamma based in vivo proton range verification system. *Radiotherapy and Oncology* **118**, 232–237 (2016).

[17] Tada, J., Hayakawa, Y., Hosono, K. & Inada, T. Time resolved properties of acoustic pulses generated in water and in soft tissue by pulsed proton beam irradiation-A possibility of doses distribution monitoring in proton radiation therapy: Time resolved properties of acoustic pulses. *Medical Physics* **18**, 1100–1104 (1991).

[18] Hayakawa, Y. *et al.* Acoustic pulse generated in a patient during treatment by pulsed proton radiation beam. *Radiation Oncology Investigations* **3**, 42–45 (1995).

[19] Assmann, W. *et al.* Ionoacoustic characterization of the proton Bragg peak with submillimeter accuracy: Ionoacoustic Characterization of the proton Bragg peak. *Medical Physics* **42**, 567–574 (2015).

[20] Lehrack, S. *et al.* Submillimeter ionoacoustic range determination for protons in water at a clinical synchrocyclotron. *Physics in Medicine & Biology* **62**, L20 (2017).

[21] Patch, S. K. *et al.* Thermoacoustic range verification during pencil beam delivery of a clinical plan to an abdominal imaging phantom. *Radiotherapy and Oncology* **159**, 224–230 (2021).

[22] Jones, K. C. *et al.* Experimental observation of acoustic emissions generated by a pulsed proton beam from a hospital-based clinical cyclotron: Measurement of acoustic emissions by clinical proton beam. *Medical Physics* **42**, 7090–7097 (2015).

[23] van Dongen, K. W. A., de Blécourt, A. J., Lens, E., Schaart, D. R. & Vos, F. M. Reconstructing 3D proton dose distribution using ionoacoustics. *Physics in Medicine & Biology* **64**, 225005 (2019).

[24] Yu, Y., Li, Z., Zhang, D., Xing, L. & Peng, H. Simulation studies of time reversal-based protoacoustic reconstruction for range and dose verification in proton therapy. *Medical Physics* **46**, 3649–3662 (2019).

[25] Yao, S., Hu, Z., Xie, Q., Yang, Y. & Peng, H. Further investigation of 3D dose verification in proton therapy utilizing acoustic signal, wavelet decomposition and machine learning. *Biomedical Physics & Engineering Express* **8**, 015008 (2022).

[26] Wieser, H. P. *et al.* Experimental demonstration of accurate Bragg peak localization with ionoacoustic tandem phase detection (iTPD). *Physics in Medicine & Biology* **66**, 245020 (2021).

[27] Lascaud, J. *et al.* Investigating the accuracy of co-registered ionoacoustic and ultrasound images in pulsed proton beams. *Physics in Medicine & Biology* **66**, 185007 (2021).

[28] Lehrack, S. *et al.* Ionoacoustic detection of swift heavy ions. *Nuclear Instruments and Methods in Physics Research Section A: Accelerators, Spectrometers, Detectors and Associated Equipment* **950**, 162935 (2020).

[29] Lascaud, J. *et al.* Applicability of Capacitive Micromachined Ultrasonic Transducers for the detection of proton-induced thermoacoustic waves. In *2019 IEEE International Ultrasonics Symposium (IUS)*, 143–146 (IEEE, Glasgow, United Kingdom, 2019).

[30] Takayanagi, T. *et al.* On-line range verification for proton beam therapy using spherical ionoacoustic waves with resonant frequency. *Scientific Reports* **10**, 20385 (2020).

[31] Lascaud, J. *et al.* Enhancement of the ionoacoustic effect through ultrasound and photoacoustic contrast agents. *Scientific Reports* **11**, 2725 (2021).

[32] Macchi, A., Borghesi, M. & Passoni, M. Ion acceleration by superintense laser-plasma interaction. *Reviews of Modern Physics* **85**, 751–793 (2013).

[33] Daido, H., Nishiuchi, M. & Pirozhkov, A. S. Review of laser-driven ion sources and their applications. *Reports on Progress in Physics* **75**, 056401 (2012).

[34] Yoon, J. W. *et al.* Realization of laser intensity over 10^{23} W/cm ^{2}. *Optica* **8**, 630 (2021).

[35] Higginson, A. *et al.* Near-100 MeV protons via a laser-driven transparency-enhanced hybrid acceleration scheme. *Nature Communications* **9**, 724 (2018).

[36] Jahn, D. *et al.* Focusing of multi-MeV, subnanosecond proton bunches from a laser-driven source. *Physical Review Accelerators and Beams* **22**, 011301 (2019).

[37] Cowan, T. E. *et al.* Ultralow Emittance, Multi-MeV Proton Beams from a Laser Virtual-Cathode Plasma Accelerator. *Physical Review Letters* **92**, 204801 (2004).

[38] Busold, S. *et al.* Focusing and transport of high-intensity multi-MeV proton bunches from a compact laser-driven source. *Physical Review Special Topics - Accelerators and Beams* **16**, 101302 (2013).

[39] Brack, F.-E. *et al.* Spectral and spatial shaping of laser-driven proton beams using a pulsed high-field magnet beamline. *Scientific Reports* **10**, 9118 (2020).

[40] Rösch, T. F. *et al.* A feasibility study of zebrafish embryo irradiation with laser-accelerated protons. *Review of Scientific Instruments* **91**, 063303 (2020).

[41] Kroll, F. *et al.* Tumour irradiation in mice with a laser-accelerated proton beam. *Nature Physics* **18**, 316–322 (2022).

[42] Ostermayr, T. M. *et al.* Laser-driven x-ray and proton micro-source and application to simultaneous single-shot bi-modal radiographic imaging. *Nature Communications* **11**, 6174 (2020).

[43] Prasselsperger, A. *et al.* Real-Time Electron Solvation Induced by Bursts of Laser-Accelerated Protons in Liquid Water. *Physical Review Letters* **127**, 186001 (2021).

[44] Habs, D. *et al.* Introducing the fission–fusion reaction process: using a laser-accelerated Th beam to produce neutron-rich nuclei towards the N=126 waiting point of the r-process. *Applied Physics B* **103**, 471–484 (2011).

[45] Romano, F. *et al.* Challenges in dosimetry of particle beams with ultra-high pulse dose rates. *Journal of Physics: Conference Series* **1662**, 012028 (2020).

[46] Hornung, J. *et al.* Enhancement of the laser-driven proton source at PHELIX. *High Power Laser Science and Engineering* **8**, e24 (2020).

[47] Lindner, F. H. *et al.* Charge-state resolved laser acceleration of gold ions to beyond 7 MeV/u. *Scientific Reports* **12**, 4784 (2022).

[48] Doria, D. *et al.* Calibration of BAS-TR image plate response to GeV gold ions. *Review of Scientific Instruments* **93**, 033304 (2022).

[49] Lindner, F. H. *et al.* A novel approach to electron data background treatment in an online wide-angle spectrometer for laser-accelerated ion and electron bunches. *Review of Scientific Instruments* **89**, 013301 (2018).

[50] Harres, K. *et al.* Development and calibration of a Thomson parabola with microchannel plate for the detection of laser-accelerated MeV ions. *Review of Scientific Instruments* **79**, 093306 (2008).

[51] Ter-Avetisyan, S. *et al.* Ion acceleration with few-cycle relativistic laser pulses from foil targets. *Plasma Physics and Controlled Fusion* **65**, 085012 (2023).

[52] Hartmann, J. *et al.* Commissioning of the laser-driven ion acceleration beamline at the Centre for Advanced Laser Applications. In Bulanov, S. S., Schroeder, C. B. & Schreiber, J. (eds.) *Laser Acceleration of Electrons, Protons, and Ions VI*, 21 (SPIE, Online Only, Czech Republic, 2021).

[53] Scuderi, V. *et al.* TOF diagnosis of laser accelerated, high-energy protons. *Nuclear Instruments and Methods in Physics Research Section A: Accelerators, Spectrometers, Detectors and Associated Equipment* **978**, 164364 (2020).

[54] Reimold, M. *et al.* Time-of-flight spectroscopy for laser-driven proton beam monitoring. *Scientific Reports* **12**, 21488 (2022).

[55] Green, J. S. *et al.* Scintillator-based ion beam profiler for diagnosing laser-accelerated ion beams. In Ledingham, K. W. D. *et al.* (eds.) *SPIE Optics + Optoelectronics*, 807919 (SPIE, Prague, Czech Republic, 2011).

[56] Dover, N. P. *et al.* Scintillator-based transverse proton beam profiler for laser-plasma ion sources. *Review of Scientific Instruments* **88**, 073304 (2017).

[57] Huault, M. *et al.* A 2D scintillator-based proton detector for high repetition rate experiments. *High Power Laser Science and Engineering* **7**, e60 (2019).

[58] Geulig, L. D. *et al.* Online charge measurement for petawatt laser-driven ion acceleration. *Review of Scientific Instruments* **93**, 103301 (2022).

[59] Haffa, D. *et al.* I-BEAT: Ultrasonic method for online measurement of the energy distribution of a single ion bunch - Supplementary material. *Scientific Reports* **9**, 6714 (2019).

[60] Gerlach, S. *et al.* Three-Dimensional Acoustic Monitoring of Laser-Accelerated Protons in the Focus of a Pulsed-Power Solenoid Lens. *High Power Laser Science and Engineering* **11**, e38 (2023).

[61] Schreiber, J., Bolton, P. R. & Parodi, K. Invited Review Article: "Hands-on" laser-driven ion acceleration: A primer for laser-driven source development and potential applications. *Review of Scientific Instruments* **87**, 071101 (2016).

[62] Esirkepov, T., Borghesi, M., Bulanov, S. V., Mourou, G. & Tajima, T. Highly Efficient Relativistic-Ion Generation in the Laser-Piston Regime. *Physical Review Letters* **92**, 175003 (2004).

[63] Silva, L. O. *et al.* Proton Shock Acceleration in Laser-Plasma Interactions. *Physical Review Letters* **92**, 015002 (2004).

[64] Mainfray, G. & Manus, G. Multiphoton ionization of atoms. *Reports on Progress in Physics* **54**, 1333–1372 (1991).

[65] Gibbon, P. *Short Pulse Laser Interactions with Matter: An Introduction* (PUBLISHED BY IMPERIAL COLLEGE PRESS AND DISTRIBUTED BY WORLD SCIENTIFIC PUBLISHING CO., 2005).

[66] Schreiber, J., Bell, F. & Najmudin, Z. Optimization of relativistic laser–ion acceleration. *High Power Laser Science and Engineering* **2**, e41 (2014).

[67] Schreiber, J. *et al.* Analytical Model for Ion Acceleration by High-Intensity Laser Pulses. *Physical Review Letters* **97** (2006).

[68] Roth, M. & Schollmeier, M. Ion Acceleration—Target Normal Sheath Acceleration. *CERN Yellow Reports* 231 Pages (2016). Artwork Size: 231 Pages Publisher: CERN, Geneva.

[69] Schreiber, J. ALPA Homepage (2023). URL `https://www.alpa.physik.uni-muenchen.de/protons.html`.

[70] Wagner, F. *et al.* Maximum Proton Energy above 85 MeV from the Relativistic Interaction of Laser Pulses with Micrometer Thick CH 2 Targets. *Physical Review Letters* **116**, 205002 (2016).

[71] Ziegler, T. *et al.* Proton beam quality enhancement by spectral phase control of a PW-class laser system. *Scientific Reports* **11**, 7338 (2021).

[72] Hartmann, J. *Quantitative Ion Spectrometry and first laser-ion acceleration results at the Centre for Advanced Laser Applications.* Ph.D. thesis, Ludwig–Maximilians–Universität München (2022).

[73] Rösch, T. *Characterization of a Permanent Magnet Quadrupoles Focus of Laser-accelerated Protons.* Ph.D. thesis, Ludwig–Maximilians–Universität München (2022).

[74] Fuchs, J. *et al.* Comparative spectra and efficiencies of ions laser-accelerated forward from the front and rear surfaces of thin solid foils. *Physics of Plasmas* **14**, 053105 (2007).

[75] Lindstrøm, C. *et al.* Emittance Preservation in an Aberration-Free Active Plasma Lens. *Physical Review Letters* **121**, 194801 (2018).

[76] Hinterberger, F. *Physik der Teilchenbeschleuniger und Ionenoptik* (Springer Berlin Heidelberg, 2008), 2 edn.

[77] Wiedemann, H. *Particle Accelerator Physics* (Springer Berlin Heidelberg, 1993).

[78] Kumar, V. Understanding the focusing of charged particle beams in a solenoid magnetic field. *American Journal of Physics* **77**, 737–741 (2009).

[79] Reiser, M. *Theory and Design of Charged Particle Beams* (Wiley, 2008), 1 edn.

[80] Hofmann, I. Performance of solenoids versus quadrupoles in focusing and energy selection of laser accelerated protons. *Physical Review Special Topics - Accelerators and Beams* **16**, 041302 (2013).

[81] Bortfeld, T. An analytical approximation of the Bragg curve for therapeutic proton beams. *Medical Physics* **24**, 2024–2033 (1997).

[82] Wang, L. V. & Wu, H.-I. *Biomedical Optics: Principles and Imaging* (John Wiley & Sons, Inc., Hoboken, NJ, USA, 2009).

[83] Xu, M. & Wang, L. V. Photoacoustic imaging in biomedicine. *Review of Scientific Instruments* **77**, 041101 (2006).

[84] National Institute of Standards and Technology (NIST): PSTAR (2023). URL `https://physics.nist.gov/PhysRefData/Star/Text/PSTAR.html`.

[85] Abramowitz, M. *Handbook of Mathematical Functions, With Formulas, Graphs, and Mathematical Tables* (Dover Publications, Inc., USA, 1974).

[86] Zwillinger, D. & Moll, V. *Table of Integrals, Series, and Products* (Elsevier, 2015).

[87] Jackson, J. D. Electrodynamics, Classical. In Wiley-VCH Verlag GmbH & Co. KGaA (ed.) *digital Encyclopedia of Applied Physics*, eap109 (Wiley-VCH Verlag GmbH & Co. KGaA, Weinheim, Germany, 2003).

[88] James, D. W. The thermal diffusivity of ice and water between -40 and + 60 C. *Journal of Materials Science* **3**, 540–543 (1968).

[89] Yang, R. Development of an Energy Spectrometer based on Thermoacoustics for Laser Accelerated Ions. Tech. Rep., Ludwig–Maximilians–Universität München, München (2017).

[90] Williams, T. L. *The Optical Transfer Function of Imaging Systems* (Routledge, 2018), 1 edn.

[91] Wieser, H.-P. Accurate Simulation and Validation of the Detector Response for improved Bragg Peak Localization via Ionoacoustics. *Medical Physics* **47**, 2579–2674 (2020).

[92] Ahmad, M., Xiang, L., Yousefi, S. & Xing, L. Theoretical detection threshold of the proton-acoustic range verification technique: Proton-acoustic detection threshold. *Medical Physics* **42**, 5735–5744 (2015).

[93] Schmidt, A.-K. Characterization of a Plasma-Acoustic Source for the Calibration of Ultrasonic Transducers. Master's Thesis, Ludwig–Maximilians–Universität München (2021).

[94] Grassberger, C., Lomax, A. & Paganetti, H. Characterizing a proton beam scanning system for Monte Carlo dose calculation in patients. *Physics in Medicine and Biology* **60**, 633–645 (2015).

[95] FEMTO Messtechnik GmbH (2023). URL `www.femto.de`.

[96] Instruments, T. Application Report SLOA033A: Signal Conditioning Piezoelectric Sensors (2000).

[97] Reeg, H. & Schneider, N. Current transformers for GSI's keV/u to GeV/u ion beams-an overview. *Proceedings of DIPAC 2001* 120–122 (2001).

[98] GSI Helmholtzzentrum für Schwerionenforschung. SEETRAM (2022). URL `https://www-windows.gsi.de/Charms/seetraminfo/seetram2.htm`.

[99] Junghans, A. *et al.* A self-calibrating ionisation chamber for the precise intensity calibration of high-energy heavy-ion beam monitors. *Nuclear Instruments and Methods in Physics Research Section A: Accelerators, Spectrometers, Detectors and Associated Equipment* **370**, 312–314 (1996).

[100] Ashland Inc. (2023). URL `http://www.gafchromic.com/gafchromic-film/radiotherapy-films/EBT/index.asp`.

[101] Walcher, D. Absolute Calibration of Radiochromic Films. Bachelor's Thesis, Ludwig–Maximilians–Universität München (2021).

[102] Hofrichter, I. Investigation of the axial I-BEAT signal - The entrance window as an acoustic etalon. Master's Thesis, Ludwig–Maximilians–Universität München (2023).

[103] Reinhardt, S. *Detection of laser-accelerated protons.* Ph.D. thesis, Ludwig–Maximilians–Universität München (2012).

[104] Brown, T. A. D. *et al.* Dose-response curve of EBT, EBT2, and EBT3 radiochromic films to synchrotron-produced monochromatic x-ray beams: EBT, EBT2, and EBT3 response to monochromatic x-rays. *Medical Physics* **39**, 7412–7417 (2012).

[105] Zhang, R., Taddei, P. J., Fitzek, M. M. & Newhauser, W. D. Water equivalent thickness values of materials used in beams of protons, helium, carbon and iron ions. *Physics in Medicine and Biology* **55**, 2481–2493 (2010).

[106] Esplen, N., Mendonca, M. S. & Bazalova-Carter, M. Physics and biology of ultrahigh dose-rate (FLASH) radiotherapy: a topical review. *Physics in Medicine & Biology* **65**, 23TR03 (2020).

[107] Luijk, P. v., Veld, A. A. v. t., Zelle, H. D. & Schippers, J. M. Collimator scatter and 2D dosimetry in small proton beams. *Physics in Medicine and Biology* **46**, 653–670 (2001).

[108] Kellnberger, S. *et al.* Ionoacoustic tomography of the proton Bragg peak in combination with ultrasound and optoacoustic imaging. *Scientific Reports* **6**, 29305 (2016).

[109] Donadio, E. Studies and simulation of a transmissive ionoacoustic detector for conventional and laser-accelerated protons. Internship report, Ludwig–Maximilians–Universität München (2022).

[110] Maier, A. R. *et al.* Decoding Sources of Energy Variability in a Laser-Plasma Accelerator. *Physical Review X* **10**, 031039 (2020).

[111] Jalas, S. *et al.* Bayesian Optimization of a Laser-Plasma Accelerator. *Physical Review Letters* **126**, 104801 (2021).

[112] Loughran, B. *et al.* Automated control and optimization of laser-driven ion acceleration. *High Power Laser Science and Engineering* **11**, e35 (2023).

[113] Hedderich, J. & Sachs, L. *Angewandte Statistik* (Springer Berlin Heidelberg, Berlin, Heidelberg, 2016).

[114] Lascaud, J. *et al.* Optimization of the backing material of a low frequency PVDF detector for ion beam monitoring during small animal proton irradiation. In *2021 IEEE International Ultrasonics Symposium (IUS)*, 1–4 (IEEE, Xi'an, China, 2021).

Danksagung

Mit großer Dankbarkeit blicke ich auf die Zeit während der Doktorarbeit zurück und möchte mich bei all denjenigen bedanken, die mich auf diesem Weg begleitet und unterstützt haben. Mein erster Dank gebührt Prof. Jörg Schreiber für seine inspirierende Anleitung, fachliche Unterstützung und wertvollen Ratschläge. Seine Begeisterung für das Fachgebiet und sein Vertrauen in junge & wilde Studierende haben maßgeblich dazu beigetragen, dass diese Dissertation gelingen konnte. Es gab kaum ein Meeting, aus dem ich nicht hochmotiviert wieder an die Arbeit gegangen bin. Ebenso möchte ich Prof. Katia Parodi herzlich für ihre langjährige Begleitung und die vielfältigen Möglichkeiten, die sie mir eröffnet hat, danken. Ganz besonders ist hierbei das Graduiertenkolleg 2274 zu nennen. Durch das Graduiertenkolleg habe ich Einblicke in Themenbereiche gewinnen konnte, die über mein Hauptforschungsgebiet hinausgehen, wie etwa klinische Fragestellungen. Die Diskussionen und Erkenntnisse aus den vielen Seminaren haben meinen Horizont erweitert und meinen wissenschaftlichen Werdegang nachhaltig beeinflusst. Als Zweitgutachterin hat Prof. Parodi diese Forschungsarbeit erst möglich gemacht und wertvolle Anregungen eingebracht.
Ein großer Dank geht an meine Kolleginnen und Kollegen, die mit mir gemeinsam in LION gearbeitet haben. Zuallererst Jens Hartmann und Thomas Rösch, die von Anfang an an meiner Seite standen und von denen ich das lernen durfte, was das wichtigste für diese Arbeit war: Wie man Protonen mit einem Laser beschleunigt und fokusiert. Danke für eure Geduld und euer Wissen, und am allermeisten für euren Humor! Mein Studienpartner war in dieser intensiven Anfangszeit Felix Balling, der mit mir versucht hat die dunkle Magie der Ionenbeschleunigung zu lernen. Vielen Dank für die vielen sehr kompetenten Ratschläge sowohl was Laser, Protonen oder Ionoacoustic angeht, die geteilte Freude wenn ich ein Problem gelöst habe, und natürlich die gemeinsamen Kaffepausen! Ein herzliches Dankeschön gilt auch den noch jüngeren und wilderen Alex, Julia, Anna und Michi, die mit der Zeit hinzukamen und die Gruppe bereichert haben. Danke für euer Engagement! An dieser Stelle möchte ich mich auch bei der gesamten AG-Schreiber incl. ihrer Ehemaligen (besonders zu nennen sind hier Martin & Jo) bedanken. Die Stimmung in dieser Gruppe ist etwas ganz besonderes und ich bin sehr froh, Teil davon zu sein!

Ein ganz besonderer Dank geht an meine treue Coffeecrew Laura und Lenny. Laura ist die beste Bürokollegin, die man sich vorstellen kann. Ihre ermutigenden Worte und ihr unerschütterlicher Glaube an mich waren eine ständige Kraftquelle. Sie stand privat wie beruflich stehts hinter mir und ich bin sehr dankbar für ihre kompetenten Ratschläge, ihre bedingungslose Unterstützung und für die vielen inspirierenden Gespräche! Lenny ist mein herausragender Sparringspartner im DAQ Projekt. Ohne Lenny ist bekannterweise LION und CALA schwer denkbar, absolut unmöglich wäre auf jeden Fall das DAQ Projekt gewesen. Ich bin sehr dankbar für Lenny's technisches Wissen was Tango, Stages und eigentlich auch alles andere angeht, und für die Bereitschaft dieses Wissen wenn nötig auch bei nächtlichen Notfallanrufen mit uns zu teilen! Auch menschlich konnte ich mich immer auf Lenny verlassen, und seine ruhige und besonnene Art hat mir oft Kraft und Mut gegeben.
Vielen Dank auch an alle DAQs, zu den bereits genannten Lenny und Michi kommen noch Flo & Vignesh dazu, die auch dieses mysteriöse technische Verständnis haben, was mir fehlt. Ich bin sehr dankbar, für das von euch allen entgegengebrachte Vertrauen! Insgesamt ist das DAQ Projekt fachlich sicher nicht das leichteste erste Forschungsprojekt was man sich hätte suchen können, aber das hervorragende Team lässt es möglich erscheinen.
Ganz herzlich möchte ich mich auch bei den vielen wunderbaren Studentinnen und Studenten bedanken, die ich über die Zeit begleiten durfte. Neben den bereits genannten Anna & Flo meint dies auch David, Vroni, Ina, Elie & Oleksii. Ihr seid alle ausnahmlos sehr talentiert und habt es mir sehr leicht gemacht, euch zu betreuen. Es war mir eine große Freude, euch einen kleinen Teil eurer Ausbildung begleiten zu dürfen!
Vielen Dank auch an den ganzen LS Parodi, der mich nun schon eine Zeit lang begleitet. Ein besonderer Dank gilt dabei dem außerordentlich kompetenten Ionoakustik-Team des Lehrstuhls mit Julie Lascaud und Pratik Dash, und ich möchte auch die ehemalige Walter Assmann und Hans-Peter Wieser nennen. Namentlich möchte ich außerdem Franz Englbrecht danken, der oft eine ganz besondere Hilfe für mich war! Ein herzliches Dankeschön geht auch an die anderen Arbeitsgruppen in CALA, AG Karsch, AG Thirolf und AG Döpp. Stefan Karsch gebührt mein aufrichtiger Dank für seine mutige Entscheidung, den Laser gemeinsam mit Studentinnen und Studenten zu betreiben. Seine Unterstützung und sein Vertrauen in mich waren eine große Stütze und haben mir viel Selbstvertrauen gegeben. Ebenso möchte ich Peter Thirolf von Herzen danken. Peter ist nicht nur ein äußerst kompetenter Wissenschaftler, sondern auch ein außergewöhnlich freundlicher Mensch. Seine Offenheit und Bereitschaft, bei Fragen und Herausforderungen

zur Seite zu stehen, haben meinen Forschungsweg ungemein bereichert. Es war stets eine Freude, auf dich zählen zu können! Danke auch an Andreas Döpp, der sich mit seinem Engagement in CALA einbringt und so eine ganz neue Gruppe entstehen konnte. Ein großes Dank geht auch an das ganze CALA Team: Nik & Oli, Andi Bär, Florian Saran, Hans-Peter Wirth, Katharina Adler und Martin Groß. Ihr macht CALA zu dem was es ist, und es ist einfach schön mit euch im selben Haus zu arbeiten!
Ein großes Dankeschön geht an meine wunderbaren Freunde, die mich immer ermutigt haben und immer hinter mir standen. Ganz zum Schluss möchte ich meiner Familie von ganzem Herzen danken, auf die ich mich immer verlassen kann.